Beam model of Doppler backscattering

Valerian H Hall-Chen[1,2], Felix I Parra[1], and Jon C Hillesheim[2]

[1] Rudolf Peierls Centre for Theoretical Physics, University of Oxford, Oxford OX1 3PU, UK

[2] UKAEA/CCFE, Culham Science Centre, Abingdon, Oxon, OX14 3DB, UK

E-mail: `valerian.chen@physics.ox.ac.uk`

January 2022

Abstract. We use beam tracing — implemented with a newly-written code, Scotty — and the reciprocity theorem to derive a model for the linear backscattered power of the Doppler Backscattering (DBS) diagnostic. Our model works for both the O-mode and X-mode in tokamak geometry (and certain regimes of stellarators). We present the analytical derivation of our model and its implications on the DBS signal localisation and the wavenumber resolution. To determine these two quantities, we find that it is the curvature of the field lines and the magnetic shear that are important, rather than the curvature of the cut-off surface. We also provide an explicit formula for the hitherto poorly-understood quantitative effect of the mismatch angle. Consequently, one can use this model to correct for the attenuation due to mismatch, avoiding the need for empirical optimisation. This is especially important in spherical tokamaks, since the magnetic pitch angle is large and varies both spatially and temporally.

1. Introduction

Turbulent fluctuations in tokamaks are responsible for cross-field transport. The Doppler Backscattering (DBS) microwave diagnostic enables the non-perturbative characterisation of turbulent density fluctuations ($1 \lesssim k_\perp \rho_i \lesssim 10$) [1, 2] and flows [3, 4, 5, 6, 7] with high spatial and temporal resolution, both at the edge and the core of the plasma. Here, $k_\perp$ is the wavenumber of turbulent fluctuations perpendicular to the magnetic field and ρ_i is the ion gyroradius. Consequently, it is a widely used diagnostic for both tokamaks and stellarators [8, 9, 10, 11, 12, 13, 14, 15, 16, 17, 18, 19, 20]. Moreover, since DBS is a microwave diagnostic, it is one of the few diagnostics able to survive the neutron fluxes generated by burning plasmas of future fusion reactors [21, 22].

There is a series of problems we seek to address: mismatch attenuation, wavenumber resolution, and localisation of the signal. We build a model that can account for all of them in realistic geometries and for realistic turbulence spectra. The model that we develop is an extension of previous work on reciprocity by Gusakov and collaborators [23, 24, 25, 26, 27]. We introduce more geometry, do not assume a particular turbulence
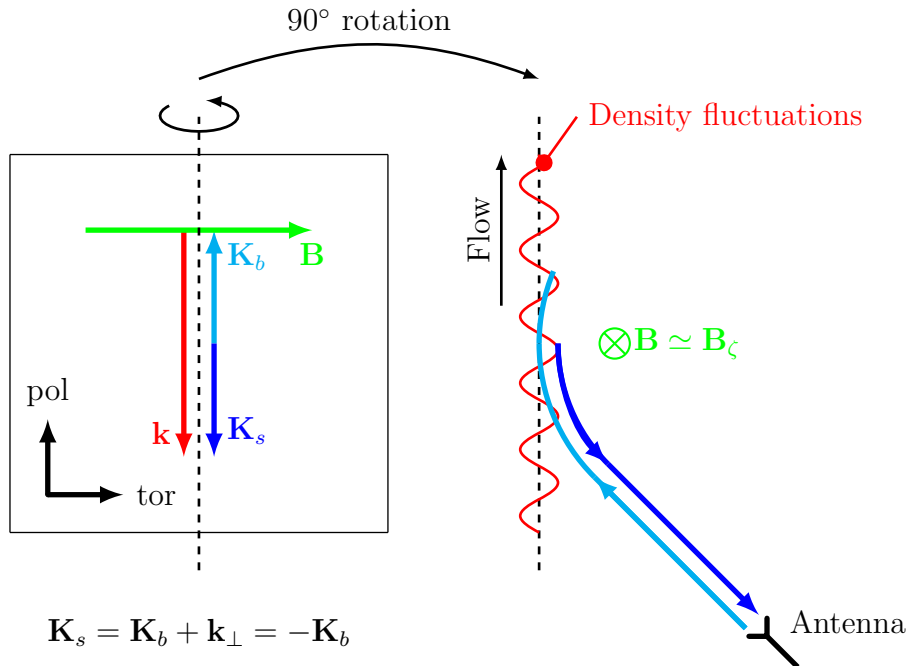
Figure 1: A microwave probe beam is launched into the plasma. The emitting antenna also acts as the receiver, hence only the backscattered signal is measured. The Bragg condition determines how the wavevectors of the turbulence $\mathbf{k}$ (red), the probe beam $\mathbf{K}_b$ (light blue), and the scattered beam $\mathbf{K}_s$ (dark blue) must relate to one another for backscattering to occur. The right side of the figure represents a poloidal cut. The left side of the figure is in the plane perpendicular to the page, through the dotted line on the right side; that is, in both cases, the poloidal direction is pointing up, but on the left, the toroidal direction is in the plane of the page, while on the right, the toroidal direction is into the page. In conventional tokamaks, the magnetic field is mostly in the toroidal direction. In this figure, we depict the density fluctuations at the cut-off for illustrative purposes only. Our model accounts for backscattering at every point along the ray, and we later show the extent to which different points contribute to the signal.

spectrum, and use beam tracing to make the problem more tractable. Since wavenumber resolution and localisation are already widely studied [2, 24, 25], we present our insight on them later in the paper with only a brief introduction here. The rest of this section will focus on the mismatch attenuation.

In order for detectable backscattering to occur, the wavevector of the turbulent fluctuations at a particular point has to be twice in magnitude and opposite in direction to the wavevector of the probe beam at that point (Figure 1). This Bragg condition determines the dominant turbulent wavenumber probed by DBS. The extent to which other wavenumbers are also backscattered into the detector is given by the wavenumber resolution, while the contribution of various points along the ray to the backscattered signal is known as the localisation or spatial resolution.

We now introduce mismatch and the associated attenuation of the backscattered
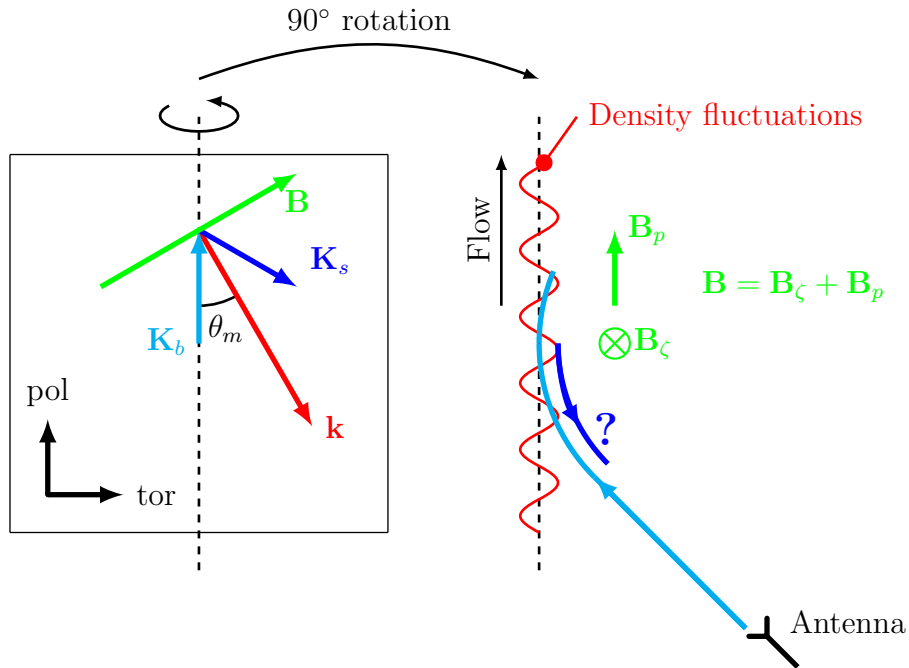
Figure 2: The mismatch angle reduces the backscattered signal. The variables are defined in the caption of Figure 1, except for the poloidal magnetic field $\mathbf{B}_p$, associated with the plasma current and the mismatch angle, which is defined to be $\sin\theta_m = \hat{\mathbf{K}} \cdot \hat{\mathbf{b}}$. Here $\hat{\mathbf{b}}$ and $\hat{\mathbf{K}}$ are the unit vectors of the magnetic field and the probe beam's wavevector respectively. Having a significant poloidal field means that a ray propagating entirely in the poloidal plane can no longer meet the Bragg condition.

signal. The spatial scale of turbulence perpendicular to the field lines is much shorter than the characteristic length parallel to the field lines [28, 29]. Hence, one has to launch the probe beam into the plasma such that the beam reaches the scattering location perpendicular to the magnetic field, allowing the Bragg condition for backscattering to be met. When the poloidal field is much smaller than the toroidal field, as in conventional tokamaks, this is achieved by sending a beam that does not propagate toroidally.

In spherical tokamaks, the magnetic pitch angle is large (up to 35° [30], compared to $\sim 10°$ in conventional tokamaks like JET [31] and KSTAR [32]) and it varies both spatially and temporally. Consequently, the DBS probe beam and the magnetic field are not normal to each other in general. This misalignment decreases the backscattered signal, making interpretation of the signal complicated (Figure 2): a decrease in the signal's magnitude could be due to a decrease in the fluctuations or an increase in the mismatch angle, defined to be $\sin\theta_m = \hat{\mathbf{K}} \cdot \hat{\mathbf{b}}$. Here $\hat{\mathbf{b}}$ and $\hat{\mathbf{K}}$ are the unit vectors along the external magnetic field $\mathbf{B}$ and the probe beam's wavevector $\mathbf{K}$, respectively.

The misalignment can be empirically optimised with 2D beam steering [30, 33]. However, such empirical optimisation is ungainly and expensive, requiring several repeated shots for every measurement. Consequently, a quantitative understanding of the effect of the mismatch angle on the DBS signal would make practical the

characterisation of spherical-tokamak plasmas with DBS.

We seek to develop a quantitative understanding of what affects the backscattered signal and how. We write the electric field due to the microwaves as $\mathbf{E}\mathrm{e}^{-\mathrm{i}\Omega t}$, where Ω is the angular frequency of the microwave beam. Hence, the electric field of the probe beam (which is launched into the plasma) and the scattered microwaves satisfy

$$\frac{c^2}{\Omega^2}\nabla \times (\nabla \times \mathbf{E}) = \boldsymbol{\epsilon} \cdot \mathbf{E}. \tag{1}$$

Here we have already divided away the factor of $\mathrm{e}^{-\mathrm{i}\Omega t}$, and $\boldsymbol{\epsilon}$ is the cold plasma dielectric tensor [34], given by

$$\boldsymbol{\epsilon} = \mathbf{1} - \frac{\Omega_{pe}^2}{\Omega^2 - \Omega_{ce}^2}(\mathbf{1} - \hat{\mathbf{b}}\hat{\mathbf{b}}) - \frac{\Omega_{pe}^2}{\Omega^2}\hat{\mathbf{b}}\hat{\mathbf{b}} + \frac{\mathrm{i}\Omega_{pe}^2\Omega_{ce}}{\Omega(\Omega^2 - \Omega_{ce}^2)}(\hat{\mathbf{b}} \times \mathbf{1}), \tag{2}$$

where $\mathbf{1}$ is the 3×3 identity matrix, $\Omega_{pe} = (\Sigma n_e e^2/m_e\epsilon_0)^{1/2}$ is the electron plasma frequency, $\Omega_{ce} = eB/m_e$ is the electron cyclotron frequency, $\Sigma n_e = n_e + \delta n_e$ is the electron density, n_e is the equilibrium electron density, δn_e is the fluctuating electron density, m_e is the electron mass, e is the absolute value of the electron charge, and ϵ_0 is the permitivity of free space. We split the dielectric tensor into equilibrium and turbulent parts, $\boldsymbol{\epsilon} = \boldsymbol{\epsilon}_{eq} + \boldsymbol{\epsilon}_{tb}$. Assuming the fluctuating part of the electron density is much smaller than its equilibrium part $\delta n_e \ll n_e$, we find that

$$\boldsymbol{\epsilon}_{tb} = \frac{\delta n_e}{n_e}(\boldsymbol{\epsilon}_{eq} - \mathbf{1}). \tag{3}$$

The inhomogeneity length associated with the equilibrium part of $\boldsymbol{\epsilon}$ is long, while the turbulence has a much shorter spatial scale. For $\delta n_e/n_e \ll 1$, we can split the electric field into a large component due to the beam and a small additive term due to the scattered microwaves, $\mathbf{E} \simeq \mathbf{E}_b + \mathbf{E}_s$. The equilibrium part of $\boldsymbol{\epsilon}$ is responsible for propagation, refraction, and diffraction of the probe beam,

$$\frac{c^2}{\Omega^2}\nabla \times (\nabla \times \mathbf{E}_b) - \boldsymbol{\epsilon}_{eq} \cdot \mathbf{E}_b = 0. \tag{4}$$

The scattered electric field $\mathbf{E}_s$, which is much smaller than the probe beam electric field $\mathbf{E}_b$, is associated with the fluctuating part of the dielectric constant, which has a much smaller associated spatial scale,

$$\frac{c^2}{\Omega^2}\nabla \times (\nabla \times \mathbf{E}_s) - \boldsymbol{\epsilon}_{eq} \cdot \mathbf{E}_s = \boldsymbol{\epsilon}_{tb} \cdot \mathbf{E}_b. \tag{5}$$

We use beam tracing in Section 2 to determine the electric field $\mathbf{E}_b$ due to the probe beam. We obtain an integral that determines the backscattered signal using the reciprocity theorem in Section 3. The main thrust of this paper is the simplifications that we apply to this integral to obtain a manageable result, as presented in Sections 4–7. With the form of the backscattered power, we proceed to discuss localisation in Section 8, wavenumber resolution in Section 9, and the effect of the mismatch angle in Sections 10 and 11. We finish with a discussion of the model's insights in Section 12.

2. Beam tracing

To determine the electric field of the probe beam, one could perform full-wave simulations [11, 27, 35, 36, 37, 38]. However, this method requires the turbulent dielectric tensor to high resolution, which is precisely what we do not know and are trying to determine. A seemingly more sensible approach, especially considering that there are many ray tracing codes in the fusion community [39, 40, 41, 42], would be to trace a bundle of rays to reconstruct the microwave electric field. However, since DBS depends on physics near the cut-off [2, 24], this method is not suitable as ray tracing breaks down near the cut-off [43].

One way around this problem is to trace only one ray and perform an expansion around that ray. This method, known as beam tracing, corresponds to tracing the path of a Gaussian beam, where this central ray gives the location of the peak of the Gaussian envelope. The theory of evolving Gaussian beams in isotropic inhomogeneous media is well-studied [44, 45, 46]. Beam tracing in anisotropic inhomogeneous media, which is relevant for magnetic confinement fusion, was covered briefly by Peeters [47] and more extensively by Pereverzev [48, 49, 50, 51] and Poli [52, 53]. Beam tracing has also been implemented numerically [54]; it has so far been used to model electron cyclotron resonance heating (ECRH) [42], electron cyclotron current drive (ECCD) [42, 55, 56], lower-hybrid current drive [57], synthetic-aperture microwave imaging (SAMI) [58], and conventional reflectometry [59, 60]. Importantly, it has been shown that the beam tracing method can be applied near the cut-off [61].

The rest of this section is divided into four parts. Section 2.1 lays out the beam-tracing orderings and equations, summarising the results of our beam-tracing derivation in Appendix A. Next, in Section 2.2, we proceed to describe our choice of the beam-tracing dispersion relation and the subtleties involved in doing this correctly (Section 2.2). Thirdly, Section 2.3 describes our new beam-tracing code. Finally, we detail two scenarios that we use to illustrate the findings of this paper in Section 2.4.

2.1. Ordering and equations

In beam tracing, we assume that the length scale associated with the inhomogeneity of the density L is long compared to both the width W and wavelength λ of the beam, and that the wavelength λ is much smaller than the width of the beam W, $\lambda \ll W \ll L$. We choose the specific ordering [48, 49, 50, 51]

$$\frac{W}{L} \sim \frac{\lambda}{W} \ll 1. \tag{6}$$

Ordering the width as an intermediate length scale follows from classical optics by taking the Rayleigh length to be the same order as the inhomogeneity length. We then consider a region of space close to the trajectory of the central ray, $\mathbf{r} = \mathbf{q}(\tau)$, where τ is a parameter that gives the position along the ray. This $\mathbf{q}$ is not to be confused with the safety factor, usually called q in the literature. We will find the equations for $\mathbf{q}(\tau)$ as part of our beam tracing derivation.

To define a convenient coordinate system, we introduce the effective group velocity (this is not the true group velocity since it is a derivative with respect to the parameter τ, not with respect to time)

$$\mathbf{g} = g\hat{\mathbf{g}} = \frac{\mathrm{d}\mathbf{q}}{\mathrm{d}\tau}, \tag{7}$$

where $g = |\mathbf{g}|$ is the magnitude of $\mathbf{g}$, and $\hat{\mathbf{g}}$ its direction. The group velocity $\mathbf{g}$ is parallel to the central ray. We will describe any arbitrary position as being composed of the position along $\mathbf{q}(\tau)$ and across the ray,

$$\mathbf{r} = \mathbf{q}(\tau) + \mathbf{w} = \mathbf{q}(\tau) + w_x\hat{\mathbf{x}}(\tau) + w_y\hat{\mathbf{y}}(\tau). \tag{8}$$

Here $\hat{\mathbf{x}}(\tau)$ and $\hat{\mathbf{y}}(\tau)$ are two mutually perpendicular unit vectors which are also perpendicular to $\mathbf{g}$. In the orthogonal basis $(\hat{\mathbf{x}}, \hat{\mathbf{y}}, \hat{\mathbf{g}})$, the vector $\mathbf{w}$ is given by

$$\mathbf{w} = \begin{pmatrix} w_x \\ w_y \\ 0 \end{pmatrix}. \tag{9}$$

We write the electric field as

$$\mathbf{E}(\mathbf{r}) = \mathbf{A}(\mathbf{r})\exp\left[\mathrm{i}\psi(\mathbf{r})\right]. \tag{10}$$

Using the beam tracing coordinate system, equation (8), we propose the following ansatz for ψ:

$$\psi(\mathbf{r}) = s(\tau) + \mathbf{K}_w(\tau) \cdot \mathbf{w} + \frac{1}{2}\mathbf{w} \cdot \boldsymbol{\Psi}_w(\tau) \cdot \mathbf{w} + \ldots; \tag{11}$$

higher order terms of ψ are not required in our derivation. Here

$$s = \int_0^\tau K_g(\tau')g(\tau')\,\mathrm{d}\tau' \sim \frac{L}{\lambda}, \tag{12}$$

with $K_g(\tau) = \mathbf{K}(\tau) \cdot \hat{\mathbf{g}}(\tau)$ being the projection of the wavevector along the ray, while

$$\mathbf{K}_w \sim \frac{1}{\lambda}, \tag{13}$$

is the projection of the wavevector perpendicular to the ray. Hence, both K_g and $\mathbf{K}_w$ are real. The 2D symmetric matrix $\boldsymbol{\Psi}_w(\tau)$ is complex, and

$$\boldsymbol{\Psi}_w \sim \frac{1}{W^2}. \tag{14}$$

The real part of $\boldsymbol{\Psi}_w$ is responsible for the curvature of the Gaussian beam, while its imaginary part gives the characteristic decay width of the Gaussian envelope. In general, the real and imaginary parts are not simultaneously diagonalisable. The eigenvalues of the real part are

$$[\mathrm{Re}\,(\boldsymbol{\Psi}_w)]_{\alpha\alpha} = \frac{K^3}{K_g^2}\frac{1}{R_{b,\alpha}}, \tag{15}$$

where $R_{b,\alpha}$ are the radii of curvature of the beam front, while the eigenvalues of the imaginary part are

$$[\mathrm{Im}\,(\boldsymbol{\Psi}_w)]_{\alpha\alpha} = \frac{2}{W_\alpha^2}, \tag{16}$$

where W_α are the beam widths. From here on, we use the subscripts $_g$ and $_w$ to indicate projection parallel and perpendicular to the central ray respectively, and we use bold roman and bold italics to denote vectors and matrices respectively. In the basis $(\hat{\mathbf{x}}, \hat{\mathbf{y}}, \hat{\mathbf{g}})$, $\mathbf{K}_w$ and $\boldsymbol{\Psi}_w$ are

$$\mathbf{K}_w = \begin{pmatrix} K_x \\ K_y \\ 0 \end{pmatrix}, \tag{17}$$

and

$$\boldsymbol{\Psi}_w = \begin{pmatrix} \Psi_{xx} & \Psi_{xy} & 0 \\ \Psi_{yx} & \Psi_{yy} & 0 \\ 0 & 0 & 0 \end{pmatrix}, \tag{18}$$

such that $\mathbf{K}_w \cdot \hat{\mathbf{g}} = 0$ and $\boldsymbol{\Psi}_w \cdot \hat{\mathbf{g}} = 0$.

We expand the amplitude $\mathbf{A}$, given in equation (10), in W/L to obtain

$$\mathbf{A} = \mathbf{A}^{(0)}(\tau) + \mathbf{A}^{(1)}(\tau, \mathbf{w}) + \mathbf{A}^{(2)}(\tau, \mathbf{w}) + \dots, \tag{19}$$

where $A^{(n)} \sim (W/L)^n A^{(0)}$. Only the lowest order term $\mathbf{A}^{(0)}$ is used in this work; finding the evolution equations for higher order corrections to the amplitude requires going to next order in the beam tracing derivation, as we show in Appendix A. We split the zeroth order term into a complex amplitude $A^{(0)}$ and a polarisation $\hat{\mathbf{e}}$,

$$\mathbf{A}^{(0)}(\tau) = A^{(0)}(\tau)\,\hat{\mathbf{e}}\left(\mathbf{q}(\tau), K_g(\tau), \mathbf{K}_w(\tau)\right). \tag{20}$$

The polarisation depends on $\mathbf{q}(\tau)$, $K_g(\tau)$, $\mathbf{K}_w(\tau)$, and satisfies

$$\hat{\mathbf{e}} \cdot \hat{\mathbf{e}}^* = 1. \tag{21}$$

We derive (in Appendix A) the equations to determine the functions of τ — $\mathbf{q}$, K_g, $\mathbf{K}_w$, $\boldsymbol{\Psi}_w$, $A^{(0)}$, and $\hat{\mathbf{e}}$. These equations are summarised here. First, we define

$$\boldsymbol{D}(\mathbf{q}, \mathbf{K}) = \frac{c^2}{\Omega^2}\left(\mathbf{K}\mathbf{K} - K^2 \mathbf{1}\right) + \boldsymbol{\epsilon}(\mathbf{q}). \tag{22}$$

Since $\boldsymbol{D}$ is Hermitian, we can find its eigenvalues and eigenvectors,

$$\boldsymbol{D} \cdot \hat{\mathbf{e}} = H\hat{\mathbf{e}}. \tag{23}$$

This equation defines the dispersion relation $H(\mathbf{q}, \mathbf{K})$ corresponding to the polarisation $\hat{\mathbf{e}}(\mathbf{q}, \mathbf{K})$. We want $H = 0$ at all points along the central ray. One way to ensure that is to choose $\mathbf{K}$ such that $H = 0$ at some arbitrary point $\mathbf{q}$ along the central ray. Then, evolve $\mathbf{q}$ and $\mathbf{K} = K_g \hat{\mathbf{g}} + \mathbf{K}_w$ using

$$\frac{\mathrm{d}\mathbf{q}}{\mathrm{d}\tau} = \nabla_K H, \tag{24}$$

and

$$\frac{\mathrm{d}\mathbf{K}}{\mathrm{d}\tau} = -\nabla H, \tag{25}$$

such that $H = 0$ along the rest of the ray. The associated polarisation $\hat{\mathbf{e}}$ is then calculated in post-processing. We do not account for mode conversion in this work. That is, either

the O-mode or X-mode has $H = 0$, and we assume that the dispersion relation of the other mode is always sufficiently different from zero. This assumption has worked well in the cases studied in this paper. However, it is known to fail when the magnetic shear is large, giving rise to mode conversion [62, 63, 64, 65, 66, 67, 68].

For convenience, instead of evolving $\boldsymbol{\Psi}_w$, we evolve the 3D matrix

$$\boldsymbol{\Psi}(\tau) = \nabla\nabla\psi\left(\tau, w_x = 0, w_y = 0\right), \tag{26}$$

from which $\boldsymbol{\Psi}_w$ is subsequently determined. The equation for $\boldsymbol{\Psi}$ is

$$\frac{\mathrm{d}\boldsymbol{\Psi}}{\mathrm{d}\tau} = -\left(\boldsymbol{\Psi}\cdot\nabla_K\nabla_K H\cdot\boldsymbol{\Psi} + \boldsymbol{\Psi}\cdot\nabla_K\nabla H + \nabla\nabla_K H\cdot\boldsymbol{\Psi} + \nabla\nabla H\right). \tag{27}$$

The matrix $\boldsymbol{\Psi}_w$ can be deduced from $\boldsymbol{\Psi}$ by projecting $\boldsymbol{\Psi}$ on the plane perpendicular to $\hat{\mathbf{g}}$.

Finally, we split the amplitude into its modulus and its phase,

$$A^{(0)} = \left|A^{(0)}\right|\exp\left[\mathrm{i}\left(\phi_G + \phi_P\right)\right]. \tag{28}$$

Its modulus is given by

$$\left|A^{(0)}\right| = C\left[\det\left(\mathrm{Im}\left(\boldsymbol{\Psi}_w\right)\right)\right]^{\frac{1}{4}} g^{-\frac{1}{2}}, \tag{29}$$

where C is a constant of integration and $\det\left[\mathrm{Im}\left(\boldsymbol{\Psi}_w\right)\right] = \mathrm{Im}\left(\Psi_{xx}\right)\mathrm{Im}\left(\Psi_{yy}\right) - \left[\mathrm{Im}\left(\Psi_{xy}\right)\right]^2$; its phase is $\phi_G + \phi_P$, which is composed of the Gouy phase ϕ_G, given by

$$\frac{\mathrm{d}\phi_G}{\mathrm{d}\tau} = -\mathrm{Im}(\boldsymbol{\Psi}) : \nabla_K\nabla_K H, \tag{30}$$

and the phase associated with the changing polarisation when propagating through a plasma ϕ_P, given by

$$\frac{\mathrm{d}\phi_P}{\mathrm{d}\tau} = \mathrm{i}\frac{\mathrm{d}\hat{\mathbf{e}}}{\mathrm{d}\tau}\cdot\hat{\mathbf{e}}^* - \frac{1}{2\mathrm{i}}\left(\frac{\partial\hat{\mathbf{e}}^*}{\partial K_\mu}\cdot\boldsymbol{D}\cdot\frac{\partial\hat{\mathbf{e}}}{\partial r_\mu} - \frac{\partial\hat{\mathbf{e}}^*}{\partial r_\mu}\cdot\boldsymbol{D}\cdot\frac{\partial\hat{\mathbf{e}}}{\partial K_\mu}\right). \tag{31}$$

Our derivation in Appendix A, an alternative approach to Pereverzev's original work [48, 49, 50, 51], shows that the beam tracing equations for $\mathbf{q}$, K_g, $\mathbf{K}_w$, $\boldsymbol{\Psi}_w$, $A^{(0)}$, and $\hat{\mathbf{e}}$ are the result of forcing equation (10) to be a solution of equation (4), keeping terms up to and including $(W/L)^2$.

Given the properties of the launch beam at the antenna, we can then calculate how it evolves as it propagates into the plasma. This initial condition for a beam launched perpendicular to the surface of the antenna is

$$\mathbf{E}_{ant} = A_{ant}\hat{\mathbf{e}}_{ant}\exp\left(\frac{\mathrm{i}}{2}\mathbf{w}\cdot\boldsymbol{\Psi}_{w,ant}\cdot\mathbf{w}\right), \tag{32}$$

where we have chosen i$s_{ant} = 0$, and noted that due to the vacuum dispersion relation, $\mathbf{K}_{w,ant} = 0$. The probe beam's electric field is thus

$$\mathbf{E}_b = A_{ant}\exp(\mathrm{i}\phi_G + \mathrm{i}\phi_P)\left[\frac{\det(\mathrm{Im}[\boldsymbol{\Psi}_w])}{\det(\mathrm{Im}[\boldsymbol{\Psi}_{w,ant}])}\right]^{\frac{1}{4}}\sqrt{\frac{g_{ant}}{g}}$$
$$\times\,\hat{\mathbf{e}}\exp\left(\mathrm{i}s + \mathrm{i}\mathbf{K}_w\cdot\mathbf{w} + \frac{\mathrm{i}}{2}\mathbf{w}\cdot\boldsymbol{\Psi}_w\cdot\mathbf{w}\right). \tag{33}$$

We then calculate this electric field by finding gradients of the dispersion relation H and using them to evolve the relevant quantities. We now proceed to describe our choice of dispersion relation, and the subtleties involved in doing this correctly.

2.2. Dispersion relation

In our derivation of beam tracing, the dispersion relation H is defined in equation (23). To calculate H, we first express the various components of the cold plasma dielectric tensor in the orthonormal basis $(\hat{\mathbf{u}}_1, \hat{\mathbf{u}}_2, \hat{\mathbf{b}})$. The $\hat{\mathbf{u}}_1$ and $\hat{\mathbf{u}}_2$ directions are perpendicular to $\hat{\mathbf{b}}$, and the $\hat{\mathbf{u}}_1$ direction together with $\hat{\mathbf{b}}$ defines a plane that contains $\mathbf{K}$, while $\hat{\mathbf{u}}_2$ is perpendicular to the plane of $\hat{\mathbf{b}}$ and $\mathbf{K}$. In this basis, we write the cold plasma dielectric tensor, given in equation (2), as

$$\boldsymbol{\epsilon} = \begin{pmatrix} \epsilon_{11} & -i\epsilon_{12} & 0 \\ i\epsilon_{12} & \epsilon_{11} & 0 \\ 0 & 0 & \epsilon_{bb} \end{pmatrix}, \tag{34}$$

where

$$\epsilon_{11} = 1 - \frac{\Omega_{pe}^2}{\Omega^2 - \Omega_{ce}^2}, \qquad \epsilon_{12} = \frac{\Omega_{pe}^2 \Omega_{ce}}{\Omega \left(\Omega^2 - \Omega_{ce}^2\right)}, \qquad \epsilon_{bb} = 1 - \frac{\Omega_{pe}^2}{\Omega^2}. \tag{35}$$

Here the subscripts $_1$, $_2$, and $_b$ denote the components in the $\hat{\mathbf{u}}_1$, $\hat{\mathbf{u}}_2$, and $\hat{\mathbf{b}}$ directions, respectively. The components of $\boldsymbol{D}$ are

$$\boldsymbol{D} = \begin{pmatrix} D_{11} & -iD_{12} & D_{1b} \\ iD_{12} & D_{22} & 0 \\ D_{1b} & 0 & D_{bb} \end{pmatrix}, \tag{36}$$

where

$$D_{11} = \epsilon_{11} - \frac{c^2}{\Omega^2} K^2 \sin^2 \theta_m, \tag{37}$$

$$D_{22} = \epsilon_{11} - \frac{c^2}{\Omega^2} K^2, \tag{38}$$

$$D_{bb} = \epsilon_{bb} - \frac{c^2}{\Omega^2} K^2 \cos^2 \theta_m, \tag{39}$$

$$D_{12} = \epsilon_{12}, \tag{40}$$

$$D_{1b} = \frac{c^2}{\Omega^2} K^2 \sin \theta_m \cos \theta_m. \tag{41}$$

Here, the mismatch angle θ_m is defined in Figure 2. We proceed to find the three eigenvalues of $\boldsymbol{D}$ in Appendix B; this requires solving a cubic equation, which we do with Cardano's formula. To evolve the beam, we would need to choose the eigenvalue that is zero along the entire path of the ray. Unfortunately, it is not immediately obvious which solutions correspond to the O and X modes. Moreover, Cardano's formula is complicated and cumbersome. Hence, we elect to use this form of the dispersion relation only in post-processing, but not to propagate the beam. We now prove that this is indeed a valid approach.

Instead of H, we used $\bar{H}\left(H(\mathbf{q}, \mathbf{K}), \mathbf{q}, \mathbf{K}\right)$, with the function $\bar{H}$ satisfying

$$\bar{H}(H = 0, \mathbf{q}, \mathbf{K}) = 0, \tag{42}$$

such that the derivatives of $\bar{H}$ with respect to $\mathbf{q}$ and $\mathbf{K}$ holding H constant vanish for $H = 0$. Bearing this in mind, we now evaluate the gradients of such an alternative dispersion relation, getting

$$\frac{\mathrm{d}\mathbf{K}}{\mathrm{d}\bar{\tau}} = -\nabla\bar{H}, \qquad \frac{\mathrm{d}\mathbf{q}}{\mathrm{d}\bar{\tau}} = \nabla_K\bar{H}, \tag{43}$$

and

$$\frac{\mathrm{d}\boldsymbol{\Psi}}{\mathrm{d}\bar{\tau}} = -\left(\boldsymbol{\Psi}\cdot\nabla_K\nabla_K\bar{H}\cdot\boldsymbol{\Psi} + \boldsymbol{\Psi}\cdot\nabla_K\nabla\bar{H} + \nabla\nabla_K\bar{H}\cdot\boldsymbol{\Psi} + \nabla\nabla\bar{H}\right), \tag{44}$$

where the new parameter $\bar{\tau}$ is defined by

$$\frac{\mathrm{d}\tau}{\mathrm{d}\bar{\tau}} = \frac{\partial\bar{H}}{\partial H}. \tag{45}$$

To obtain this result, we use equation (A.41) in the derivation of equation (44). Here the derivatives of $\bar{H}$ are evaluated without holding H fixed, that is

$$\frac{\partial\bar{H}}{\partial\alpha} = \left.\frac{\partial\bar{H}}{\partial H}\right|_{\mathbf{q},\mathbf{K}}\frac{\partial H}{\partial\alpha} + \frac{\partial\mathbf{q}}{\partial\alpha}\cdot\left.\nabla\bar{H}\right|_{H,\mathbf{K}} + \frac{\partial\mathbf{K}}{\partial\alpha}\cdot\left.\nabla_K\bar{H}\right|_{H,\mathbf{q}}. \tag{46}$$

Consequently, we can calculate the beam parameters $\mathbf{q}$, $\mathbf{K}$, and $\boldsymbol{\Psi}$ from $\bar{H}$ as they are unaffected by choosing a new dispersion relation.

In our implementation of beam tracing, which we later describe in Section 2.3, we make the following choice for the dispersion relation $\bar{H}$: the solution of the Booker quartic [69, 70]. Since at least one of the eigenvalues of $\boldsymbol{D}$ is always zero along the central ray, its determinant must also be zero, $\det\left(\boldsymbol{D}\right) = 0$. This turns out to be a quartic equation. Fortunately, this quartic is biquadratic, which makes it easier to solve than Cardano's formula. Hence, we have

$$\bar{H} = K^2\frac{c^2}{\Omega^2} + \frac{\beta\pm\sqrt{\beta^2 - 4\alpha\gamma}}{2\alpha} = 0, \tag{47}$$

where

$$\alpha = \epsilon_{bb}\sin^2\theta_m + \epsilon_{11}\cos^2\theta_m, \tag{48}$$

$$\beta = -\epsilon_{11}\epsilon_{bb}\left(1 + \sin^2\theta_m\right) - \left(\epsilon_{11}^2 - \epsilon_{12}^2\right)\cos^2\theta_m, \tag{49}$$

and

$$\gamma = \epsilon_{bb}\left(\epsilon_{11}^2 - \epsilon_{12}^2\right). \tag{50}$$

Recall that $\sin\theta_m$ is the mismatch angle, see Figure 2. The sign of the square root in equation (47) is chosen based on the mode. To figure out which sign corresponds to which mode, we consider the case where $\theta_m = 0$, getting

$$\frac{\beta\pm\sqrt{\beta^2 - 4\alpha\gamma}}{2\alpha} = \frac{-\epsilon_{11}^2 + \epsilon_{12}^2 - \epsilon_{11}\epsilon_{bb} \pm |\epsilon_{11}^2 - \epsilon_{12}^2 - \epsilon_{11}\epsilon_{bb}|}{2\epsilon_{11}}. \tag{51}$$

We need to choose the signs such that we recover $K^2c^2/\Omega^2 = \epsilon_{bb}$ for the O mode and $K^2c^2/\Omega^2 = \epsilon_{11} + \epsilon_{12}/\epsilon_{11}$ for the X mode. Thus, if $\epsilon_{11}^2 - \epsilon_{12}^2 - \epsilon_{11}\epsilon_{bb} > 0$, the $+$ of the $\pm$ corresponds to the O mode. If it is less than zero, then $-$ of the $\pm$ corresponds to the

O mode. The other sign, in either case, would correspond to the X mode. One selects the appropriate sign, and uses this $\bar{H}(H, \mathbf{q}, \mathbf{K})$ in place of H to find $\mathbf{q}$, $\mathbf{K}$, and $\boldsymbol{\Psi}$.

There are a few quantities that depend on the definition of H given in equation (23). These are equations (29), (30), and (31). In particular, the exact definition of g in equation (29) is crucial for our result on localisation in Section 8. Our calculation of group velocity is dependent on the choice of dispersion relation, since

$$\bar{\mathbf{g}} = \frac{\mathrm{d}\tau}{\mathrm{d}\bar{\tau}} \frac{\mathrm{d}\mathbf{q}}{\mathrm{d}\tau}, \tag{52}$$

where the dependence of $\mathrm{d}\tau/\mathrm{d}\bar{\tau}$ on our choice of H is given in equation (45). We use Cardano's solution in equations (B.6), (B.7), and (B.8) in post-processing to determine g_{ant} and g in equation (33) consistent with our definition of H.

Having explained how to handle the subtleties of the dispersion relation, we proceed to describe the code used to solve the beam-tracing equations and determine the probe beam's electric field.

2.3. Beam tracer: Scotty

To simulate the propagation of Gaussian beams in tokamak plasmas, we have developed a new code, Scotty. It is a beam-tracing code written in Python 3, entirely in cylindrical coordinates (R, ζ, Z), with an option to convert the output to Cartesian coordinates (X, Y, Z). This exploits the toroidal symmetry of tokamak plasmas, simplifying the beam tracing equations. Hence, although the theoretical work presented in this paper is applicable to stellarators (in regions where the appropriate orderings and approximations hold), Scotty cannot be used out-of-the-box for such devices. Nonetheless, the results presented in this paper would still be applicable; one would simply need to run a suitable beam-tracing code and post-process the output appropriately.

In cylindrical coordinates, we have $H(R, Z, K_R, K_\zeta, K_Z)$: a very natural choice of variables for a tokamak. The new spatial coordinates R, Z, ζ are defined as follows

$$R = \sqrt{X^2 + Y^2}, \tag{53}$$

$$\zeta = \tan^{-1}\left(\frac{Y}{X}\right), \tag{54}$$

$$Z = Z. \tag{55}$$

The components of $\mathbf{K}$ in the new coordinate system are

$$K_R = K_X \cos\zeta + K_Y \sin\zeta, \tag{56}$$

$$K_\zeta = (-K_X \sin\zeta + K_Y \cos\zeta)\sqrt{X^2 + Y^2}, \tag{57}$$

and

$$K_Z = K_Z. \tag{58}$$

Note that K_ζ is the toroidal mode number, and is thus dimensionless, instead of having units of inverse length (unlike the other components of the wavevector). Hence, $\mathbf{K}$ becomes

$$\mathbf{K} = K_R \nabla R + K_\zeta \nabla \zeta + K_Z \nabla Z, \tag{59}$$

being careful to remember that we have $\nabla R = \hat{\mathbf{R}}$, $\nabla Z = \hat{\mathbf{Z}}$, but $\nabla \zeta = \hat{\boldsymbol{\zeta}}/R$.

Since Scotty was inspired by TORBEAM [54], it has the option to use the same input files for equilibrium data: specifically, $\mathbf{B}$ and the poloidal flux ψ_p on a grid (R and Z), as well as electron density as a function of radial coordinate $\sqrt{\psi_p}$. We split the magnetic field into toroidal and poloidal components,

$$\mathbf{B} = B_\zeta \hat{\boldsymbol{\zeta}} + B_R \hat{\mathbf{R}} + B_Z \hat{\mathbf{Z}}, \tag{60}$$

where B_ζ is the toroidal component of the magnetic field, and B_R and B_Z are its poloidal components. Scotty can also calculate $\mathbf{B}$ directly from EFIT [71, 72] output: this is done by using RB_ζ, given in the EFIT output, and numerically evaluating the gradients of ψ_p. The magnetic field is calculated as follows:

$$B_R = -\frac{1}{R}\frac{\partial \psi_p}{\partial Z}, \tag{61}$$

$$B_\zeta = \frac{1}{R}I\left(\psi_p(R, Z)\right), \tag{62}$$

where I is proportional to the poloidal current, an output of EFIT, and

$$B_Z = \frac{1}{R}\frac{\partial \psi_p}{\partial R}. \tag{63}$$

Scotty assumes lossless propagation as it is written specially for DBS. Since we use Mega Ampere Spherical Tokamak (MAST) plasmas as a case study in this work, we do not need to account for the relativistic correction to the electron mass. As such, in its current implementation Scotty does not use temperature profiles, although we expect to add the relativistic correction in the near future.

In its current implementation, Scotty matches boundary conditions at the plasma-vacuum edge, using the generalised Snell's law [53] for $\boldsymbol{\Psi}$ (like TORBEAM) but not for $\mathbf{K}$ (unlike TORBEAM). Consequently, a possible discontinuity in $\nabla\nabla H$ arising from a sudden change in the density gradient is properly handled; see Appendix C for details.

The definitions of K_R, K_ζ, K_Z, in equations (56), (57), and (58), were chosen such that the electric field has the form:

$$\begin{aligned}
\mathbf{E}_b \propto \exp\Big[&\mathrm{i}s + \mathrm{i}K_R\Delta R + \mathrm{i}K_Z\Delta Z + \mathrm{i}K_\zeta\Delta\zeta \\
&+ \frac{\mathrm{i}}{2}(\Psi_{RR}\left(\Delta R\right)^2 + 2\Psi_{RZ}\Delta R\Delta Z + \Psi_{ZZ}\left(\Delta Z\right)^2 \\
&+ \Psi_{\zeta\zeta}\left(\Delta\zeta\right)^2 + 2\Psi_{R\zeta}\Delta R\Delta\zeta + 2\Psi_{\zeta Z}\Delta\zeta\Delta Z)\Big],
\end{aligned} \tag{64}$$

which gives us the definitions of the components of $\boldsymbol{\Psi}$ in cylindrical coordinates. The components Ψ_{RR}, Ψ_{ZZ}, $\Psi_{\zeta\zeta}$, Ψ_{RZ}, $\Psi_{R\zeta}$, and $\Psi_{Z\zeta}$ of the matrix $\boldsymbol{\Psi}$ in the new coordinate system must satisfy

$$\Psi_{\alpha\beta}(\tau) = \frac{\partial^2 \psi}{\partial r_\alpha \partial r_\beta}\left(\tau, w_x = 0, w_y = 0\right). \tag{65}$$

Hence, they are

$$\Psi_{RR} = \Psi_{XX}\cos^2\zeta + 2\Psi_{XY}\sin\zeta\cos\zeta + \Psi_{YY}\sin^2\zeta, \tag{66}$$

$$\Psi_{ZZ} = \Psi_{ZZ}, \tag{67}$$

$$\Psi_{\zeta\zeta} = \left[\Psi_{XX}\sin^2\zeta - 2\Psi_{XY}\sin\zeta\cos\zeta + \Psi_{YY}\cos^2\zeta\right]\left(X^2 + Y^2\right)$$
$$- \left(K_X\cos\zeta + K_Y\sin\zeta\right)\sqrt{X^2 + Y^2}, \tag{68}$$

$$\Psi_{RZ} = \Psi_{XZ}\cos\zeta + \Psi_{YZ}\sin\zeta, \tag{69}$$

$$\Psi_{R\zeta} = \left[-\Psi_{XX}\sin\zeta\cos\zeta + \Psi_{XY}\left(\cos^2\zeta - \sin^2\zeta\right) + \Psi_{YY}\sin\zeta\cos\zeta\right]\sqrt{X^2 + Y^2}$$
$$- K_X\sin\zeta + K_Y\cos\zeta, \tag{70}$$

$$\Psi_{Z\zeta} = \left(-\Psi_{XZ}\sin\zeta + \Psi_{YZ}\cos\zeta\right)\sqrt{X^2 + Y^2}. \tag{71}$$

The rest of the elements can be found by remembering that $\boldsymbol{\Psi}$ is symmetric.

With these new variables, the gradients become

$$\nabla = \nabla R\frac{\partial}{\partial R} + \nabla\zeta\frac{\partial}{\partial\zeta} + \nabla Z\frac{\partial}{\partial Z}, \tag{72}$$

and

$$\nabla_K = \nabla_K K_R\frac{\partial}{\partial K_R} + \nabla_K K_\zeta\frac{\partial}{\partial K_\zeta} + \nabla_K K_Z\frac{\partial}{\partial K_Z}. \tag{73}$$

Using all these properties, we can write the evolution equations in a way which makes their Hamiltonian character explicit,

$$\frac{\mathrm{d}q_\alpha}{\mathrm{d}\tau} = \frac{\partial H}{\partial K_\alpha}, \tag{74}$$

$$\frac{\mathrm{d}K_\alpha}{\mathrm{d}\tau} = -\frac{\partial H}{\partial r_\alpha}, \tag{75}$$

and

$$\frac{\mathrm{d}\Psi_{\alpha\beta}}{\mathrm{d}\tau} = -\frac{\partial^2 H}{\partial r_\alpha\partial r_\beta} - \Psi_{\alpha\gamma}\frac{\partial^2 H}{\partial K_\gamma\partial r_\beta} - \frac{\partial^2 H}{\partial r_\alpha\partial K_\eta}\Psi_{\eta\beta} - \Psi_{\alpha\gamma}\frac{\partial^2 H}{\partial K_\gamma\partial K_\eta}\Psi_{\eta\beta}. \tag{76}$$

Here we note that while $\mathrm{d}q_\zeta/\mathrm{d}\tau = \partial H/\partial K_\zeta$, the corresponding component of group velocity, given by

$$\mathbf{g} = \nabla_K H, \tag{77}$$

is $g_\zeta = R\,\partial H/\partial K_\zeta$; $\mathrm{d}q_\zeta/\mathrm{d}\tau = \partial H/\partial K_\zeta$ is an angular velocity, while g_ζ is a linear velocity, and they have different units.

Moving forward, the most obvious simplification to the above equations is due to toroidal symmetry: spatial gradients of equilibrium properties in the toroidal direction are zero, that is, $\partial H/\partial\zeta = 0$.

We proceed to solve these equations numerically, evolving $\boldsymbol{\Psi}$, from which $\boldsymbol{\Psi}_w$ may be obtained. Since $\boldsymbol{\Psi}$ is symmetric, it only has six independent components. We can further reduce the number of such components: equation (A.41) means we can reduce it

by three. Hence, it is in principle possible to solve for only three independent components of $\boldsymbol{\Psi}$. However, we deemed the implementation too complex given the unclear benefits, which is why we have made a conscious design decision to solve for all six components

The initial conditions required by Scotty for the beam are as follows: frequency, initial beam widths and curvatures, poloidal φ_p and toroidal φ_t launch angles, and launch position. Note that only the initial q_R and q_Z need to be specified. The toroidal angle is taken to be zero at launch, $q_\zeta = 0$. The launch angles are defined the same way as TORBEAM [54], and are used to initialise $\mathbf{K}_{ant}$ as follows,

$$
\begin{aligned}
K_{R,ant} &= -\frac{\Omega}{c}\cos\varphi_t \cos\varphi_p, \\
K_{\zeta,ant} &= -\frac{\Omega}{c} R_{ant} \sin\varphi_t \cos\varphi_p, \\
K_{Z,ant} &= -\frac{\Omega}{c}\sin\varphi_p.
\end{aligned}
\tag{78}
$$

Scotty uses SciPy's initial value problem solver to evolve the beam tracing ODEs. The solver has the option to easily switch between various integration methods. For this paper, we use an explicit Runge-Kutta method of order 5(4) [73, 74].

Having broadly described the workings of Scotty, we lay out the parameters for two test scenarios that we use throughout the rest of the paper to illustrate our analytical results.

2.4. Test scenarios

Throughout the rest of this paper, we use two test scenarios to illustrate our results. One of these scenarios uses equilibrium data from a real shot which was carried out at MAST, while the other is entirely analytical. We detail these two scenarios here, and unless otherwise stated in subsequent sections, the parameters here are what we then use. In both scenarios, the probe beam's frequency was taken to be 55 GHz with O-mode polarisation.

To illustrate our model's ability to deal with real plasmas, we chose MAST shot 29908, at 190ms. This was one of six repeated shots used to study the effect of mismatch in an earlier paper [30], in which DBS data was analysed for these shots at 190ms. The RB_ζ and the normalised poloidal flux density ψ_p were determined by MSE-constrained EFIT, and we used equations (61), (62), and (63) to calculate $\mathbf{B}$. We used SciPy's bivariate spline to interpolate ψ_p [73]. To ensure that the second spatial derivatives are smooth, we used a degree of 5 and a smoothing factor of 2. This does not significantly change the poloidal flux profile, as can be seen from Figure 3.

The density profile was acquired by Thomson scattering [75]. We chose to fit the density data rather than smooth it because it was noisy, which made the evaluation of $\nabla\nabla n$, and thus $d\boldsymbol{\Psi}/d\tau$, challenging. Since data processing is not the main focus of this paper, we instead use the following function to fit the density data

$$
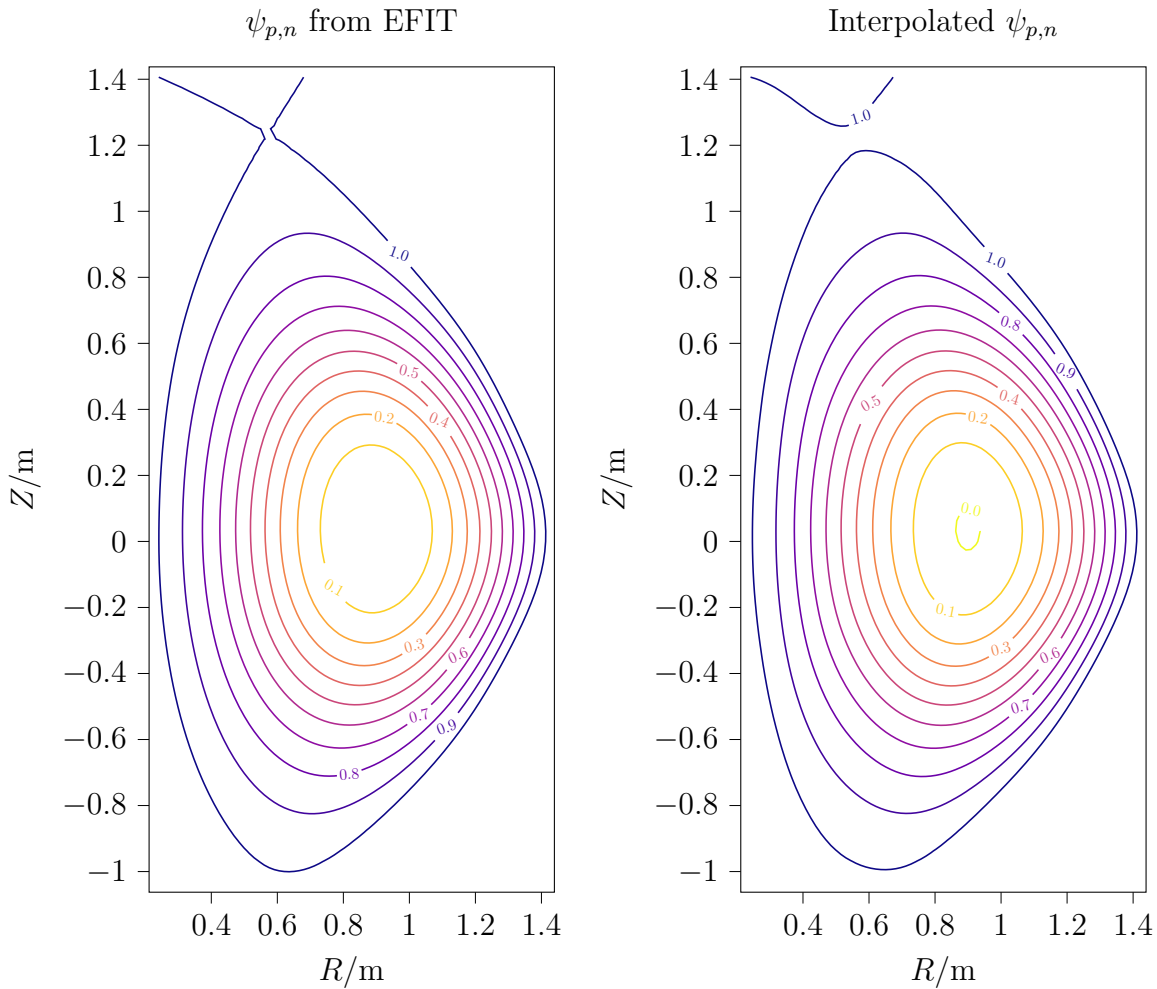n_e = C_1 \tanh\left[C_2\left(\psi_{p,n} - C_3\right)\right],
\tag{79}
$$

Figure 3: Data from MSE-constrained EFIT (left), after smoothing (right). Here $\psi_{p,n}$ is the normalised ψ_p such that $\psi_{p,n} = 1$ on the last closed flux surface and $\psi_{p,n} = 0$ on the magnetic axis (left). The smoothing spline (right) gives $\psi_{p,n} < 0$ in a region of space near the magnetic axis. Thankfully, the beam is never in that region in the simulations used for this paper, so this is not an issue.

where $\psi_{p,n}$ is the normalised ψ_p such that $\psi_{p,n} = 1$ on the last closed flux surface and $\psi_{p,n} = 0$ on the magnetic axis. The coefficients $C_1 = 3.25 \times 10^{19} \mathrm{m}^{-3}$, $C_2 = -2.4$, and $C_3 = 1.22$ were determined via manual fitting by visual inspection. These coefficients were used by Scotty directly to calculate the density. Notice that the fit gives negative densities for $\psi_{p,n} > C_3$; at these values of ψ, the density is set to 0. The fit is not particularly good when $\psi_{p,n} \lesssim 0.4$; the experimental density profile is hollow. Fortunately, this is not a problem for the current work, since the beams studied in this paper do not enter that region.

We launch a circular beam, at $q_R = 2.44\mathrm{m}$ and $q_Z = 0\mathrm{m}$, with $\varphi_p = 6°$, $\varphi_t = -6.4°$, $R_{b,x} = R_{b,y} = -72.8\mathrm{cm}$, and $W_x = W_y = 3.97\mathrm{cm}$. The launch beam's width and curvature were obtained from E-plane measurements of the 50 GHz beam of the MAST
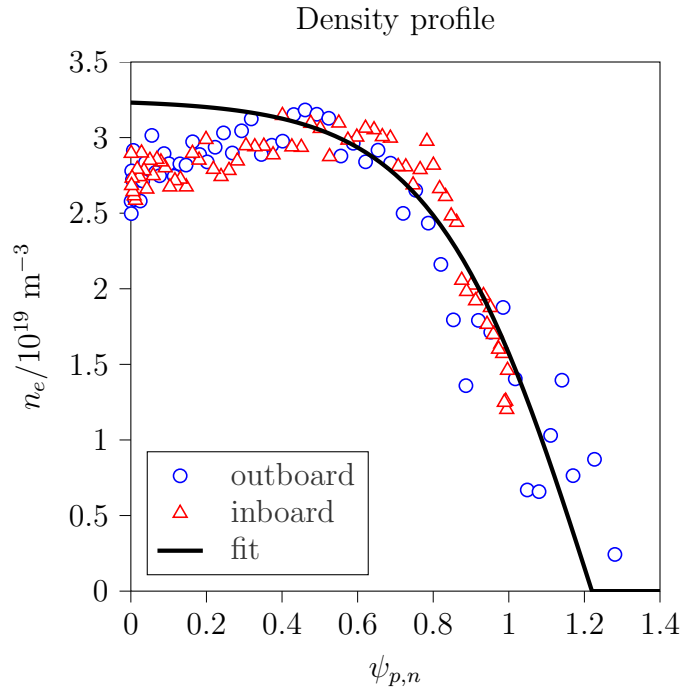
Density profile

Figure 4: Electron density n_e data from the Thomson scattering diagnostic as a function of normalised poloidal flux (blue circles and red triangles, denoting measurements on the outboard and inboard respectively), hyperbolic tangent fit (black line). The fit is less good when $\psi_{p,n} \lesssim 0.4$; the experimental density profile is hollow. Fortunately, this is not a problem for the current work, since the beams studied in this paper do not enter that region.

DBS; this is a focusing rather than a diverging beam, with the beam waist roughly located at the MAST port window [30]. This beam propagates through the plasma as given in Figure 5.

For our analytical equilibrium, we use a large aspect ratio, circular flux surface equilibrium. The toroidal component is given by

$$B_\zeta = B_{\zeta,a} \frac{R_a}{R}, \tag{80}$$

where R_a is the R of the magnetic axis and $B_{\zeta,a}$ is the corresponding toroidal magnetic field at the said axis. The poloidal field inside the last closed flux surface, $(R - R_a)^2 + Z^2 = a^2$, where a is the minor radius, is

$$B_R = B_p \frac{Z}{\sqrt{(R - R_a)^2 + Z^2}}, \tag{81}$$

and

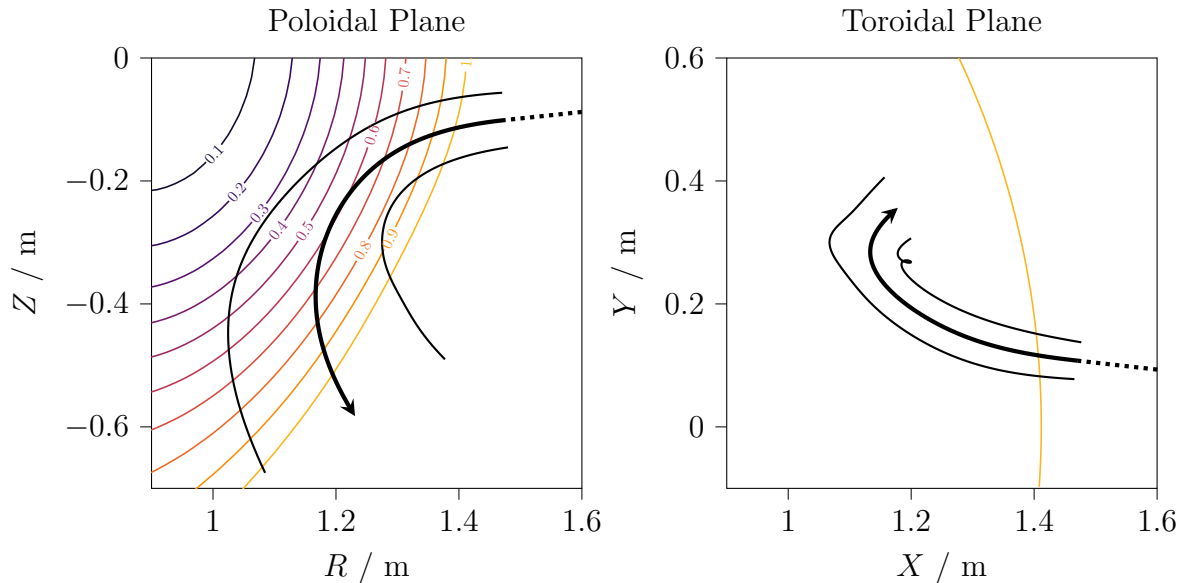$$B_Z = B_p \frac{R - R_a}{\sqrt{(R - R_a)^2 + Z^2}}. \tag{82}$$

Figure 5: Beam propagation through MAST plasma, shot 29908 at 190ms. Poloidal (left) and toroidal (right) cross-sections. The orange line in the right figure shows the radial position of the last closed flux surface at the midplane. Thin solid black lines give the 1/e positions of the Gaussian beam's electric field and the dotted lines show the ray's propagation in vacuum. The beam is launched from the steering mirror, located on the midplane at $R = 2.4$m, which is out of the graph's boundaries. Thick solid black lines indicate trajectory of the central ray and the arrow the direction of propagation. Notice that the thin solid line loops upon itself in the figure on the right: this is not an artefact but the result of the beam widening as it turns and travels a significant distance in the poloidal plane, while not propagating quite as far in the toroidal plane.

Here, inside the last closed flux surface, we have

$$B_p = B_{p,a} \frac{\sqrt{(R - R_a)^2 + Z^2}}{a},$$

(83)

where $B_{p,a}$ is the magnitude of the poloidal magnetic field on the last closed flux surface. Unless otherwise stated, we use $B_{p,a} = 0.1$T, $B_{\zeta,a} = 1$T, $R_a = 1.5$m, and $a = 0.5$m. The density profile was linear in $\sqrt{\psi_p}$, going from $n_e = 4 \times 10^{19}$m^{-3} at $\sqrt{\psi_p} = 0$ to zero density at $\sqrt{\psi_p} = 1$. A circular beam is launched at $q_R = 2.2$m and $q_Z = 0$m, with $\varphi_p = 6°$, $\varphi_t = 0°$, $R_{b,x} = R_{b,y} = -4.0$m, and $W_x = W_y = 4$cm.

3. Reciprocity theorem

The exact expression for the scattered electric field $\mathbf{E}_s$ is complicated. Coherent scattering in fusion plasmas has been studied extensively in cases where the wave frequency is much larger than the plasma frequency [76, 77, 78]. Since the frequency of the DBS beam is close to the plasma frequency, refraction is significant, making analysis even more challenging. Fortunately, we know that the emitted and received

patterns of the antenna are the same. To simplify the subsequent equations, we define the antenna surface to be a surface perperpendicular to the beam propagation and close to the physical antenna. For the antenna to receive a wave, it must be of the same form as the emitted wave, shown in equation (32), but time reversed. Since the received and emitted waves are travelling in opposite directions, their wavevectors and beamfront curvatures, given by $\mathrm{Re}(\boldsymbol{\Psi})$, have opposite signs. The received and emitted waves must also have the same envelope, given by $\mathrm{Im}(\boldsymbol{\Psi})$, to pass through the optics of the DBS system. The polarisation of the emitted wave must be the same as that of the received wave. For example, an antenna emitting right circularly polarised light must also receive right circularly polarised light. However, the direction of travel has changed, and thus the direction the polarisation is moving also changes, as one might expect from time reversal symmetry. The received polarisation is thus the complex conjugate of that emitted. Consequently, at the antenna, the received scattered electric field must satisfy

$$\mathbf{E}_{r,ant} = A_r \hat{\mathbf{e}}_{ant}^* \exp\left(-\frac{\mathrm{i}}{2}\mathbf{w} \cdot \boldsymbol{\Psi}_{w,ant}^* \cdot \mathbf{w}\right), \tag{84}$$

where we have assumed that the antenna is in a vacuum and that the probe beam is launched perpendicular to the antenna surface. The scattered wave will be detected by the antenna if and only if it is of the form in equation (84).

To calculate A_r for a given $\mathbf{E}_s$, we project the scattered electric field on the Gaussian beam mode, the lowest order mode of the Gauss-Hermite beams, which form an orthogonal basis [79, 80],

$$A_r = \pi^{-1} \left[\det\left[\mathrm{Im}\left(\boldsymbol{\Psi}_{w,ant}\right)\right]\right]^{\frac{1}{2}} \int_{ant} \left[\mathbf{E}_s \cdot \hat{\mathbf{e}}_{ant} \exp\left(\frac{\mathrm{i}}{2}\mathbf{w} \cdot \boldsymbol{\Psi}_{w,ant} \cdot \mathbf{w}\right)\right] \mathrm{d}S. \tag{85}$$

The $\pi^{-1} \left[\det\left[\mathrm{Im}\left(\boldsymbol{\Psi}_{w,ant}\right)\right]\right]^{1/2}$ piece is the reciprocal of what we would get if we evaluated the 2D Gaussian surface integral with standard contour integration methods, taking care to choose the signs of the roots carefully. We have assumed that the DBS optics produces a sufficiently good Gaussian beam, such that the contribution to the signal from higher order modes is negligible.

We use reciprocity to obtain A_r without calculating $\mathbf{E}_s$ in its entirety. The reciprocity theorem is a standard method of calculating the signal received by an antenna. However, it cannot be used in its usual form when the medium is a magnetised plasma. In order to deal with highly magnetised plasmas in tokamaks, some modifications have to be made. Specifically, the reciprocal beam has to be launched into a plasma which has its dielectric tensor transposed [81, 23, 24, 82], which is the same as having its magnetic field reversed. The dielectric tensor has to be transposed to maintain time reversal symmetry. Like previous work on reciprocity, we use the superscript $^{(+)}$ to denote solutions in the medium with the transposed dielectric tensor, which is

$$\frac{c^2}{\Omega^2}\nabla \times \left(\nabla \times \mathbf{E}^{(+)}\right) = \boldsymbol{\epsilon}_{eq}^T \cdot \mathbf{E}^{(+)}. \tag{86}$$

To obtain A_r in equation (85), we contract equation (5) with $\mathbf{E}^{(+)}$,

$$\frac{c^2}{\Omega^2}\mathbf{E}^{(+)} \cdot \nabla \times (\nabla \times \mathbf{E}_s) = \mathbf{E}^{(+)} \cdot \boldsymbol{\epsilon}_{eq} \cdot \mathbf{E}_s + \mathbf{E}^{(+)} \cdot \boldsymbol{\epsilon}_{tb} \cdot \mathbf{E}_b, \tag{87}$$

and integrate by parts, using equation (86) to obtain

$$\frac{c^2}{\Omega^2}\nabla \cdot [(\nabla \times \mathbf{E}_s) \times \mathbf{E}^{(+)} - (\nabla \times \mathbf{E}^{(+)}) \times \mathbf{E}_s] = \mathbf{E}^{(+)} \cdot \boldsymbol{\epsilon}_{tb} \cdot \mathbf{E}_b. \tag{88}$$

Choosing the right surface and the right boundary condition for $\mathbf{E}^{(+)}$ on that surface, one can calculate A_r from a volume integral of $\mathbf{E}^{(+)} \cdot \boldsymbol{\epsilon}_{tb} \cdot \mathbf{E}_b$,

$$\int [(\nabla \times \mathbf{E}_s) \times \mathbf{E}^{(+)} + \mathbf{E}_s \times (\nabla \times \mathbf{E}^{(+)})] \cdot \mathrm{d}\mathbf{S} = \int \frac{\Omega^2}{c^2}\mathbf{E}^{(+)} \cdot \boldsymbol{\epsilon}_{tb} \cdot \mathbf{E}_b \,\mathrm{d}V. \tag{89}$$

We impose that $\mathbf{E}^{(+)}$ at the antenna is

$$\mathbf{E}_{ant}^{(+)} = \pi^{-1} \left\{\det\left[\mathrm{Im}\left(\boldsymbol{\Psi}_{w,ant}\right)\right]\right\}^{\frac{1}{2}} \hat{\mathbf{e}}_{ant} \exp\left(\frac{\mathrm{i}}{2}\mathbf{w} \cdot \boldsymbol{\Psi}_{w,ant} \cdot \mathbf{w}\right). \tag{90}$$

The behaviour of $\mathbf{E}^{(+)}$ as it propagates into the transposed plasma is governed by the beam tracing equations. The beam's evolution is governed by the dispersion relation $\boldsymbol{D} \cdot \hat{\mathbf{e}} = 0$, where $\boldsymbol{D}$ was defined in equation (22). When the dielectric tensor of the plasma is transposed, the dispersion relation is $\boldsymbol{D}^T \cdot \hat{\mathbf{e}}^{(+)} = 0$. The fact that $\boldsymbol{D}$ is Hermitian implies that $\boldsymbol{D}^\dagger \cdot \hat{\mathbf{e}} = 0$. Thus, $\boldsymbol{D}^T \cdot \hat{\mathbf{e}}^* = 0$, and we conclude that $\hat{\mathbf{e}}^{(+)} = \hat{\mathbf{e}}^*$. Intuitively, this makes sense, since transposing the dielectric tensor corresponds to switching the direction of the magnetic field; hence, left-handed polarisation in the transposed plasma behaves the same as right-handed polarisation in the physical plasma and vice versa. As such, the reciprocal beam $\mathbf{E}^{(+)}$ propagates like the probe beam $\mathbf{E}_b$, except for its polarisation being complex conjugated. Since $\mathbf{E}^{(+)}$ at the antenna, equation (90), has the same form as $\mathbf{E}_b$ at the antenna and follows the same set of evolution equations, except for the complex conjugated polarisation, the reciprocal beam is

$$\mathbf{E}^{(+)} = \pi^{-1} \sum_{i=O,X} \alpha_i \left\{\det\left[\mathrm{Im}\left(\boldsymbol{\Psi}_{w,ant}\right)\right]\right\}^{\frac{1}{4}} \left\{\det\left[\mathrm{Im}\left(\boldsymbol{\Psi}_{w,i}\right)\right]\right\}^{\frac{1}{4}} \left(\frac{g_{ant}}{g_i}\right)^{\frac{1}{2}}$$
$$\times \hat{\mathbf{e}}_i^* \exp(\mathrm{i}\phi_{G,i} - \mathrm{i}\phi_{P,i}) \exp\left(\mathrm{i}s_i + \mathrm{i}\mathbf{K}_{w,i} \cdot \mathbf{w}_i + \frac{\mathrm{i}}{2}\mathbf{w}_i \cdot \boldsymbol{\Psi}_{w,i} \cdot \mathbf{w}_i\right), \tag{91}$$

where the coefficients α_i give the relative amplitudes of the O and X modes. We remark that ϕ_G does not change sign, unlike ϕ_P. We now match the expression for the reciprocal electric field, equation (91), with its initial condition, equation (90), giving

$$\hat{\mathbf{e}}_{ant} = \alpha_{O,ant}\hat{\mathbf{e}}_{O,ant}^* + \alpha_{X,ant}\hat{\mathbf{e}}_{X,ant}^*. \tag{92}$$

Since the dispersion relation $\boldsymbol{D}$ is Hermitian, its eigenvectors are orthogonal: $\hat{\mathbf{e}}_X \cdot \hat{\mathbf{e}}_O^* = 0$ and $\hat{\mathbf{e}}_O \cdot \hat{\mathbf{e}}_X^* = 0$. We contract equation (92) with $\hat{\mathbf{e}}_O^*$ and $\hat{\mathbf{e}}_X^*$ in turn, finding

$$\alpha_O = \hat{\mathbf{e}}_{ant} \cdot \hat{\mathbf{e}}_{O,ant}, \tag{93}$$

and

$$\alpha_X = \hat{\mathbf{e}}_{ant} \cdot \hat{\mathbf{e}}_{X,ant}. \tag{94}$$

Having found the coefficients for the O and X modes, we now explicitly have an expression for $\mathbf{E}^{(+)}$.

We proceed by evaluating the integral on the left side of equation (89) over a surface which both contains the antenna and is far enough from the plasma that we can write $\mathbf{E}_s$ as a summation of plane waves,

$$\mathbf{E}_s = \sum_{\mathbf{K}_s} \mathbf{A}_s \exp(\mathrm{i}\mathbf{K}_s \cdot \mathbf{r}), \tag{95}$$

which we can do because the antenna is typically situated away from the plasma. Due to the vacuum dispersion relation, the scattered microwaves at the antenna have almost the same wavenumber as that emitted, Ω/c, at the antenna. The integrand of the surface integral in equation (89) is

$$
\begin{aligned}
(\nabla \times \mathbf{E}_s) &\times \mathbf{E}^{(+)} + \mathbf{E}_s \times (\nabla \times \mathbf{E}^{(+)}) \\
&\simeq \sum_{\mathbf{K}_s} \left[\mathrm{i}(\mathbf{K}_s \cdot \mathbf{E}^{(+)})\mathbf{A}_s - \mathrm{i}(\mathbf{A}_s \cdot \mathbf{E}^{(+)})\mathbf{K}_s \right] \exp(\mathrm{i}\mathbf{K}_s \cdot \mathbf{r}) \\
&+ \sum_{\mathbf{K}_s} \left[\mathrm{i}(\mathbf{A}_s \cdot \mathbf{E}^{(+)})\mathbf{K} - \mathrm{i}(\mathbf{K} \cdot \mathbf{A}_s)\mathbf{E}^{(+)} \right] \exp(\mathrm{i}\mathbf{K}_s \cdot \mathbf{r}),
\end{aligned}
\tag{96}
$$

where we have used $\nabla \mathbf{E}^{(+)} \simeq \mathrm{i}\mathbf{K}\mathbf{E}^{(+)}$. At the antenna, $\mathbf{K}$ is normal to the surface, and as a result its electric field is parallel to the surface. Moreover, at the antenna, $\mathbf{E}^{(+)} \propto \exp(\mathrm{i}K_g\hat{\mathbf{g}} \cdot \mathbf{r})$, and any term that contains an $\mathbf{A}_s$ with $\mathbf{K}_s$ not exactly perpendicular to the surface of the antenna integrates to zero. Therefore, $\int \sum_{\mathbf{K}_s} (\mathbf{K}_s \cdot \mathbf{E}^{(+)})[\mathbf{A}_s \exp(\mathrm{i}\mathbf{K}_s \cdot \mathbf{r})] \cdot \mathrm{d}\mathbf{S} = 0$. Similarly, $\int (\mathbf{K} \cdot \mathbf{E}_s)\mathbf{E}^{(+)} \cdot \mathrm{d}\mathbf{S} = 0$. The scattered waves are always travelling out of the plasma; the probe beam is also travelling out of the plasma at all points, except at the antenna. Consequently, the terms that contain $\mathbf{A}_s \cdot \mathbf{E}^{(+)}$ cancel at all points other than on the antenna. The surface integral in equation (89) is thus

$$
\begin{aligned}
\int [(\nabla \times \mathbf{E}_s) \times \mathbf{E}^{(+)} + \mathbf{E}_s \times (\nabla \times \mathbf{E}^{(+)})] \cdot \mathrm{d}\mathbf{S} &= -\int_{ant} 2\mathrm{i}\frac{\Omega}{c}\mathbf{E}_s \cdot \mathbf{E}^{(+)}\mathrm{d}S \\
&= -2\mathrm{i}\frac{\Omega}{c}A_r.
\end{aligned}
\tag{97}
$$

Here we have used the fact that the wavenumbers are Ω/c since the antenna is in vacuum. Hence, we get the reciprocity relation

$$A_r = \frac{\Omega\mathrm{i}}{2c} \int \mathbf{E}^{(+)} \cdot \boldsymbol{\epsilon}_{tb} \cdot \mathbf{E}_b \, \mathrm{d}V. \tag{98}$$

Before we conclude this section, we first show that this equation can be further simplified. We use the microwave and reciprocal electric fields, as well as the linearised dielectric tensor, in the reciprocity theorem. Substituting equations (3), (33), (91), (93),

and (94) into the volume integral of the reciprocity theorem, equation (98), we get

$$
\begin{aligned}
A_r = {} & \frac{\mathrm{i}\Omega A_{ant}}{2\pi c} \int \sum_{i=O,X} \hat{\mathbf{e}}_{ant} \cdot \hat{\mathbf{e}}_{i,ant} \left\{ \det \left[\mathrm{Im}\left(\boldsymbol{\Psi}_{w,i} \right) \right] \right\}^{\frac{1}{4}} \left(\frac{g_{ant}}{g_i} \right)^{\frac{1}{2}} \\
& \times \exp(\mathrm{i}\phi_{G,i} - \mathrm{i}\phi_{P,i}) \exp\left(\mathrm{i}s_i + \mathrm{i}\mathbf{K}_{w,i} \cdot \mathbf{w}_i + \frac{\mathrm{i}}{2}\mathbf{w}_i \cdot \boldsymbol{\Psi}_{w,i} \cdot \mathbf{w}_i \right) \\
& \times \frac{\delta n_e}{n_e} \hat{\mathbf{e}}_i^* \cdot \left(\boldsymbol{\epsilon}_{eq} - \mathbf{1} \right) \cdot \hat{\mathbf{e}} \ \exp(\mathrm{i}\phi_G + \mathrm{i}\phi_P) \left\{ \det \left[\mathrm{Im}\left(\boldsymbol{\Psi}_w \right) \right] \right\}^{\frac{1}{4}} \left(\frac{g_{ant}}{g} \right)^{\frac{1}{2}} \\
& \times \exp\left(\mathrm{i}s + \mathrm{i}\mathbf{K}_w \cdot \mathbf{w} + \frac{\mathrm{i}}{2}\mathbf{w} \cdot \boldsymbol{\Psi}_w \cdot \mathbf{w} \right) \ \mathrm{d}V.
\end{aligned}
\tag{99}
$$

Here we have assumed that the polarisation of the probe beam is appropriately well-matched to the pitch angle at the plasma edge, such that only one mode, either O or X, propagates into the plasma. If this assumption does not hold, then one should calculate A_r for each probe beam mode separately and add the two together. To simplify the above expression, equation (99), and thus the subsequent algebra, we first make an argument about the contribution of the reciprocal electric field to the backscattered amplitude.

In general, the O and X modes take different paths through the plasma, even if they enter the plasma at the same point. For a given polarisation of the probe beam $\mathbf{E}_b$, the reciprocal beam with the same polarisation will follow the same path as the probe beam, and the reciprocal beam with the opposite polarisation follows a different path. As a result, the reciprocal beam with the same polarisation as the probe beam overlaps with the probe beam over a volume of order $W^2 L$, whereas the reciprocal beam with the opposite polarisation in general overlaps only over a small volume W^3. Since the contribution to the integral from the reciprocal beam with the opposite polarisation to the probe beam is small by $W/L \ll 1$, equation (99) simplifies to

$$
\begin{aligned}
A_r = {} & \frac{\mathrm{i}\Omega A_{ant}}{2\pi c} \hat{\mathbf{e}}_{ant} \cdot \hat{\mathbf{e}}_{ant} \int \left[\det[\mathrm{Im}(\boldsymbol{\Psi}_w)] \right]^{\frac{1}{2}} \frac{g_{ant}}{g} \exp(2\mathrm{i}\phi_G) \\
& \times \frac{\delta n_e}{n_e} \hat{\mathbf{e}}^* \cdot \left(\boldsymbol{\epsilon}_{eq} - \mathbf{1} \right) \cdot \hat{\mathbf{e}} \ \exp(2\mathrm{i}s + 2\mathrm{i}\mathbf{K}_w \cdot \mathbf{w} + \mathrm{i}\mathbf{w} \cdot \boldsymbol{\Psi}_w \cdot \mathbf{w}) \ \mathrm{d}V.
\end{aligned}
\tag{100}
$$

This is the form of the backscattered amplitude that we subsequently use.

4. Assumptions about turbulent fluctuations

We see that we need to evaluate the three spatial integrals in equation (100) to determine the backscattered signal. In order to do this, we need to make some assumptions about the nature of the turbulent fluctuations δn_e.

In this work, we take the plasma to be in steady state, such that the equilibrium electron density n_e has no time dependence, whereas we assume that the turbulent fluctuations δn_e can indeed have a fast time dependence t in addition to a spatial dependence. This time-dependence will be important in Section 7.1. For now, we will concentrate on the spatial properties δn_e.

We consider a tubular region of space around the Gaussian beam as it propagates through the plasma. This region of space is elongated along the ray, and across the ray it is several times the width of the Gaussian beam, such that the beam's electric field is effectively zero on the boundary of this region. We Fourier analyse δn_e in this volume. We use the usual assumptions for turbulent fluctuations [28, 29], considering electron density fluctuations δn_e with very large gradients across the magnetic field and small gradients along it. Hence, we define coordinates aligned with the magnetic field. We use $u_\parallel$, the arc length along magnetic field lines, and two variables u_1 and u_2 that both satisfy

$$\hat{\mathbf{b}}(\mathbf{q}(\tau) + \mathbf{w}) \cdot \nabla u_i = 0. \tag{101}$$

With these variables, we get

$$\delta n_e(\mathbf{r}, t) = \int \delta\tilde{n}_e(k_{\perp,1}, k_{\perp,2}, u_\parallel, \omega) \exp\left(\mathrm{i}k_{\perp,1}u_1 + \mathrm{i}k_{\perp,2}u_2 - \mathrm{i}\omega t\right) \mathrm{d}k_{\perp,1} \; \mathrm{d}k_{\perp,2} \; \mathrm{d}\omega, \tag{102}$$

where ω has contributions from both the angular frequency of the turbulence in the plasma's frame and the Doppler shift due to the moving plasma, and

$$k_{\perp,\alpha} \sim \frac{1}{\lambda} \gg k_\parallel \sim \frac{1}{L} \sim \frac{\partial}{\partial u_\parallel} \tag{103}$$

are the components of the turbulence wavevector perpendicular to the magnetic field. We define u_1 and u_2 such that their gradients are perpendicular to each other at $\mathbf{w} = 0$ (on the central ray). They are only perpendicular to each other along the central ray, and not when we move away from it; this is a consequence of magnetic shear. Any vector perpendicular to the magnetic field is resolved into two directions: $\hat{\mathbf{u}}_1 = \nabla u_1(\mathbf{w} = \mathbf{0})$ and $\hat{\mathbf{u}}_2 = \nabla u_2(\mathbf{w} = \mathbf{0})$. The subscripts $_1$ and $_2$ indicate projection on these directions, respectively. We choose $\hat{\mathbf{u}}_1$ and $\hat{\mathbf{u}}_2$ as follows: $\hat{\mathbf{u}}_1$ is in the plane of $\hat{\mathbf{g}}$ and $\hat{\mathbf{b}}$, while $\hat{\mathbf{u}}_2$ is perpendicular to $\hat{\mathbf{g}}$, and both of them are perpendicular to $\hat{\mathbf{b}}$,
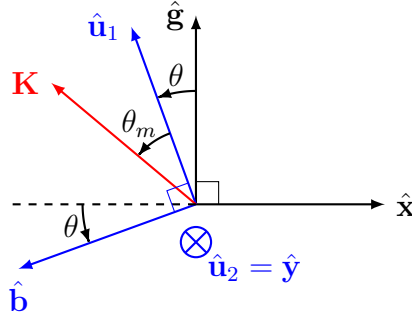
$$\hat{\mathbf{u}}_1 = \frac{(\hat{\mathbf{b}} \times \hat{\mathbf{g}}) \times \hat{\mathbf{b}}}{|(\hat{\mathbf{b}} \times \hat{\mathbf{g}}) \times \hat{\mathbf{b}}|}, \tag{104}$$

and

$$\hat{\mathbf{u}}_2 = \frac{\hat{\mathbf{b}} \times \hat{\mathbf{g}}}{|\hat{\mathbf{b}} \times \hat{\mathbf{g}}|}. \tag{105}$$

Here we take $\hat{\mathbf{b}}$ to be a shorthand for $\hat{\mathbf{b}}(\mathbf{q}(\tau)) = \hat{\mathbf{b}}(\tau)$. That is, $\hat{\mathbf{b}}$ is the unit vector of the magnetic field on the central ray. Note that if $\hat{\mathbf{g}}$ and $\hat{\mathbf{b}}$ are perpendicular to each other (that is, if there is no mismatch, as we later show), $\hat{\mathbf{u}}_1 = \hat{\mathbf{g}}$ (Figure 6). Note that these $\hat{\mathbf{u}}_1$ and $\hat{\mathbf{u}}_2$ are the same as those used in Section 2.2, as we will prove in equation (133). We align the basis for $\mathbf{w}$, see equation (8), with the basis for $\mathbf{k}_\perp$. We choose $\hat{\mathbf{y}} = \hat{\mathbf{u}}_2$ and denote projection in that direction with the subscript $_y$. The other basis vector for $\mathbf{w}$, which is perpendicular to both $\hat{\mathbf{g}}$ and $\hat{\mathbf{y}}$, will be

$$\hat{\mathbf{x}} = \frac{\hat{\mathbf{y}} \times \hat{\mathbf{g}}}{|\hat{\mathbf{y}} \times \hat{\mathbf{g}}|} = \frac{\hat{\mathbf{u}}_2 \times \hat{\mathbf{g}}}{|\hat{\mathbf{u}}_2 \times \hat{\mathbf{g}}|}. \tag{106}$$

Figure 6: Bases for $\mathbf{k}_\perp$ and $\mathbf{w}$, with $\theta > 0$ and $\theta_m > 0$.

Based on the bases for $\mathbf{k}_\perp$ and $\mathbf{w}$, we define the angle θ such that

$$\cos \theta = \hat{\mathbf{g}} \cdot \hat{\mathbf{u}}_1, \tag{107}$$

and

$$\hat{\mathbf{x}} \cdot \hat{\mathbf{u}}_1 = -\sin \theta. \tag{108}$$

This angle θ is not the mismatch angle, but is of the same order as the mismatch angle, as we will later prove. The mismatch angle is

$$\sin \theta_m = \hat{\mathbf{K}} \cdot \hat{\mathbf{b}}. \tag{109}$$

Using the definitions of $\hat{\mathbf{u}}_1 = \nabla u_1(\mathbf{w} = \mathbf{0})$ and $\hat{\mathbf{u}}_2 = \nabla u_2(\mathbf{w} = \mathbf{0})$ above, we derive the coordinates u_1 and u_2 in Appendix D. We summarise the results here. They are

$$
\begin{aligned}
u_1 =& \int_0^\tau g(\tau') \cos \theta(\tau') \, \mathrm{d}\tau - w_x \sin \theta \\
&+ \frac{w_x^2}{2} \left(\frac{\sin \theta}{g} \frac{\mathrm{d}\theta}{\mathrm{d}\tau} - \boldsymbol{\kappa} \cdot \hat{\mathbf{x}} \sin \theta + \hat{\mathbf{x}} \cdot \nabla \hat{\mathbf{b}} \cdot \hat{\mathbf{g}} - \hat{\mathbf{x}} \cdot \nabla \hat{\mathbf{b}} \cdot \hat{\mathbf{x}} \tan \theta \right) \\
&+ w_x w_y \left(-\boldsymbol{\kappa} \cdot \hat{\mathbf{y}} \sin \theta + \hat{\mathbf{y}} \cdot \nabla \hat{\mathbf{b}} \cdot \hat{\mathbf{g}} + \frac{\sin \theta \tan \theta}{g} \frac{\mathrm{d}\hat{\mathbf{x}}}{\mathrm{d}\tau} \cdot \hat{\mathbf{y}} - \hat{\mathbf{y}} \cdot \nabla \hat{\mathbf{b}} \cdot \hat{\mathbf{x}} \tan \theta \right),
\end{aligned} \tag{110}
$$

and

$$u_2 = w_y + \frac{w_x^2}{2} \left(\frac{\tan \theta}{g} \frac{\mathrm{d}\hat{\mathbf{x}}}{\mathrm{d}\tau} \cdot \hat{\mathbf{y}} + \frac{\hat{\mathbf{x}} \cdot \nabla \hat{\mathbf{b}} \cdot \hat{\mathbf{y}}}{\cos \theta} \right) + w_x w_y \frac{\hat{\mathbf{y}} \cdot \nabla \hat{\mathbf{b}} \cdot \hat{\mathbf{y}}}{\cos \theta}. \tag{111}$$

Here,

$$\boldsymbol{\kappa} = \frac{1}{g} \frac{\mathrm{d}\hat{\mathbf{g}}}{\mathrm{d}\tau} \tag{112}$$

is the curvature of the central ray. This ray curvature should not be confused with the wavefront curvature, $1/R_b$. Note that we have kept corrections to u_1 and u_2 to order λ. Finally, the arc length along the magnetic field is

$$u_\parallel \simeq -\int_0^\tau g(\tau') \sin \theta(\tau') \mathrm{d}\tau' - w_x \cos \theta, \tag{113}$$

where we have neglected terms that are small in W/L. Since $k_\parallel \sim 1/L$, we have $k_\parallel u_\parallel \sim 1$, and the higher order contributions to $u_\parallel$ are not required.

5. Backscattered electric field: general

We proceed to evaluate the amplitude of the backscattered electric field, A_r. Writing the volume element in equation (100) as

$$\mathrm{d}V = g \, \mathrm{d}w_x \, \mathrm{d}w_y \, \mathrm{d}\tau, \tag{114}$$

and substituting equations (102), (110), and (111) into equation (100), we get

$$
\begin{aligned}
A_r = {} & \frac{\mathrm{i}\Omega A_{ant} g_{ant} \hat{\mathbf{e}}_{ant} \cdot \hat{\mathbf{e}}_{ant}}{2\pi c} \int [\det[\mathrm{Im}(\boldsymbol{\Psi}_w)]]^{\frac{1}{2}} \exp(2\mathrm{i}\phi_G) \exp\left(-\mathrm{i}\omega t\right) \\
& \times \frac{\delta\tilde{n}_e}{n_e} \, \hat{\mathbf{e}}^* \cdot (\boldsymbol{\epsilon}_{eq} - \mathbf{1}) \cdot \hat{\mathbf{e}} \, \exp\left(2\mathrm{i}s + \mathrm{i}k_{\perp,1}\int_0^\tau g(\tau')\cos\theta(\tau')\,\mathrm{d}\tau'\right) \\
& \times \exp\left[\mathrm{i}(2\mathbf{K}_w + \mathbf{k}_{\perp,w})\cdot\mathbf{w} + \mathrm{i}\mathbf{w}\cdot\boldsymbol{M}_w\cdot\mathbf{w}\right] \, \mathrm{d}w_x \, \mathrm{d}w_y \, \mathrm{d}\tau \, \mathrm{d}k_{\perp,1} \, \mathrm{d}k_{\perp,2} \, \mathrm{d}\omega.
\end{aligned}
\tag{115}
$$

Here $\mathbf{k}_\perp = k_{\perp,1}\hat{\mathbf{u}}_1 + k_{\perp,2}\hat{\mathbf{u}}_2$, $\mathbf{k}_{\perp,w}$ is $\mathbf{k}_\perp$ projected on the plane perpendicular to the group velocity, and $\boldsymbol{M}_w$ is the symmetric modified $\boldsymbol{\Psi}_w$ matrix, given by

$$\boldsymbol{M}_w = \begin{pmatrix} M_{xx} & M_{xy} & 0 \\ M_{xy} & M_{yy} & 0 \\ 0 & 0 & 0 \end{pmatrix}, \tag{116}$$

where

$$
\begin{aligned}
M_{xx} = {} & \Psi_{xx} + \frac{k_{\perp,1}}{2}\left(\frac{\sin\theta}{g}\frac{\mathrm{d}\theta}{\mathrm{d}\tau} - \boldsymbol{\kappa}\cdot\hat{\mathbf{x}}\sin\theta + \hat{\mathbf{x}}\cdot\nabla\hat{\mathbf{b}}\cdot\hat{\mathbf{g}} - \hat{\mathbf{x}}\cdot\nabla\hat{\mathbf{b}}\cdot\hat{\mathbf{x}}\tan\theta\right) \\
& + \frac{k_{\perp,2}}{2}\left(\frac{\tan\theta}{g}\frac{\mathrm{d}\hat{\mathbf{x}}}{\mathrm{d}\tau}\cdot\hat{\mathbf{y}} + \frac{\hat{\mathbf{x}}\cdot\nabla\hat{\mathbf{b}}\cdot\hat{\mathbf{y}}}{\cos\theta}\right),
\end{aligned}
\tag{117}
$$

$$
\begin{aligned}
M_{xy} = {} & \Psi_{xy} + \frac{k_{\perp,1}}{2}\left(-\boldsymbol{\kappa}\cdot\hat{\mathbf{y}}\sin\theta + \hat{\mathbf{y}}\cdot\nabla\hat{\mathbf{b}}\cdot\hat{\mathbf{g}} + \frac{\sin\theta\tan\theta}{g}\frac{\mathrm{d}\hat{\mathbf{x}}}{\mathrm{d}\tau}\cdot\hat{\mathbf{y}} - \hat{\mathbf{y}}\cdot\nabla\hat{\mathbf{b}}\cdot\hat{\mathbf{x}}\tan\theta\right) \\
& + \frac{k_{\perp,2}}{2}\frac{\hat{\mathbf{y}}\cdot\nabla\hat{\mathbf{b}}\cdot\hat{\mathbf{y}}}{\cos\theta},
\end{aligned}
\tag{118}
$$

and

$$M_{yy} = \Psi_{yy}. \tag{119}$$

It is worth noting a few points about this modified matrix. First, the modifications to $\boldsymbol{\Psi}_w$ are only to its real part, that is, the part associated with curvature (as opposed to width). Secondly, that these modifications depend directly on the curvature of the magnetic field and the magnetic shear; the curvature of the cut-off surface does not explicitly enter the corrections. As we will see in Section 9, this affects the wavenumber resolution, and our model gives a different result from widely-cited earlier work [2, 25]. In Scotty, we calculate the gradients of $\hat{\mathbf{b}}$ in cylindrical coordinates,

$$
\begin{aligned}
\nabla\hat{\mathbf{b}} = {} & \frac{\partial b_R}{\partial R}\hat{\mathbf{R}}\hat{\mathbf{R}} + \frac{\partial b_R}{\partial Z}\hat{\mathbf{Z}}\hat{\mathbf{R}} + b_R\frac{\hat{\boldsymbol{\zeta}}\hat{\boldsymbol{\zeta}}}{R} + \frac{\partial b_Z}{\partial R}\hat{\mathbf{R}}\hat{\mathbf{Z}} + \frac{\partial b_Z}{\partial Z}\hat{\mathbf{Z}}\hat{\mathbf{Z}} \\
& + \frac{\partial b_\zeta}{\partial R}\hat{\mathbf{R}}\hat{\boldsymbol{\zeta}} + \frac{\partial b_\zeta}{\partial Z}\hat{\mathbf{Z}}\hat{\boldsymbol{\zeta}} - b_\zeta\frac{\hat{\boldsymbol{\zeta}}\hat{\mathbf{R}}}{R}.
\end{aligned}
\tag{120}
$$

To get this result, one should remember that the $\hat{\mathbf{R}}$ and $\hat{\boldsymbol{\zeta}}$ basis vectors depend on position. That is, we have used

$$\nabla\hat{\mathbf{R}} = \frac{\hat{\boldsymbol{\zeta}}\hat{\boldsymbol{\zeta}}}{R}, \tag{121}$$

and

$$\nabla\hat{\boldsymbol{\zeta}} = -\frac{\hat{\boldsymbol{\zeta}}\hat{\mathbf{R}}}{R}. \tag{122}$$

What the DBS community actually uses is not $A_r(t)$ directly, but its Fourier transform $\tilde{A}_r(\omega) = (2\pi)^{-1} \int A_r(t) \exp(\mathrm{i}\omega t) \, \mathrm{d}t$, which is

$$\begin{aligned}
\tilde{A}_r(\omega) = {} & \frac{\mathrm{i}\Omega A_{ant}g_{ant}\hat{\mathbf{e}}_{ant} \cdot \hat{\mathbf{e}}_{ant}}{2\pi c} \int [\det[\mathrm{Im}(\boldsymbol{\Psi}_w)]]^{\frac{1}{2}} \exp(2\mathrm{i}\phi_G) \\
& \times \frac{\delta\tilde{n}_e}{n_e} \, \hat{\mathbf{e}}^* \cdot (\boldsymbol{\epsilon}_{eq} - \mathbf{1}) \cdot \hat{\mathbf{e}} \, \exp\left(2\mathrm{i}s + \mathrm{i}k_{\perp,1} \int_0^\tau g(\tau') \cos\theta(\tau') \, \mathrm{d}\tau'\right) \\
& \times \exp\left[\mathrm{i}(2\mathbf{K}_w + \mathbf{k}_{\perp,w}) \cdot \mathbf{w} + \mathrm{i}\mathbf{w} \cdot \boldsymbol{M}_w \cdot \mathbf{w}\right] \, \mathrm{d}w_x \, \mathrm{d}w_y \, \mathrm{d}\tau \, \mathrm{d}k_{\perp,1} \, \mathrm{d}k_{\perp,2}.
\end{aligned} \tag{123}$$

The task ahead of us is to solve the integrals in equation (123). We begin by evaluating the Gaussian integrals in $\mathbf{w}$ (Section 5.1). When calculating Gaussian integrals with complex coefficients, we need to be careful to choose the correct signs of the roots, in accordance with standard contour integration techniques. To solve the integral in τ, we have to make some assumptions about θ, which we do in Section 5.2. Depending on the assumptions made, we can solve this integral with the *small mismatch angle* (Section 6) or *large mismatch angle* (Section 11) orderings. Moving forward, the form of the backscattered electric field that we will use for the backscattered power will be that of the *small mismatch angle* ordering. We later show in Section 11 that in the appropriate limit, the *small mismatch angle* and *large mismatch angle* orderings give the same result. This enables us to use the *small mismatch angle* formulation even in cases which are moderately in the *large mismatch angle* regime.

5.1. Gaussian integrals in w_x and w_y

To solve the spatial integrals perpendicular to the beam, we first define the inverse of $\boldsymbol{M}_w$ as

$$\boldsymbol{M}_w^{-1} = \begin{pmatrix} M_{xx}^{-1} & M_{xy}^{-1} & 0 \\ M_{yx}^{-1} & M_{yy}^{-1} & 0 \\ 0 & 0 & 0 \end{pmatrix} = \begin{pmatrix} \begin{pmatrix} M_{xx} & M_{xy} \\ M_{yx} & M_{yy} \end{pmatrix}^{-1} & \begin{array}{c} 0 \\ 0 \end{array} \\ \begin{array}{cc} 0 & 0 \end{array} & 0 \end{pmatrix}, \tag{124}$$

which one may recognise as the Moore-Penrose inverse. It is important to bear in mind that M_{ij}^{-1} is the ij component of $\boldsymbol{M}_w^{-1}$, and not $1/M_{ij}$. We then note that

$$\begin{aligned}
(2\mathbf{K}_w &+ \mathbf{k}_{\perp,w}) \cdot \mathbf{w} + \mathbf{w} \cdot \boldsymbol{M}_w \cdot \mathbf{w} \\
&= \left[\mathbf{w} + \frac{1}{2}(2\mathbf{K}_w + \mathbf{k}_{\perp,w}) \cdot \boldsymbol{M}_w^{-1}\right] \cdot \boldsymbol{M}_w \cdot \left[\mathbf{w} + \frac{1}{2}\boldsymbol{M}_w^{-1} \cdot (2\mathbf{K}_w + \mathbf{k}_{\perp,w})\right] \\
&\quad - \frac{1}{4}(2\mathbf{K}_w + \mathbf{k}_{\perp,w}) \cdot \boldsymbol{M}_w^{-1} \cdot (2\mathbf{K}_w + \mathbf{k}_{\perp,w}).
\end{aligned} \tag{125}$$

We substitute this expression into equation (115). Note that the integral over w_y in equation (123) is a Gaussian integral. The integral over w_x in equation (123) is not strictly a Gaussian integral because of the dependence of $u_\parallel$ on w_x; this dependence is negligible because the turbulent properties change slowly along a field line, allowing us to use the approximate expression

$$\delta\tilde{n}_e\left(k_{\perp,1}, k_{\perp,2}, u_\parallel, \omega\right) \simeq \delta\tilde{n}_e\left(k_{\perp,1}, k_{\perp,2}, -\int_0^\tau g(\tau')\sin\theta(\tau')\,\mathrm{d}\tau', \omega\right), \ (126)$$

to treat this integral as Gaussian as well. Thus, we have a 2D complex Gaussian integral; one should be careful when choosing the signs of the roots, as dictated by standard contour integration techniques. Hence, equation (123) becomes

$$\tilde{A}_r = -\frac{\Omega A_{ant} g_{ant} \hat{\mathbf{e}}_{ant} \cdot \hat{\mathbf{e}}_{ant}}{2c} \int \left[\frac{\det\left[\mathrm{Im}\left(\boldsymbol{\Psi}_w\right)\right]}{\det\left(\boldsymbol{M}_w\right)}\right]^{\frac{1}{2}} \exp(2\mathrm{i}\phi_G)$$

$$\times \frac{\delta\tilde{n}_e}{n_e}\ \hat{\mathbf{e}}^* \cdot (\boldsymbol{\epsilon}_{eq} - \mathbf{1}) \cdot \hat{\mathbf{e}}\ \exp\left(2\mathrm{i}s + \mathrm{i}k_{\perp,1}\int_0^\tau g(\tau')\cos\theta(\tau')\,\mathrm{d}\tau'\right) \quad (127)$$

$$\times \exp\left[-\frac{\mathrm{i}}{4}(2\mathbf{K}_w + \mathbf{k}_{\perp,w}) \cdot \boldsymbol{M}_w^{-1} \cdot (2\mathbf{K}_w + \mathbf{k}_{\perp,w})\right]\ \mathrm{d}\tau\ \mathrm{d}k_{\perp,1}\ \mathrm{d}k_{\perp,2}.$$

We note that the phase of $\sqrt{\det\left(\boldsymbol{M}_w\right)}$ is chosen from

$$\sqrt{\det\left(\boldsymbol{M}_w\right)} = \sqrt{M_{xx}}\sqrt{\frac{\det\left(\boldsymbol{M}_w\right)}{M_{xx}}}, \quad (128)$$

and the fact that these square roots must have

$$\mathrm{Im}\left(\sqrt{M_{xx}}\right) > 0, \quad (129)$$

and

$$\mathrm{Im}\left[\sqrt{\frac{\det\left(\boldsymbol{M}_w\right)}{M_{xx}}}\right] > 0. \quad (130)$$

A convenient way to remember these rules is to consider a purely imaginary $\boldsymbol{M}_w$, in which case this result is the most intuitive and sensible one.

To simplify equation (127), we project $\mathbf{K}_w$ onto $\hat{\mathbf{x}}$ and $\hat{\mathbf{y}}$. Note that the dispersion relation for cold plasma depends on $\mathbf{K}$ only via K^2 and $(\mathbf{K}\cdot\hat{\mathbf{b}})^2$,

$$H(\mathbf{K}, \mathbf{q}) = H(K^2, (\mathbf{K}\cdot\hat{\mathbf{b}})^2, \mathbf{q}). \quad (131)$$

Thus, we find that

$$\mathbf{g} = \nabla_K H = 2\frac{\partial H}{\partial K^2}\mathbf{K} + 2K\sin\theta_m\frac{\partial H}{\partial(\mathbf{K}\cdot\hat{\mathbf{b}})^2}\hat{\mathbf{b}}. \quad (132)$$

and as a consequence

$$K_y = 0. \quad (133)$$

That is, the beam wavevector $\mathbf{K}$ is always in the plane defined by $\hat{\mathbf{b}}$ and $\hat{\mathbf{g}}$. Using these insights, we remark that there is an exponential decay of the signal with $k_{\perp,2}$ because of the piece

$$
\begin{aligned}
&\exp\left[-\frac{\mathrm{i}}{4}(2\mathbf{K}_w + \mathbf{k}_{\perp,w}) \cdot \boldsymbol{M}_w^{-1} \cdot (2\mathbf{K}_w + \mathbf{k}_{\perp,w})\right] \\
&= \exp\left[-\frac{\mathrm{i}}{4}\left((2K_x - k_{\perp,1}\sin\theta)^2 M_{xx}^{-1} + 2k_{\perp,2}(2K_x - k_{\perp,1}\sin\theta)M_{xy}^{-1} + k_{\perp,2}^2 M_{yy}^{-1}\right)\right].
\end{aligned}
\tag{134}
$$

Hence, $k_{\perp,2}$ cannot be of order $1/\lambda$ because otherwise the argument of the exponential will be large and there will be no signal. Instead, by requiring that this argument can at most be of order unity, we find that

$$
k_{\perp,2} \sim \frac{1}{W}.
\tag{135}
$$

5.2. Ordering θ_m

We consider two orderings: *small mismatch angle* and *large mismatch angle*. These are simply names for two different orderings typical of, but not exclusive to, conventional and spherical tokamaks, respectively. Moreover, these orderings are not only applicable to tokamaks. As long as the particular ordering holds, the results will be applicable. In particular, they are applicable to stellarators.

In the *small mismatch angle* ordering, we take the mismatch angle to be small for the entire length of the beam path,

$$
\theta_m \sim \frac{\lambda}{W}.
\tag{136}
$$

In this situation, the backscattered signal is given by the Bragg condition, which we discuss in more detail in Section 6.

In the *large mismatch angle* ordering, we take the mismatch angle to be of order unity $\theta_m \sim 1$. In general, this requires more work and is beyond the scope of this paper. However, in the special scenario where there is no mismatch ($\theta_m = 0$) on at least one point along the beam path, the backscattered signal is dominated by this point. We derive the backscattered signal for this particular ordering in Section 11. In the right limits, we show that the *large mismatch angle* and *small mismatch angle* orderings coincide, see Section 11.

6. Backscattered electric field: small mismatch angle ordering

In this section, we solve the integral in τ for the *small mismatch angle* ordering, while the *large mismatch angle* ordering will be handled in Section 11. We begin by exploring in detail the orderings involved in the former ordering. Once we do this, we then proceed to evaluate the integral in τ via the method of stationary phase.

6.1. Ordering

We contract equation (132) with $\hat{\mathbf{b}}$, giving us

$$-g\sin\theta = 2K\left(\frac{\partial H}{\partial K^2} + \frac{\partial H}{\partial(\mathbf{K}\cdot\hat{\mathbf{b}})^2}\right)\sin\theta_m. \tag{137}$$

When $\theta_m \sim \lambda/W$, equation (132) gives us $g \simeq 2K\,\partial H/\partial K^2$ to leading order. Hence we find that

$$\sin\theta = -\left[1 + \frac{\partial H}{\partial(\mathbf{K}\cdot\hat{\mathbf{b}})^2}\left(\frac{\partial H}{\partial K^2}\right)^{-1}\right]\sin\theta_m. \tag{138}$$

The finer details of the relationship between θ and θ_m are discussed in Appendix E. However, to proceed, all we need is to note that since

$$\frac{\partial H}{\partial(\mathbf{K}\cdot\hat{\mathbf{b}})^2} \sim \frac{\partial H}{\partial K^2}, \tag{139}$$

we get

$$\theta \sim \theta_m \sim \frac{\lambda}{W}. \tag{140}$$

Consequently, we have

$$K_x = -K\sin(\theta_m + \theta) \simeq -K(\theta_m + \theta) \sim \frac{1}{W}. \tag{141}$$

Hence, K_x/K is small in mismatch angle, whereas

$$K_g = K\cos(\theta + \theta_m) \simeq K. \tag{142}$$

From equations (133) and (141), we find that $K_w/K = K_x/K \sim \theta_m$. At this point, we see that our ordering $\theta_m \sim \lambda/W$ is necessary for the mismatch angle to be small enough to allow for a backscattered signal to be detected. Indeed, using equations (140) and (141), the M_{xx}^{-1} and M_{xy}^{-1} terms in the exponential of equation (134) are of order unity.

In a conventional tokamak, most of the magnetic field is in the toroidal direction $\hat{\mathbf{b}} \simeq \hat{\boldsymbol{\zeta}}$. Hence, to have $\theta \sim \lambda/W$, we require

$$\hat{\mathbf{g}}\cdot\hat{\boldsymbol{\zeta}} \sim \frac{\lambda}{W}. \tag{143}$$

Note that this is a maximal ordering. The consequence of this is that the group velocity of the probe beam can have a small toroidal component and the orderings will still hold, but everything still works perfectly fine if the group velocity is entirely in the poloidal plane. If this were the case, then the mismatch angle is simply the ratio of the poloidal magnetic field to the toroidal magnetic field, leading us to the conclusion that

$$\frac{B_p}{B} \sim \frac{\lambda}{W}. \tag{144}$$

When the mismatch angle is exactly zero, $\hat{\mathbf{e}}$ can be calculated exactly. In the basis of Section 2.2, the polarisations of the O-mode and X mode are

$$\hat{\mathbf{e}}_O \propto \begin{pmatrix} 0 \\ 0 \\ 1 \end{pmatrix}, \tag{145}$$
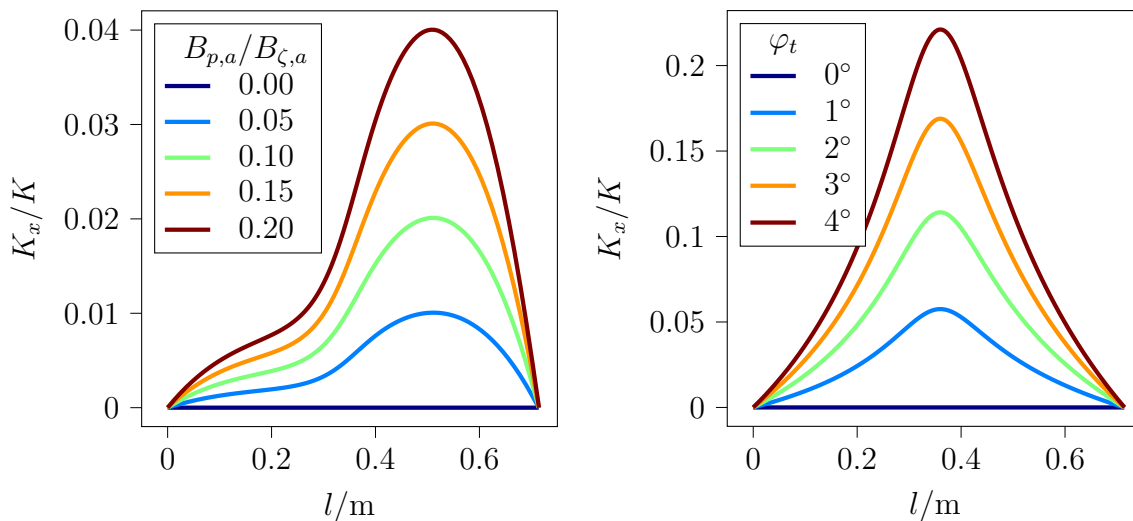
Figure 7: Here l is the arc-length along the central ray, measured from the point of entering the plasma. For a beam in the poloidal plane, increasing the ratio of poloidal field to toroidal field $B_{p,a}/B_{\zeta,a}$ increases the mismatch angle, which increases K_x/K (left). Increasing the toroidal launch angle also increases the mismatch angle, which increases K_x/K (right). We used circular flux surfaces, as described in Section 2.4.

and

$$\hat{\mathbf{e}}_x \propto \begin{pmatrix} i\epsilon_{12} \\ \epsilon_{11} \\ 0 \end{pmatrix}. \tag{146}$$

Since we assume the antenna surface to be in vacuum, we take the limit $n_e \to 0$ to find the polarisation at the antenna. The polarisation is linear and hence $|\hat{\mathbf{e}}_{ant} \cdot \hat{\mathbf{e}}_{ant}| = 1$. Without loss of generality, we take $\hat{\mathbf{e}}_{ant}$ to be purely real, and in this case, $\hat{\mathbf{e}}_{ant} \cdot \hat{\mathbf{e}}_{ant} = 1$. If, for purely perpendicular propagation, $\hat{\mathbf{e}}_{ant} \cdot \hat{\mathbf{e}}_{ant} = 1$, then for $\theta \sim \theta_m \ll 1$, it will be close to one.

In order to help develop better intuition of equation (141) and the various orderings, we launch various probe beams into high-aspect-ratio circular-flux-surface analytic equilibria with no Shafranov shift, described in Section 2.4. We fix the launch angles, and vary $B_{p,max}/B_{\zeta,max}$, thereby scaling $B_p/B_\zeta \sim B_p/B \sim \theta_m$ everywhere. We see from Figure 7 (left) that the magnitude of K_x scales accordingly, as expected. We increase the toroidal launch angle for a plasma with $B_p = 0$, starting from a launch angle of 0, which corresponds to the beam being entirely in the poloidal plane. This also has the effect of increasing the mismatch angle, and we can see in Figure 7 (right) that K_x also increases.

6.2. Stationary phase integral in τ

We now proceed to evaluate the integral in τ in equation (127), exploiting the orderings above. Noticing that the function $\exp\left[2is + ik_{\perp,1} \int_0^\tau g(\tau') \cos\theta(\tau')\,d\tau'\right]$ oscillates quickly

in τ since $2s + k_{\perp,1} \int_0^\tau g(\tau') \cos\theta(\tau') \, \mathrm{d}\tau' \sim L/\lambda \gg 1$, we use the method of stationary phase to evaluate the τ integral, an approach to DBS that is well-established [24]. The method works as follows. Since the exponential fluctuates quickly, the positive fluctuations cancel with the negative fluctuations, integrating to zero to lowest order. This does not happen where the phase is stationary, that is, when

$$\frac{\mathrm{d}}{\mathrm{d}\tau}\left[2s + k_{\perp,1}\int_0^\tau g(\tau')\cos\theta(\tau')\,\mathrm{d}\tau'\right]\Bigg|_{\tau_\mu} = 0, \tag{147}$$

where $\tau_\mu = \tau_a, \tau_b, \ldots$ are various points along the ray that satisfy this equation. Equation (147) is the Bragg condition alluded to in the introduction,

$$k_{\perp,1}\cos\theta(\tau_\mu) = -2K_g(\tau_\mu). \tag{148}$$

Neglecting terms that are small in mismatch, we get

$$k_{\perp,1} \simeq -2K(\tau_\mu), \tag{149}$$

which is how the Bragg condition is typically presented in the literature: at every point along the ray, there is a specific $k_{\perp,1}$ that is responsible for backscattering, and its value is determined solely by the wavenumber at that point. We consider the case where the density profile is monotonic. In such a situation, K decreases as we get close to the cut-off, and increases as we go further from it. Hence, for any given $k_{\perp,1}$, there are three possible scenarios, as shown in Figure 8. First, that $k_{\perp,1}$ is either too small or too large, such that at no point of the ray's trajectory is it responsible for backscattering. Second, that it backscatters the beam exactly once, at an extremum value of K along the path. Third, that the same $k_{\perp,1}$ is responsible for backscattering at two points along the path, $\tau_\mu = \tau_a$ and $\tau_\mu = \tau_b$; consequently, we have to add contributions from both these locations when taking the integral in τ. This can be extended to more complicated cases where the density profile is non-monotonic.

Since the dominant contributions to the integral are due to small intervals centred around $\tau_\mu = \tau_a, \tau_b, \ldots$, we Taylor expand the phase $2\mathrm{i}s + \mathrm{i}k_{\perp,1}\int_0^\tau g(\tau')\,\mathrm{d}\tau'$ around $\tau_a, \tau_b, \ldots$ to find these contributions. Usually, we will have at most two points to expand around (τ_a and τ_b), but we keep things general and sum over all of them, just in case one were to consider one of the aforementioned complicated cases. We first note that when the mismatch angle is small, $\theta_m \sim \lambda/W$, we have

$$\exp\left(\mathrm{i}k_{\perp,1}\int_0^\tau g(\tau')\cos\theta(\tau')\,\mathrm{d}\tau'\right) \simeq \exp\left(\mathrm{i}k_{\perp,1}\int_0^\tau g(\tau')\left(1-\frac{1}{2}\theta^2(\tau')\right)\mathrm{d}\tau'\right), \tag{150}$$

where we have discarded terms which are small. Hence, expanding the large phase term, we get

$$
\begin{aligned}
&\exp\left(2\mathrm{i}s + \mathrm{i}k_{\perp,1}\int_0^\tau g(\tau')\left(1-\frac{1}{2}\theta^2(\tau')\right)\mathrm{d}\tau'\right) \\
&\simeq \exp\left[2\mathrm{i}s(\tau_\mu) + \mathrm{i}k_{\perp,1}\int_0^{\tau_\mu} g(\tau')\left(1-\frac{1}{2}\theta^2(\tau')\right)\mathrm{d}\tau' + \mathrm{i}g(\tau_\mu)\frac{\mathrm{d}K}{\mathrm{d}\tau}\bigg|_{\tau_\mu}(\tau-\tau_\mu)^2\right].
\end{aligned}
\tag{151}
$$

Here the subscript $_\mu$ on functions of τ indicates these functions are evaluated at $\tau = \tau_\mu$. We have also used the Bragg condition, equation (149), to simplify some of the terms.
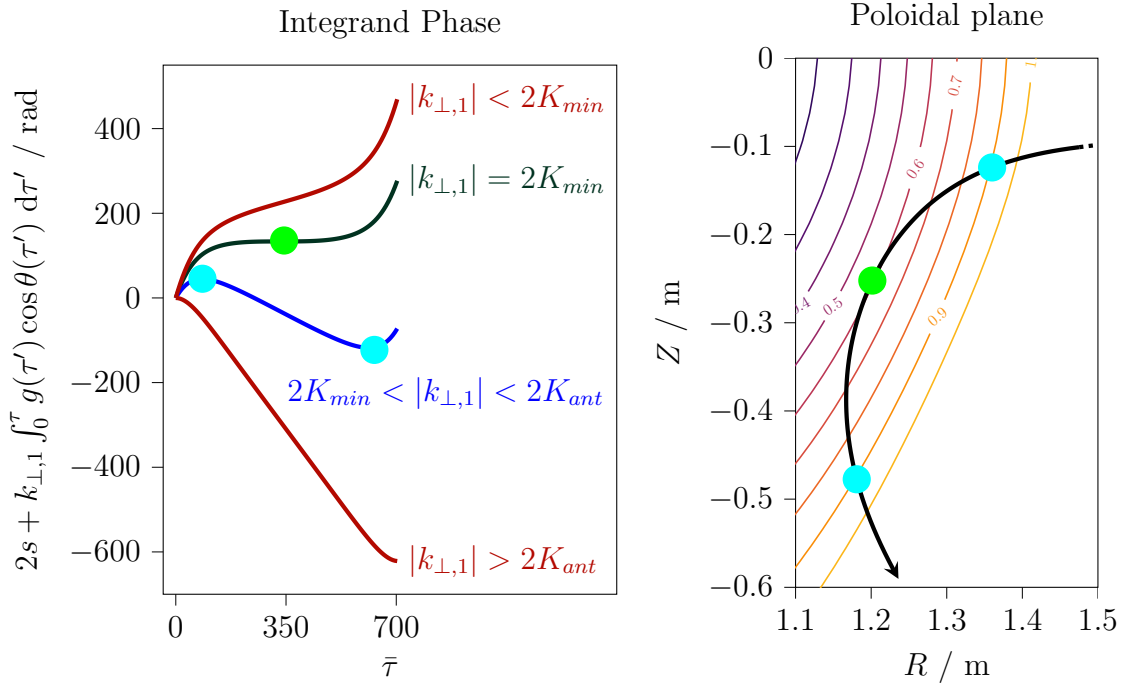
Figure 8: The beam is launched from the steering mirror, located on the midplane at $R = 2.4$m, which is out of the graph's boundaries (right). The thick black line (right) indicates the trajectory of the central ray and the arrow the direction of propagation. Here K_{min} is the minimum wavenumber along the central ray and K_{ant} is the vacuum wavenumber. Every $k_{\perp,1}$ is associated with scattering at different points of the beam path in our MAST test scenario. Every point only backscatters one particular $k_{\perp,1}$. Red lines: these values of $k_{\perp,1}$ are not responsible for backscattering along the ray (either too large or too small). Green line: the $k_{\perp,1}$ for which backscattering occurs at the extremum. Blue line: this value of $k_{\perp,1}$ backscatters from two points along the ray, which is generally the case.

Thus, the final integral is again a Gaussian integral that gives a significant contribution for sufficiently small values of $|\tau - \tau_\mu|$; hence, slowly-varying functions of τ such as $\delta\tilde{n}_e$ can be simply evaluated at $\tau_a, \tau_b, \ldots$,

$$\delta\tilde{n}_e\left(k_{\perp,1}, k_{\perp,2}, u_\parallel, \omega\right) \simeq \delta\tilde{n}_{e,\mu}\left(k_{\perp,1}, k_{\perp,2}, \omega\right)$$
$$= \delta\tilde{n}_e\left(k_{\perp,1}, k_{\perp,2}, -\int_0^{\tau_\mu} g(\tau')\sin\theta(\tau')\,\mathrm{d}\tau', \omega\right), \quad (152)$$

giving

$$
\tilde{A}_r = -\frac{\Omega A_{ant} g_{ant}}{2c} \int \sum_{\mu=a,b,\dots} \left[\frac{\det\left[\mathrm{Im}\left(\boldsymbol{\Psi}_{w,\mu} \right) \right]}{\det\left(\boldsymbol{M}_{w,\mu} \right)} \right]^{\frac{1}{2}} \left[\pi \mathrm{i} \left(g_\mu \frac{\mathrm{d}K}{\mathrm{d}\tau} \Big|_{\tau_\mu} \right)^{-1} \right]^{\frac{1}{2}}
$$

$$
\times \exp\left(2\mathrm{i}\phi_{G,\mu} \right) \, \hat{\mathbf{e}}_\mu^* \cdot \left(\boldsymbol{\epsilon}_{eq,\mu} - \mathbf{1} \right) \cdot \hat{\mathbf{e}}_\mu \frac{\delta \tilde{n}_{e,\mu}}{n_{e,\mu}}
$$

$$
\times \exp\left[-\frac{\mathrm{i}}{4} (2\mathbf{K}_{w,\mu} + \mathbf{k}_\perp) \cdot \boldsymbol{M}_{w,\mu}^{-1} \cdot (2\mathbf{K}_{w,\mu} + \mathbf{k}_\perp) \right]
$$

$$
\times \exp\left(2\mathrm{i}s_\mu + \mathrm{i}k_{\perp,1} \int_0^{\tau_\mu} g(\tau') \left(1 - \frac{\theta^2(\tau')}{2} \right) \, \mathrm{d}\tau' \right) \, \mathrm{d}k_{\perp,1} \, \mathrm{d}k_{\perp,2}.
$$

(153)

With the mismatch angle being small, $\theta_m \sim W/L$, we remark that

$$
-\frac{\mathrm{i}}{4} (2\mathbf{K}_{w,\mu} + \mathbf{k}_\perp) \cdot \boldsymbol{M}_{w,\mu}^{-1} \cdot (2\mathbf{K}_{w,\mu} + \mathbf{k}_\perp)
$$

$$
\simeq -\mathrm{i}K_\mu^2 \theta_{m,\mu}^2 M_{xx,\mu}^{-1} + \mathrm{i}k_{\perp,2} K_\mu \theta_{m,\mu} M_{xy,\mu}^{-1} - \frac{\mathrm{i}}{4} k_{\perp,2}^2 M_{yy,\mu}^{-1},
$$

(154)

and the corrections to $\boldsymbol{\Psi}_w$ are

$$
M_{xx,\mu} \simeq \Psi_{xx,\mu} - \frac{k_{\perp,1}}{2} \left(\hat{\mathbf{b}} \cdot \nabla \hat{\mathbf{b}} \cdot \hat{\mathbf{g}} \right)_\mu,
$$

(155)

and

$$
M_{xy,\mu} \simeq \Psi_{xy,\mu} + \frac{k_{\perp,1}}{2} \frac{\left[\left(\hat{\mathbf{b}} \times \hat{\mathbf{g}} \right) \cdot \nabla \hat{\mathbf{b}} \cdot \hat{\mathbf{g}} \right]_\mu}{\left| \hat{\mathbf{b}}_\mu \times \hat{\mathbf{g}}_\mu \right|}.
$$

(156)

Here we have used, $\hat{\mathbf{x}} \simeq -\hat{\mathbf{b}}$, $\hat{\mathbf{y}} = \hat{\mathbf{b}} \times \hat{\mathbf{g}}/|\hat{\mathbf{b}} \times \hat{\mathbf{g}}|$, and the result that $k_{\perp,2} \sim 1/W$, as we argued in equation (135). Hence, the $M_{xx,\mu}$ is modified by the curvature of the magnetic field $\mathbf{B}$, while $M_{xy,\mu}$ is modified by the magnetic shear.

Unfortunately, $\mathrm{d}K/\mathrm{d}\tau = 0$ at a minimum of one point along the ray, since K decreases as the beam enters the plasma and increases as it leaves. A proper treatment of this divergence requires us to consider the next order terms in the Taylor expansion of the phase $2\mathrm{i}s + \mathrm{i}k_{\perp,1} \int_0^{\tau_\mu} g(\tau') \left(1 - \theta^2(\tau')/2 \right) \, \mathrm{d}\tau'$, which we do in Appendix F. However, this is not an important issue; the divergence is integrable, as we see in Section 8.

At this point, we find ourselves in a bit of a difficulty. Consider the inverse Fourier transform of the density fluctuations

$$
\delta \tilde{n}_{e,\mu}(k_{\perp,1}, k_{\perp,2}, \omega) = \frac{1}{4\pi^2} \int \delta n_e \left(u_1, u_2, -\int_0^{\tau_\mu} g(\tau') \sin\theta(\tau') \, \mathrm{d}\tau', t \right)
$$

$$
\times \exp\left(-\mathrm{i}k_{\perp,1} u_1 - \mathrm{i}k_{\perp,2} u_2 + \mathrm{i}\omega t \right) \mathrm{d}k_{\perp,1} \, \mathrm{d}k_{\perp,2} \, \mathrm{d}\omega.
$$

(157)

We see from equations (110) and (111) that $u_1 \sim L$ and $u_2 \sim W$. Consequently, inverse scales as small as $1/L$ for $k_{\perp,1}$ and $1/W$ for $k_{\perp,2}$ are large enough to change $\delta \tilde{n}_{e,\mu}$ by order unity. This is in addition to δn_e changing on the very small scale of λ. Moreover, in equation (153), there is a large phase term $k_{\perp,1} \int_0^{\tau_\mu} g(\tau') \mathrm{d}\tau' \sim k_{\perp,1} L \sim L/\lambda \gg 1$. These two facts mean that we have order unity change even when $k_{\perp,1}$ changes by as little $1/L$ or when $k_{\perp,2}$ changes by $1/W$. Consequently, one would have to consider very

small inverse-length scales $1/L$ which is not only undesirable from a physical point of view, but also prevents us from evaluating either of the remaining integrals. We can get around this by working with the time-averaged backscattered power instead. Using power avoids the need to deal with the phase, and time averaging leads to separation of scales in $\delta\tilde{n}_{e,\mu}$, thereby eliminating the small inverse-length scales.

7. Backscattered power

For the reasons discussed at the end of Section 6.2, it is difficult to evaluate the $k_{\perp,1}$ and $k_{\perp,2}$ integrals when working with the backscattered amplitude. In order to make further analytical progress, we have to eschew the phase of $\tilde{A}_r$, and work with the time-averaged backscattered power instead. We introduce the correlation function (Section 7.1), and proceed to solve the Gaussian integral in $k_{\perp,2}$ (Section 7.2). Unfortunately, the final integral in $k_{\perp,1}$ cannot be solved analytically without making assumptions about the turbulence spectrum. This issue, along with a numerical solution to the $k_{\perp,1}$ integral, is discussed in Section 7.3.

7.1. Correlation function

We consider the correlation function for two density fluctuations, at $\mathbf{r}, t$ and $\mathbf{r}+\Delta\mathbf{r}, t+\Delta t$,

$$C(\mathbf{r}, t, \Delta\mathbf{r}, \Delta t) = \frac{\langle \delta n_e(\mathbf{r}, t)\delta n_e(\mathbf{r}+\Delta\mathbf{r}, t+\Delta t)\rangle_t}{\langle \delta n_e^2(\mathbf{r}, t)\rangle_t}. \tag{158}$$

The vectors $\mathbf{r}$ and $\Delta\mathbf{r}$ have different scales after time averaging, and this will be important later. Using equation (102), we express the density fluctuations in terms of their Fourier transforms

$$\frac{\langle \delta n_e(\mathbf{r}, t)\delta n_e(\mathbf{r}+\Delta\mathbf{r}, t+\Delta t)\rangle_t}{\langle \delta n_e^2(\mathbf{r}, t)\rangle_t}$$

$$= \langle \delta n_e^2(\mathbf{r}, t)\rangle_t^{-1} \int \delta\tilde{n}_e\left(k_{\perp,1}, k_{\perp,2}, u_\| + \Delta u_\|, \omega\right) \delta\tilde{n}_e^*\left(k'_{\perp,1}, k'_{\perp,2}, u_\|, \omega'\right) \tag{159}$$

$$\times \exp\left[\mathrm{i}(k_{\perp,1} - k'_{\perp,1})u_1 + \mathrm{i}(k_{\perp,2} - k'_{\perp,2})u_2\right] \langle\exp\left[-\mathrm{i}(\omega - \omega')t\right]\rangle_t$$

$$\times \exp\left(\mathrm{i}k_{\perp,1}\Delta u_1 + \mathrm{i}k_{\perp,2}\Delta u_2 - \mathrm{i}\omega\Delta t\right) \, \mathrm{d}k_{\perp,1} \, \mathrm{d}k_{\perp,2} \, \mathrm{d}\omega \, \mathrm{d}k'_{\perp,1} \, \mathrm{d}k'_{\perp,2} \, \mathrm{d}\omega'.$$

Since we assumed our system was in steady state, we can perform the time average $<>_t$ over a sufficiently large time interval

$$T \gg \frac{1}{\omega}, \tag{160}$$

such that we get a Dirac delta function as follows

$$\int_{-\infty}^{\infty} \exp\left[-\mathrm{i}(\omega - \omega')t\right] \, \mathrm{d}t = 2\pi\delta\left(\omega - \omega'\right). \tag{161}$$

However, this is not true of $k_{\perp,i} - k'_{\perp,i}$, since there is a characteristic long length scale L. After time averaging, we assume separation of scales for $\mathbf{r}$ and $\Delta\mathbf{r}$, which means we have to order

$$k_{\perp,1} - k'_{\perp,1} \sim k_{\perp,2} - k'_{\perp,2} \sim \frac{1}{L}, \tag{162}$$

but

$$k_{\perp,1} \sim k_{\perp,2} \sim \frac{1}{\lambda}. \tag{163}$$

Note the apparent contradiction with equation (135): the Fourier transform of the turbulent fluctuations $\delta\tilde{n}_e$ has $k_{\perp,2} \sim 1/\lambda$, but backscattering requires $k_{\perp,2}$ to be as small as $1/W$ per equation (135). We will see shortly that this implies that we eventually should take $k_{\perp,2} = 0$. For now, however, we get

$$\frac{\langle \delta n_e(\mathbf{r}, t) \delta n_e(\mathbf{r} + \Delta\mathbf{r}, t + \Delta t) \rangle_t}{\langle \delta n_e^2(\mathbf{r}, t) \rangle_t}$$

$$= \langle \delta n_e^2(\mathbf{r}, t) \rangle_t^{-1} \int \delta\tilde{n}_e \left(k_{\perp,1}, k_{\perp,2}, u_\| + \Delta u_\|, \omega \right) \delta\tilde{n}_e^* \left(k_{\perp,1}', k_{\perp,2}', u_\|, \omega \right) \tag{164}$$

$$\times \exp\left[i(k_{\perp,1} - k_{\perp,1}')u_1 + i(k_{\perp,2} - k_{\perp,2}')u_2 \right] \, dk_{\perp,1} \, dk_{\perp,2}$$

$$\times \exp\left(ik_{\perp,1}\Delta u_1 + ik_{\perp,2}\Delta u_2 - i\omega\Delta t \right) \, d\omega \, dk_{\perp,1}' \, dk_{\perp,2}',$$

We compare this to the Fourier transform of the correlation function with respect to $\Delta\mathbf{r}$ and Δt, which satisfies

$$C(\mathbf{r}, t, \Delta\mathbf{r}, \Delta t) = \int \widetilde{C}(\mathbf{r}, t, k_{\perp,1}, k_{\perp,2}, \Delta u_\|, \omega)$$

$$\times \exp\left(ik_{\perp,1}\Delta u_1 + ik_{\perp,2}\Delta u_2 - i\omega\Delta t \right) \, dk_{\perp,1} \, dk_{\perp,2} \, d\omega. \tag{165}$$

Hence, we find that

$$\widetilde{C}(\mathbf{r}, t, k_{\perp,1}, k_{\perp,2}, \Delta u_\|, \omega)$$

$$= \langle \delta n_e^2(\mathbf{r}, t) \rangle_t^{-1} \int \delta\tilde{n}_e \left(k_{\perp,1}, k_{\perp,2}, u_\| + \Delta u_\|, \omega \right) \delta\tilde{n}_e^* \left(k_{\perp,1}', k_{\perp,2}', u_\|, \omega \right) \tag{166}$$

$$\times \exp\left[i(k_{\perp,1} - k_{\perp,1}')u_1 + i(k_{\perp,2} - k_{\perp,2}')u_2 \right] \, dk_{\perp,1}' \, dk_{\perp,2}'.$$

Since we have assumed a steady-state plasma, there is no slow time dependence, so we drop it from $\widetilde{C}$ from here onwards. The t in δn_e, is a fast time dependence, which we need to keep.

We introduce the backscattered power spectral density p_r, such that the total backscattered power P_r is given by

$$P_r = \int p_r \, d\omega. \tag{167}$$

To evaluate p_r, we multiply the backscattered amplitude, equation (153), by its complex conjugate, and we time average over a time T that satisfies equation (160) to find

$$\frac{p_r}{P_{ant}} = \int \sum_{\mu=a,b,\dots} F_\mu(k_{\perp,1}, k_{\perp,2}) \exp\left[2is(\tau_\mu(k_{\perp,1})) + ik_{\perp,1} \int_0^{\tau_\mu(k_{\perp,1})} g(\tau'') \, d\tau'' \right]$$

$$\times \delta\tilde{n}_{e,\mu}(k_{\perp,1}, k_{\perp,2}, \omega) \, dk_{\perp,1} \, dk_{\perp,2}$$

$$\times \int \sum_{\nu=a,b,\dots} F_\nu^*(k_{\perp,1}', k_{\perp,2}') \exp\left[-2is(\tau_\nu(k_{\perp,1}')) - ik_{\perp,1}' \int_0^{\tau_\nu(k_{\perp,1}')} g(\tau'') \, d\tau'' \right] \tag{168}$$

$$\times \delta\tilde{n}_{e,\nu}^*(k_{\perp,1}', k_{\perp,2}', \omega) \, dk_{\perp,1}' \, dk_{\perp,2}',$$

where P_{ant} is the total power emitted by the antenna and where we have abbreviated the slowly-varying piece of the amplitude (without density fluctuations) as

$$
\begin{aligned}
F_\mu(k_{\perp,1}, k_{\perp,2}) = {} & \frac{\Omega g_{ant}}{2c} \left[\frac{\det\left[\text{Im}\left(\boldsymbol{\Psi}_{w,\mu}\right)\right]}{\det\left(\boldsymbol{M}_{w,\mu}\right)} \right]^{\frac{1}{2}} \left[\pi\text{i}\left(g_\mu \frac{\text{d}K}{\text{d}\tau}\Big|_{\tau_\mu} \right)^{-1} \right]^{\frac{1}{2}} \\
& \times \exp\left(2\text{i}\phi_{G,\mu}\right)\ \hat{\mathbf{e}}_\mu^* \cdot \left(\boldsymbol{\epsilon}_{eq,\mu} - \mathbf{1}\right) \cdot \hat{\mathbf{e}}_\mu \frac{1}{n_{e,\mu}} \\
& \times \exp\left[-\frac{\text{i}}{4}(2\mathbf{K}_{w,\mu} + \mathbf{k}_\perp) \cdot \boldsymbol{M}_{w,\mu}^{-1} \cdot (2\mathbf{K}_{w,\mu} + \mathbf{k}_\perp) \right] \\
& \times \exp\left(\frac{\text{i}}{2} k_{\perp,1} \int_0^{\tau_\mu} g(\tau')\theta^2(\tau')\ \text{d}\tau' \right).
\end{aligned}
\tag{169}
$$

We remind readers that τ_μ is a function of $k_{\perp,1}$. Hence, $F_\nu(k'_{\perp,1}, k'_{\perp,2})$ would be evaluated at $\tau_\nu(k'_{\perp,1})$, rather than at $\tau_\nu(k_{\perp,1})$.

Moving forward, we try to match equation (168) with the Fourier transform of the correlation function $\widetilde{C}$. First, we note that $F_\mu(k_{\perp,1}, k_{\perp,2})$ depends slowly on $k_{\perp,1}$ and $k_{\perp,2}$, as we have taken the large phase term out of it. Hence, we can neglect $k_{\perp,i} - k'_{\perp,i} \sim 1/L \ll 1$, giving us

$$
F_\nu(k'_{\perp,1}, k'_{\perp,2}) \simeq F_\nu(k_{\perp,1}, k_{\perp,2}).
\tag{170}
$$

To deal with the exponential term outside $F_\mu(k_{\perp,1}, k_{\perp,2})$, we Taylor expand $\tau_\nu(k'_{\perp,1})$ about $\tau_\nu(k_{\perp,1})$

$$
\begin{aligned}
2s\left(\tau_\nu(k'_{\perp,1})\right) & + k'_{\perp,1} \int_0^{\tau_\nu(k'_{\perp,1})} g(\tau'')\ \text{d}\tau'' \\
& \simeq 2s\left(\tau_\nu(k_{\perp,1})\right) + k'_{\perp,1} \int_0^{\tau_\nu(k_{\perp,1})} g(\tau'')\ \text{d}\tau'' \\
& + \left[2K_\nu g_\nu + k'_{\perp,1} g_\nu \right] \left[\tau_\nu(k'_{\perp,1}) - \tau_\nu(k_{\perp,1}) \right].
\end{aligned}
\tag{171}
$$

In order to gain the insight we need to proceed further, we consider the following piece of equation (168),

$$
\sum_{\mu,\nu} \delta\tilde{n}_{e,\mu}(k_{\perp,1}, k_{\perp,2}, \omega)\delta\tilde{n}_{e,\nu}^*(k'_{\perp,1}, k'_{\perp,2}, \omega).
\tag{172}
$$

When $\mu \neq \nu$, τ_μ and τ_ν generally correspond to positions that, in the perpendicular direction, are many correlation lengths apart. For $\mu \neq \nu$, $\delta\tilde{n}_{e,\mu}\delta\tilde{n}_{e,\nu}^*$ can only become significant when τ_μ and τ_ν are either close to each other or connected by a length of magnetic field line of the order of the parallel correlation length. Since this only happens on a countable number of flux surfaces, we ignore this possibility, and assume that when

$\mu \neq \nu$, $\delta\tilde{n}_{e,\mu}\delta\tilde{n}^*_{e,\nu}$ is small. Hence, we find that

$$\sum_{\mu,\nu} \delta\tilde{n}_{e,\mu}(k_{\perp,1}, k_{\perp,2}, \omega)\delta\tilde{n}^*_{e,\nu}(k'_{\perp,1}, k'_{\perp,2}, \omega)$$

$$\times \exp\left[2\mathrm{i}s_\mu + \mathrm{i}k_{\perp,1}\int_0^{\tau_\mu} g(\tau'')\,\mathrm{d}\tau'' - 2\mathrm{i}s_\nu - \mathrm{i}k'_{\perp,1}\int_0^{\tau_\nu} g(\tau'')\,\mathrm{d}\tau''\right]$$

$$= \sum_\mu \delta\tilde{n}_{e,\mu}(k_{\perp,1}, k_{\perp,2}, \omega)\delta\tilde{n}^*_{e,\mu}(k'_{\perp,1}, k'_{\perp,2}, \omega) \tag{173}$$

$$\times \exp\left\{\mathrm{i}\left(2K_\mu g_\mu + k'_{\perp,1}g_\mu\right)\left[\tau_\mu(k_{\perp,1}) - \tau_\mu(k'_{\perp,1})\right]\right\}$$

$$\times \exp\left[\mathrm{i}\left(k_{\perp,1} - k'_{\perp,1}\right)\int_0^{\tau_\mu} g(\tau'')\,\mathrm{d}\tau''\right].$$

Here we can neglect the small term $\left(2K_\mu g_\mu + k'_{\perp,1}g_\mu\right)\left[\tau_\mu(k_{\perp,1}) - \tau_\mu(k'_{\perp,1})\right]$. Indeed, using

$$\tau_\mu(k_{\perp,1}) - \tau_\mu(k'_{\perp,1}) = -\frac{1}{2}\left(\left.\frac{\mathrm{d}K}{\mathrm{d}\tau}\right|_{\tau_\mu}\right)^{-1}(k_{\perp,1} - k'_{\perp,1}), \tag{174}$$

which is a result of the Bragg condition, equation (149), we show that term to be small,

$$\left(2K_\mu g_\mu + k'_{\perp,1}g_\mu\right)\left[\tau_\mu(k_{\perp,1}) - \tau_\mu(k'_{\perp,1})\right]$$

$$= \frac{1}{2}\left(\left.\frac{\mathrm{d}K}{\mathrm{d}\tau}\right|_{\tau_\mu}\right)^{-1} g_\mu(k_{\perp,1} - k'_{\perp,1})^2 \sim \frac{\lambda}{L} \ll 1. \tag{175}$$

Using equations (173) and (170), we rewrite equation (168) as

$$\frac{p_r}{P_{ant}} = \int \sum_{\mu=a,b,\ldots} \delta\tilde{n}_{e,\mu}(k_{\perp,1}, k_{\perp,2}, \omega)\delta\tilde{n}^*_{e,\mu'}(k'_{\perp,1}, k'_{\perp,2}, \omega)$$

$$\times \exp\left[\left(k_{\perp,1} - k'_{\perp,1}\right)\int_0^{\tau_\mu} g(\tau'')\,\mathrm{d}\tau''\right]\,\mathrm{d}k'_{\perp,1}\,\mathrm{d}k'_{\perp,2} \tag{176}$$

$$\times |F_\mu(k_{\perp,1}, k_{\perp,2})|^2\,\mathrm{d}k_{\perp,1}\,\mathrm{d}k_{\perp,2},$$

and we match the result to the Fourier transform of the correlation function in equation (166). We now get

$$\frac{p_r}{P_{ant}} = \frac{1}{4}\frac{\Omega^2}{c^2}g_{ant}^2\pi \int \sum_{\mu=a,b,\ldots} \frac{\det\left[\mathrm{Im}\left(\boldsymbol{\Psi}_{w,\mu}\right)\right]}{|\det\left[\boldsymbol{M}_{w,\mu}\right]|}\left|\hat{\mathbf{e}}^*_\mu \cdot \left(\boldsymbol{\epsilon}_{eq,\mu} - \mathbf{1}\right) \cdot \hat{\mathbf{e}}_\mu\right|^2$$

$$\times \left|g_\mu\left.\frac{\mathrm{d}K}{\mathrm{d}\tau}\right|_{\tau_\mu}\right|^{-1}\exp\left[2\mathrm{Im}\left(M^{-1}_{xx,\mu}\right)K_\mu^2\theta_{m,\mu}^2\right]$$

$$\times \exp\left[-2\mathrm{Im}\left(M^{-1}_{xy,\mu}\right)K_\mu\theta_{m,\mu}k_{\perp,2} + \frac{1}{2}\mathrm{Im}\left(M^{-1}_{yy,\mu}\right)k_{\perp,2}^2\right] \tag{177}$$

$$\times \frac{\left\langle\delta n_{e,\mu}^2(t)\right\rangle_t}{n_{e,\mu}^2}\widetilde{C}_\mu(k_{\perp,1}, k_{\perp,2}, \omega)\,\mathrm{d}k_{\perp,1}\,\mathrm{d}k_{\perp,2}.$$

Here, $\Delta u_\parallel$ in $\widetilde{C}_\mu$ is zero and the subscript $_\mu$ indicates that it is evaluated at $u_{\parallel,\mu}$, $\delta n_{e,\mu}^2$ is evaluated at $u_{\parallel,\mu} = -\int_0^{\tau_\mu} g(\tau')\sin\theta(\tau')\,\mathrm{d}\tau' \simeq 0$, $u_2 = 0$, and $u_1 = \int_0^{\tau_\mu} g(\tau'')\,\mathrm{d}\tau''$. Hence, $\mathbf{r} = \mathbf{q}(\tau_\mu(k_{\perp,1}))$, and so, for convenience, we have dropped the $\mathbf{r}$ dependence and denoted it with the subscript $_\mu$ instead.

7.2. Gaussian integral in $k_{\perp,2}$

We begin by manipulating equation (177) into a more wieldly form. Remarking that

$$
\begin{aligned}
-2\mathrm{Im}\left(M_{xy,\mu}^{-1}\right) K_\mu \theta_{m,\mu} k_{\perp,2} &+ \frac{1}{2}\mathrm{Im}\left(M_{yy,\mu}^{-1}\right) k_{\perp,2}^2 \\
&= \frac{1}{2}\mathrm{Im}\left(M_{yy,\mu}^{-1}\right)\left[k_{\perp,2} - 2K_\mu \theta_{m,\mu}\frac{\mathrm{Im}\left(M_{xy,\mu}^{-1}\right)}{\mathrm{Im}\left(M_{yy,\mu}^{-1}\right)}\right]^2 \\
&\quad - 2K_\mu^2 \theta_{m,\mu}^2 \frac{\left[\mathrm{Im}\left(M_{xy,\mu}^{-1}\right)\right]^2}{\mathrm{Im}\left(M_{yy,\mu}^{-1}\right)},
\end{aligned}
\tag{178}
$$

we see that the $k_{\perp,2}$ integral is a Gaussian integral. Thus, we find the $k_{\perp,2}$ selected by the signal,

$$
\begin{aligned}
k_{\perp,2} &\simeq k_{\mu,2}(\tau_\mu(k_{\perp,1})) \\
&= 2K_\mu \theta_{m,\mu}\frac{\mathrm{Im}\left(M_{xy,\mu}^{-1}\right)}{\mathrm{Im}\left(M_{yy,\mu}^{-1}\right)} \sim \frac{1}{W}.
\end{aligned}
\tag{179}
$$

Interestingly, this is small in mismatch, and is exactly zero when there is no mismatch. The backscattered power is thus

$$
\begin{aligned}
\frac{p_r}{P_{ant}} &= \frac{\pi}{4}\frac{\Omega^2}{c^2} g_{ant}^2 \int \sum_{\mu=a,b,\ldots} \frac{\det\left[\mathrm{Im}\left(\boldsymbol{\Psi}_{w,\mu}\right)\right]}{|\det\left[\boldsymbol{M}_{w,\mu}\right]|} \left|\hat{\mathbf{e}}_\mu^* \cdot \left(\boldsymbol{\epsilon}_{eq,\mu}-\boldsymbol{1}\right)\cdot\hat{\mathbf{e}}_\mu\right|^2 \\
&\quad \times \left|g_\mu\frac{\mathrm{d}K}{\mathrm{d}\tau}\bigg|_{\tau_\mu}\right|^{-1} \exp\left[-2\frac{(k_{\perp,2}-k_{\mu,2})^2}{(\Delta k_{\mu,2})^2}\right]\exp\left[-2\frac{\theta_{m,\mu}^2}{(\Delta\theta_{m,\mu})^2}\right] \\
&\quad \times \frac{\left\langle\delta n_{e,\mu}^2(t)\right\rangle_t}{n_{e,\mu}^2}\widetilde{C}_\mu(k_{\perp,1},k_{\perp,2},\omega)\,\mathrm{d}k_{\perp,1}\,\mathrm{d}k_{\perp,2}.
\end{aligned}
\tag{180}
$$

Here, we use the notation

$$
\Delta\theta_{m,\mu} = \frac{1}{K_\mu}\left(\frac{\mathrm{Im}\left(M_{yy,\mu}^{-1}\right)}{\left[\mathrm{Im}\left(M_{xy,\mu}^{-1}\right)\right]^2 - \mathrm{Im}\left(M_{xx,\mu}^{-1}\right)\mathrm{Im}\left(M_{yy,\mu}^{-1}\right)}\right)^{\frac{1}{2}},
\tag{181}
$$

which gives the characteristic $1/e^2$ width of the mismatch attenuation and

$$
\Delta k_{\mu,2} = 2\left(\frac{-1}{\mathrm{Im}\left(M_{yy,\mu}^{-1}\right)}\right)^{\frac{1}{2}},
\tag{182}
$$

which gives us the wavenumber resolution (in $1/e^2$). For those seeking to design a synthetic DBS to study data from gyrokinetic simulations, equation (180) is the form of the backscattered signal that we recommend using.

If we take the $k_{\perp,2}$ wavenumber resolution, $\Delta k_{\mu,2}$, to be small, we can evaluate the Gaussian integral by using the approximation $k_{\perp,2} \simeq k_{\mu,2} \simeq 0$ in $\widetilde{C}_\mu$. After doing this,

we get

$$\frac{p_r}{P_{ant}} = \frac{\sqrt{2\pi^3}}{4} \frac{\Omega^2}{c^2} g_{ant}^2 \int \sum_{\mu=a,b,\dots} \frac{\det\left[\mathrm{Im}\left(\boldsymbol{\Psi}_{w,\mu}\right)\right]}{\left|\det\left[\boldsymbol{M}_{w,\mu}\right]\right|} \left|\hat{\mathbf{e}}_\mu^* \cdot \left(\boldsymbol{\epsilon}_{eq,\mu} - \mathbf{1}\right) \cdot \hat{\mathbf{e}}_\mu\right|^2$$

$$\times \left|g_\mu \frac{\mathrm{d}K}{\mathrm{d}\tau}\bigg|_{\tau_\mu}\right|^{-1} \left[-\mathrm{Im}\left(M_{yy,\mu}^{-1}\right)\right]^{-\frac{1}{2}} \exp\left(-2\frac{\theta_{m,\mu}^2}{\left(\Delta\theta_{m,\mu}\right)^2}\right) \tag{183}$$

$$\times \frac{\left\langle \delta n_{e,\mu}^2(t)\right\rangle_t}{n_{e,\mu}^2} \widetilde{C}_\mu(k_{\perp,1}, k_{\mu,2}, \omega) \,\mathrm{d}k_{\perp,1}.$$

The final integral in $k_{\perp,1}$ cannot be evaluated analytically. However, we can make a few simplifications to the current form of the backscattered power, thereby making clearer the physics involved.

7.3. Final simplifications

We hone in on three pieces of equation (183), showing how they may be normalised and re-expressed in more explicit forms. We begin by writing equation (183) as

$$\frac{p_r}{P_{ant}} = \frac{\sqrt{\pi^3}e^4}{2c^2\Omega^2\epsilon_0^2 m_e^2 \bar{W}_y} \sum_{\mu=a,b,\dots} \int \varepsilon_\mu \frac{\bar{W}_y \det\left[\mathrm{Im}\left(\boldsymbol{\Psi}_w\right)\right]}{\sqrt{2}\left|\det\left[\boldsymbol{M}_w\right]\right|\left[-\mathrm{Im}\left(M_{yy}^{-1}\right)\right]^{\frac{1}{2}}} \exp\left(-2\frac{\theta_m^2}{\left(\Delta\theta_m\right)^2}\right)$$

$$\times \left\langle \delta n_e^2(t)\right\rangle_t \widetilde{C}_\mu(k_{\perp,1}, k_{\mu,2}, \omega) \, g_{ant}^2 \left|g_\mu \frac{\mathrm{d}K}{\mathrm{d}\tau}\bigg|_{\tau_\mu}\right|^{-1} \mathrm{d}k_{\perp,1}, \tag{184}$$

where ε and $\bar{W}_y$ will be introduced in the following lines. The first piece we focus on is related to the polarisation; we call this piece ε,

$$\varepsilon_\mu = \frac{\Omega^4\epsilon_0^2 m_e^2}{e^4 n_{e,\mu}^2}|\hat{\mathbf{e}}_\mu^* \cdot \left(\boldsymbol{\epsilon}_{eq,\mu} - \mathbf{1}\right) \cdot \hat{\mathbf{e}}_\mu|^2. \tag{185}$$

The second pertains to the widths (beam) and curvatures (beam and field lines),

$$\frac{\bar{W}_y}{\sqrt{2}} \frac{\det\left[\mathrm{Im}\left(\boldsymbol{\Psi}_{w,\mu}\right)\right]}{\left|\det\left[\boldsymbol{M}_{w,\mu}\right]\right|\left[-\mathrm{Im}\left(M_{yy,\mu}^{-1}\right)\right]^{\frac{1}{2}}}. \tag{186}$$

Here $\bar{W}_y$ is the value that $W_y = \sqrt{2/\mathrm{Im}(\Psi_{yy})}$ takes at the beam waist, in vacuum. The final piece contains the integrable divergence

$$g_{ant}^2 \left|g_\mu \frac{\mathrm{d}K}{\mathrm{d}\tau}\bigg|_{\tau_\mu}\right|^{-1} \mathrm{d}k_{\perp,1}. \tag{187}$$

We first look into the polarisation piece, ε. Using equation (22) and recalling that the polarisation $\hat{\mathbf{e}}$ is the eigenvector of $\boldsymbol{D}$ corresponding to $H = 0$, see Appendix A.1, we re-express the polarisation piece as

$$\varepsilon_\mu = \frac{\Omega^4\epsilon_0^2 m_e^2}{e^4 n_{e,\mu}^2} \left|\frac{c^2}{\Omega^2}K_\mu^2\left[1 - \left(\hat{\mathbf{K}}_\mu \cdot \hat{\mathbf{e}}_\mu\right)^2\right] - 1\right|^2. \tag{188}$$

This expression can be made simpler for the O-mode, but is less obvious for the X-mode. Assuming the polarisation is reasonably well-aligned upon entering the
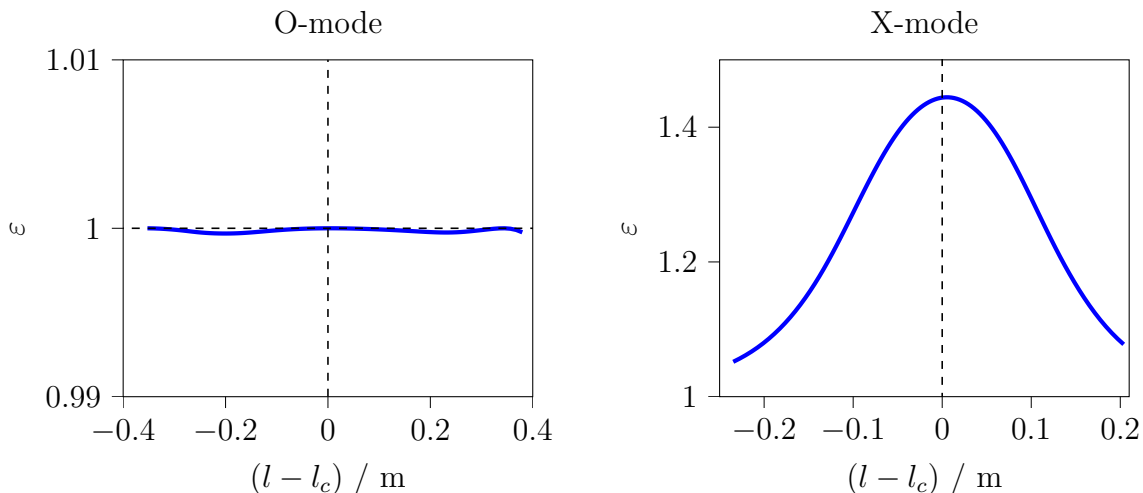
Figure 9: The O-mode polarisation piece (left) and that of the X-mode (right) along the ray, for the MAST test scenario. Here $l - l_c$ is the distance from the cut-off, as measured by the arc-length along the central ray. We define the cut-off to be where K is minimum. Notice that the O-mode polarisation piece is almost exactly 1, as expected. The X-mode polarisation piece does seem to give more localisation to the cut-off, but this may not be generally true.

plasma, we have $\hat{\mathbf{e}} \cdot \hat{\mathbf{b}} \simeq 1$ for the O-mode. For the cold plasma dispersion relation, $\mathbf{K} = K\cos\theta_m\hat{\mathbf{u}}_1 + K\sin\theta_m\hat{\mathbf{b}}$ by definition of the mismatch angle, and consequently $|\hat{\mathbf{K}} \cdot \hat{\mathbf{e}}| \sim \theta_m$ for the O-mode. Thus, the O-mode polarisation piece is

$$\varepsilon_\mu = \frac{\Omega^4 \epsilon_0^2 m_e^2}{e^4 n_{e,\mu}^2}\left(\frac{c^2}{\Omega^2}K_\mu^2 - 1\right)^2. \tag{189}$$

Making use of the O-mode dispersion, $\epsilon_{bb,\mu} - K_\mu^2 c^2/\Omega^2 \simeq 0$, we find that

$$\varepsilon_\mu \simeq 1, \tag{190}$$

which is constant, see Figure 9 (left). For the X-mode, even when $\theta_m = 0$, the polarisation piece ε depends on the relative sizes of Ω_{ce} and Ω_{pe}. Since we do not make any assumptions about them, we will not further simplify the polarisation piece for the X-mode in this work. Should one wish to calculate the polarisation piece of the X-mode, one should use its full expression, given in equation (188). An example is given in Figure 9 (right).

Subsequently, we briefly discuss the piece related to the widths and curvatures,

$$\frac{\bar{W}_y}{\sqrt{2}}\frac{\det\left[\mathrm{Im}\left(\boldsymbol{\Psi}_{w,\mu}\right)\right]}{|\det\left[\boldsymbol{M}_{w,\mu}\right]|\left[-\mathrm{Im}\left(M_{yy,\mu}^{-1}\right)\right]^{\frac{1}{2}}}. \tag{191}$$

Due to the complexity of this piece, we do not simplify it any further. Instead, we explain our choice of normalisation. The idea is that we want this piece to be unity under certain conditions which make the problem easier. Consider the waist of a Gaussian beam in vacuum. Take $\boldsymbol{M} = \boldsymbol{\Psi}$ for simplicity. Assume also that this beam is not astigmatic,

that is, the beam widths are minimised at the same point in τ. At this same point, the real parts of $\boldsymbol{\Psi}$ are simply zero. If $\boldsymbol{\Psi}_w$ is also diagonal in the $(\hat{\mathbf{x}}, \hat{\mathbf{y}}, \hat{\mathbf{g}})$ basis, then the prefactor $\bar{W}_y/\sqrt{2}$ ensures that this piece is unity.

Finally, we simplify the piece containing the integrable divergence. First, differentiate the Bragg condition with respect to τ

$$\frac{\mathrm{d}k_{\perp,1}}{\mathrm{d}\tau} = -2\frac{\mathrm{d}K}{\mathrm{d}\tau}, \tag{192}$$

and use this to find that

$$\mathrm{d}k_{\perp,1} \left| g_\mu \frac{\mathrm{d}K}{\mathrm{d}\tau}\bigg|_{\tau_\mu} \right|^{-1} = \frac{2}{g}\mathrm{d}\tau_\mu. \tag{193}$$

Since we sum over μ, equation (180), we can express the integration as being over the beam path,

$$\frac{2}{g_\mu}\mathrm{d}\tau_\mu = \frac{2}{g^2}\mathrm{d}l. \tag{194}$$

This piece is thus

$$g_{ant}^2 \left| g_\mu \frac{\mathrm{d}K}{\mathrm{d}\tau}\bigg|_{\tau_\mu} \right|^{-1} \mathrm{d}k_{\perp,1} = \frac{g_{ant}^2}{g^2}\mathrm{d}l, \tag{195}$$

where one has to be careful to use the form of the dispersion relation used in our beam tracing derivation, equation (23). Using the definition of H, we find that equation (132) gives us $g_{ant} = 2c/\Omega$ (since we take the antenna to be in vacuum).

In summary, after all these simplifications are applied, equation (184) is now

$$\begin{aligned}
\frac{p_r}{P_{ant}} = \frac{\sqrt{\pi^3}e^4}{2c^2\Omega^2\epsilon_0^2 m_e^2 \bar{W}_y} \int \varepsilon_\mu \frac{g_{ant}^2}{g^2} \frac{\bar{W}_y \det\left[\mathrm{Im}\left(\boldsymbol{\Psi}_w\right)\right]}{\sqrt{2}\left|\det\left[\boldsymbol{M}_w\right]\right|\left[-\mathrm{Im}\left(M_{yy}^{-1}\right)\right]^{\frac{1}{2}}} \\
\times \exp\left(-2\frac{\theta_m^2}{(\Delta\theta_m)^2}\right)\left\langle\delta n_e^2(t)\right\rangle_t \widetilde{C}_l(\omega)\,\mathrm{d}l.
\end{aligned} \tag{196}$$

We remind readers that the variables in this equation are now functions of arc-length along the ray, that is $\tau(l)$ and $k_{l,1} = k_{\perp,1}(l)$. As such, we have dropped the subscript $_\mu$. The notation $\widetilde{C}_l$ indicates that the correlation function is evaluated at $\mathbf{q}(\tau(l))$, $k_{l,1}(l)$, $k_{\perp,2} = 0$, and $\Delta u_\parallel = 0$, which are all functions of arc-length as well. Note that ε is given by equation (188); for the O-mode, this can be simplified to equation (190), while we do not further simplify it for the X-mode.

Unlike typical papers on DBS [2, 83, 84, 85], our model does not require one to assume that the signal comes entirely from the cut-off. We will later assess the validity of this assumption. Literature on reciprocity does not *a priori* make such an assumption [24, 25], and we now compare our work with theirs. The beam model is applicable in general tokamak geometry (and some regimes of stellarators), can easily account for a wide variety of initial beam conditions and equilibrium density profiles, and does not rely on assuming the density fluctuations have an exponential spectrum. Consequently, we better understand the effect of geometry on wavenumber resolution. We can also perform a more realistic assessment of localisation. Finally, for the first time, we present

a quantitative description of the mismatch attenuation as a function of beam properties. The subsequent sections explore localisation, wavenumber resolution, and mismatch attenuation, which are various pieces of equations (180) and (196).

8. Localisation

In the previous section, we expressed the backscattered signal as a line integral along the central ray, equation (196). In this section, we study the integrand of this equation to understand where, along the line integral, does most of the signal come from. Traditionally, the DBS signal is thought to come from the region around the cut-off [2, 24]; we now use the beam model to evaluate and understand this insight. The integrand in equation (196) consists of two parts, the turbulence that one seeks to measure $\langle \delta n_e^2(t) \rangle_t \, \widetilde{C}_l(\omega)$, and the prefactor

$$\frac{g_{ant}^2}{g^2} \frac{\bar{W}_y \det \left[\mathrm{Im} \left(\boldsymbol{\Psi}_w \right) \right]}{\sqrt{2} \left| \det \left[\boldsymbol{M}_w \right] \right| \left[-\mathrm{Im} \left(M_{yy}^{-1} \right) \right]^{\frac{1}{2}}}, \tag{197}$$

which we call the localisation. Other authors refer to analogous quantities as the spatial resolution [24], instrumentation response function [86, 87], weighting function [25], or filter function [88]. In our expression of the localisation, we have deliberately omitted the pieces associated with polarisation, equation (188), and mismatch

$$\exp \left[-2 \frac{\theta_m^2}{\left(\Delta \theta_m \right)^2} \right]. \tag{198}$$

The mismatch may indeed affect localisation; in fact, it is the dominant mechanism of localisation in the *large mismatch angle* ordering, see Section 11. However, assuming we are not dealing with such extreme situations, we deem it more physically insightful to discuss the effect of mismatch later (Section 10).

We analyse two contributions to the localisation, equation (197), which we call the *ray* piece

$$\frac{g_{ant}^2}{g^2}, \tag{199}$$

and the *beam* piece

$$\frac{\bar{W}_y \det \left[\mathrm{Im} \left(\boldsymbol{\Psi}_w \right) \right]}{\sqrt{2} \left| \det \left[\boldsymbol{M}_w \right] \right| \left[-\mathrm{Im} \left(M_{yy}^{-1} \right) \right]^{\frac{1}{2}}}. \tag{200}$$

They are named as such because the former can be determined with ray tracing alone, while the latter requires beam tracing. The *ray* piece requires one to use the appropriate dispersion relation, equation (23), to calculate the group velocity. We now briefly discuss the physical interpretations of these two pieces. It seems that the ray piece appears loosely related to scattering efficiency. The beam piece is more complicated. The beam area is proportional to $\det \left[\mathrm{Im} \left(\boldsymbol{\Psi}_w \right) \right]$; hence, that part decreases as the beam expands. However, the interpretation of $\left| \det \left[\boldsymbol{M}_w \right] \right|$ is less straightforward. For a circular beam in vacuum, it turns out that the overall beam piece also decreases as the beam expands.
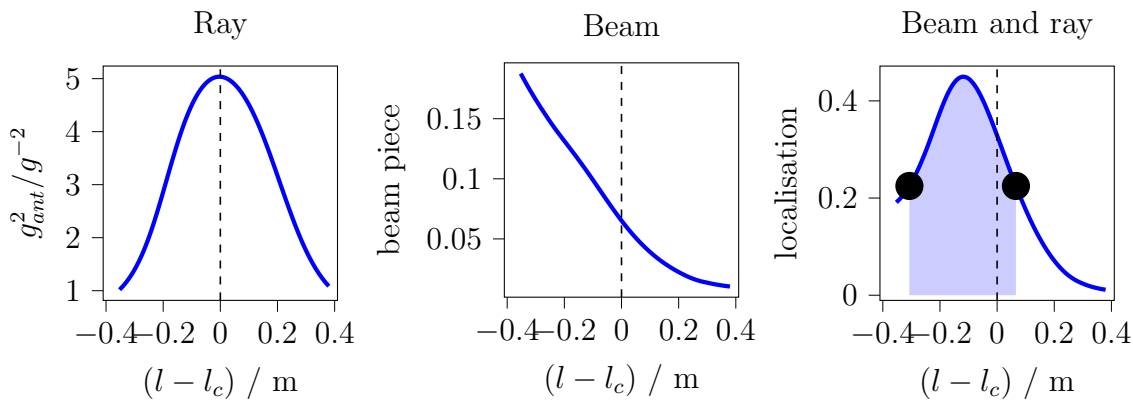
Figure 10: Ray (left) and beam (middle) contributions to localisation as a function of distance along the central ray from the cut-off location for the MAST test scenario. The beam piece is given explicitly in equation (200). Product of the ray and beam pieces (right); the shaded area is 80% of the total area under the curve. Black points mark the start and end of the shaded area; note that we have chosen these points such that they have the same ordinate value, that is, the same value of localisation. The corresponding half width is 19cm.

We now apply our model to our MAST test scenario. In Figure 10, we show the localisation due to the *ray* and *beam* pieces. We see that there is some localisation to the cut-off due to the *ray* piece. Here, we define the cut-off to be where K is minimum. Since the localisation associated with the *ray* and *beam* pieces is complicated, we use the following method to determine the localisation length. First, we integrate the localisation with respect to arc length along the central ray, from the point the beam enters the plasma until the point it leaves. Secondly, we choose two points along the ray, integrate localisation with respect to arc length l from the first point to the second, and make sure that this result is 80% that of the first integral. These two points show the start and end of the region where most of the signal is coming from. In this work, we choose the first and second points such that the value of the localisation piece is the same at these two points. Thirdly, we take the localisation length to be half of the arc length between the first and second points. The localisation length associated with the combined *beam* and *ray* pieces calculated by this method is 19cm, which is large, indicating that, in experiments, there are probably other mechanisms of localisation.

We now consider the turbulence spectrum, which may further contribute to localisation. For electrostatic turbulece, references [89, 90, 91] suggest that the spectrum is of the form $\widetilde{C}_\mu(k_{\perp,1}, k_{\mu,2}, \omega) \propto k_\perp^{-10/3}$ for $k_\perp \rho_i \ll 1$ and $\widetilde{C}_\mu(k_{\perp,1}, k_{\mu,2}, \omega) \propto k_\perp^{-13/3}$ for $k_\perp \rho_i \gg 1$. The spectrum piece associated with the backscattered power is thus

$$\left(\frac{K}{K_{ant}}\right)^{-\frac{10}{3}} \quad \text{or} \quad \left(\frac{K}{K_{ant}}\right)^{-\frac{13}{3}}, \tag{201}$$

where we have used the Bragg condition to express $k_{\perp,1}$ in terms of the beam's wavenumber. Since the magnitude of the wavevector is minimum at the cut-off, there
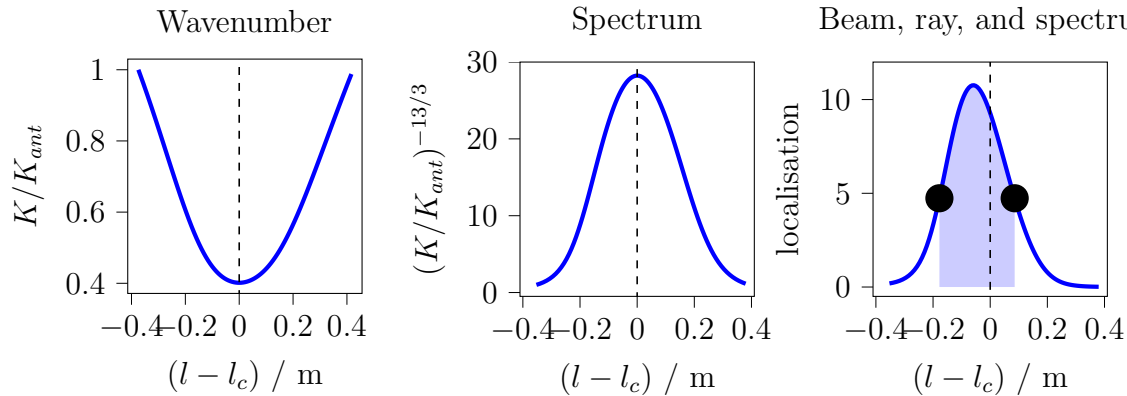
Figure 11: Normalised wavenumber along the central ray (left). Localisation due to the power-law turbulence spectrum (middle) and overall localisation (right). Here l_c is the distance along the central ray, from launch to cut-off location. The overall localisation is the product of equations (198), (200), and (201). The shaded area is 80% of the total area under the curve, and the black points mark the start and end of the shaded area. The corresponding half width is 13cm. Note that we have chosen the black points such that they have the same ordinate value, that is, the same value of localisation.

is significantly more turbulence with the appropriate $k_{\perp,1}$ for backscattering. We now multiply the piece $(K/K_{ant})^{-13/3}$, Figure 11 (middle), together with the beam and ray pieces, and see what this overall localisation gives, Figure 11 (right). We find the localisation length, after taking the spectrum into account, to be around 13cm for our MAST test scenario, Figure 11. One more consideration is the effect of the Doppler shift on localisation, which we do not assess in this work because it requires assuming particular realisations of turbulence. Investigating this effect using gyrokinetic simulations of turbulence together with a synthetic DBS based on the beam model would be interesting further work.

It is important to note that this distance $l-l_c$, where l_c is the arc-length of the cut-off position, is measured along the ray. For an O-mode beam, the ray's radial component of group velocity is small near the cut-off, hence more of the signal is coming from fairly similar flux surfaces, unlike what it might ostensibly seem given the fairly large half-width, see Figure 12. Apart from that, it is interesting to note that the peak of localisation is shifted away from the cut-off, by around $l - l_c = 6$cm or so, due to the changing *beam* piece near the cut-off. The physical intuition as to why the *beam* piece decreases as the beam propagates is as follows: the MAST DBS was designed to have the beam waist before the plasma, hence the beam is always getting wider while in the plasma. Thus far, we have shown plots of the integrand of equation (196), and calculated the associated localisation lengths. Since these lengths are calculated from the cumulative integrals of the localisation pieces, we plot the cumulative integrals themselves in Figure 13.

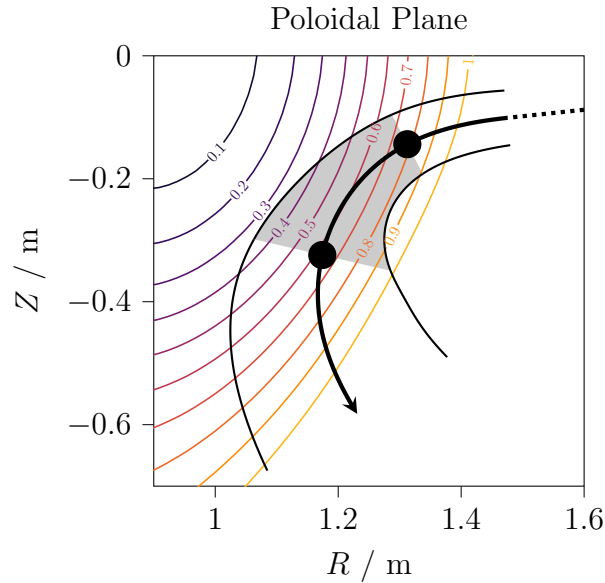Since every point along the ray is associated with a particular $k_{\perp,1}$ as a result of the

Figure 12: Most of the signal (80%) comes from the region between the two black points. The thick solid line shows the path of the central ray. Thin solid lines give the 1/e positions of the Gaussian beam's electric field, and the dotted lines show the ray's propagation in vacuum.
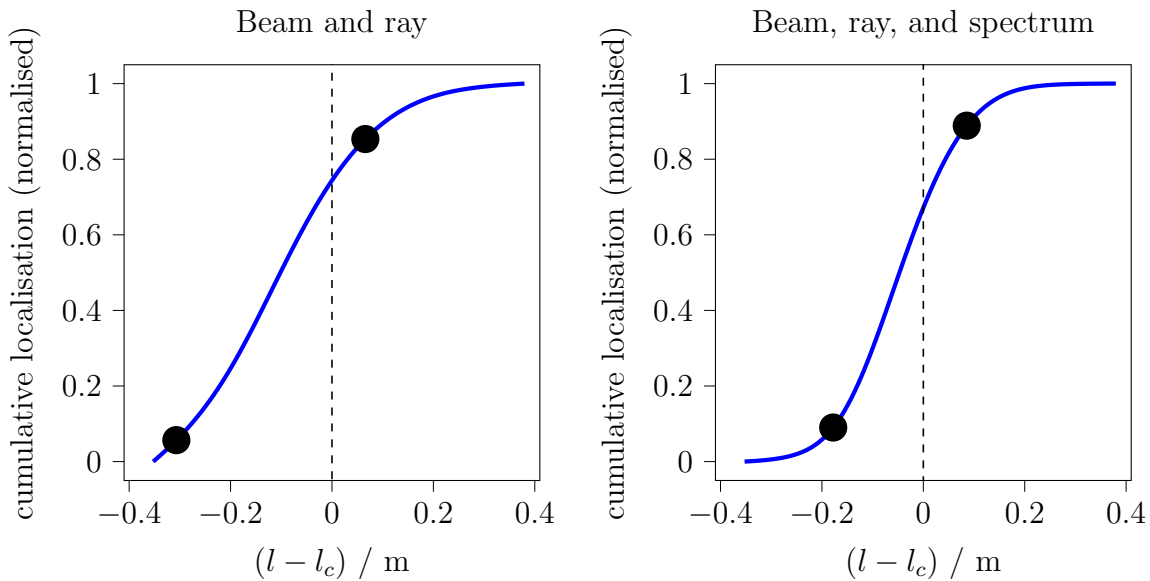

Figure 13: Here we show the cumulative integrals of localisation for the MAST test scenario, normalised such that it is 0 upon entering the plasma, and 1 when leaving. On the left, we look at the *beam* and *ray* pieces, and on the right, we include the *spectrum* piece as well. These pieces are shown as a function of arc length from the cut-off, $l - l_c$. The vertical dashed line shows the location of the cut-off. The two black points in each figure correspond to that of Figure 10 (right) and Figure 11 (right), indicating the start and end of 80% range, which gives where most of the backscattered signal comes from.

stationary phase integral in Section 6.2, it is impossible to divorce the localisation and $k_{\perp,1}$ resolution. Instead of $k_{\perp,1}$ resolution, it is more physically suitable to think of the spread of backscattered $k_{\perp,1}$ as localisation along the ray. Nonetheless, we show how to calculate the associated $k_{\perp,1}$ resolution from the spatial localisation in Section 9.1.

9. Wavenumber resolution

The wavenumber resolution is different for $k_{\perp,1}$ and $k_{\perp,2}$. The calculation of the former follows from the previous section on localisation, while that of the latter is simply given by equation (182). Consequently, this section is split into two parts, discussing the $k_{\perp,1}$ and $k_{\perp,2}$ resolutions in turn.

9.1. $k_{\perp,1}$ resolution

The $k_{\perp,1}$ resolution, $\Delta k_{\perp,1}$, cannot be divorced from the localisation, Section 8. Nonetheless, one may consider it insightful to calculate it. Since the *ray* piece as a function of backscattered $k_{\perp,1}$ diverges at cut-off, namely at $k_{l,1} = -2K(l_c)$, one might wrongly suspect that the dominant backscattered $k_{l,1}$ comes from the cut-off as well. To properly deal with this divergence, which is integrable, we instead consider the cumulative integral of the *ray* piece. We show this in Figure 14. As we can see from the figure, the median backscattered $k_{\perp,1}$ is not exactly that of the cut-off, regardless of whether we use the spectrum piece or not. The divergence means that it is not particularly insightful to calculate and plot the localisation, the integrand of equation (184), to find the backscattered $k_{\perp,1}$ resolution. Instead, we directly take a cumulative integral of the localisation piece, and calculate the resolution from there, see Figure 14.

9.2. $k_{\perp,2}$ resolution

To understand the width of the Gaussian, $\Delta k_{\mu,2}$, we first consider a simple case with $M_{xy,\mu} = 0$. Then, $M_{yy,\mu}^{-1} = 1/M_{yy,\mu}$. Remembering that $M_{yy,\mu} = \Psi_{yy,\mu}$ exactly, and using the definitions given by equations (15) and (16), we find that equation (182) gives

$$\Delta k_{\mu,2} = \frac{2\sqrt{2}}{W_{y,\mu}} \left[1 + \frac{1}{4} K_\mu^2 W_{y,\mu}^4 \left(\frac{1}{R_{b,y,\mu}} \right)^2 \right]^{1/2} . \tag{202}$$

This recovers the widely-used expression for the wavenumber resolution for a circular beam in a slab. We do not see the corrections due to the curvature of the magnetic field lines or the magnetic shear in equation (202) because we have taken $M_{xy,\mu} = 0$. As useful as this might have been to gain some physical insight, in general, we cannot neglect $M_{xy,\mu}$. The corrections due to curvature and shear of the magnetic field are therefore important. These corrections affect the wavenumber resolution in a way that in general cannot be easily further simplified. Hence, one has to use equation (182) in its presented form to determine the wavenumber resolution. We now apply our full
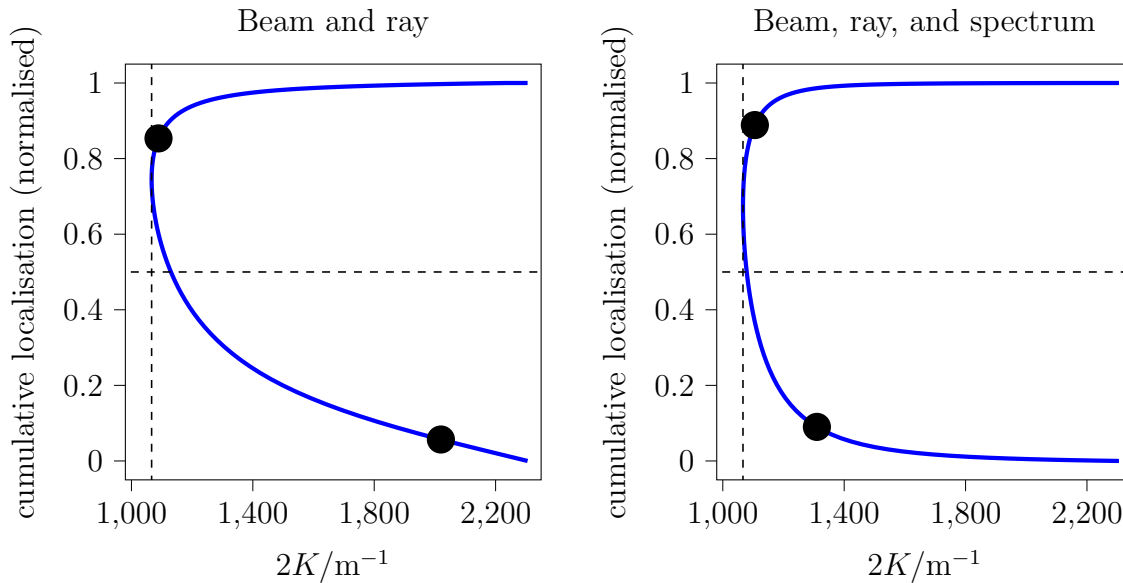
Figure 14: Here we show the normalised cumulative integrals of localisation as a function of backscattered $k_{\perp,1} = -2K$ (given by the Bragg condition) for the MAST test scenario. On the left, we look at the *beam* and *ray* pieces, and on the right, we include the *spectrum* piece as well. These two plots are analogous to those in Figure 13; the difference being that here we plot the cumulative localisation with respect to the backscattered wavenumber rather than arc-length along the ray. The start and end of the 80% range are marked on the graphs. The vertical dashed line indicates the backscattered $k_{\perp,1}$ at the cut-off. Note that the derivatives are infinite at the cut-off, but the plots themselves do not diverge, showing that the localisation piece is indeed integrable. The backscattered $|k_{\perp,1}|$ at the cutoff is $1070\mathrm{m}^{-1}$, while the values of $|k_{\perp,1}|$ at the ends of the 80% range are $2020\mathrm{m}^{-1}$ and $1090\mathrm{m}^{-1}$ (left) and $1310\mathrm{m}^{-1}$ and $1110\mathrm{m}^{-1}$ (right). The intersection of the horizontal dashed lines and the curves give the median backscattered $k_{\perp,1}$.

model, equation (182), to our MAST test scenario, Figure 15. By noticing the difference between the solid and dash-dot lines in the figure, one sees that the corrections indeed significantly affect wavenumber resolution.

In our model, the curvature of the cut-off surface does not affect the wavenumber resolution at all. One can understand this as follows. Physically, it is the curvature of the field lines and the magnetic shear that are important, since the beam is scattered off the turbulent fluctuations perpendicular to the field lines. The beam is not scattered from the cut-off surface per se — hence, strictly speaking, it is not the curvature of the cut-off surface that is important, as previously argued [2, 25].
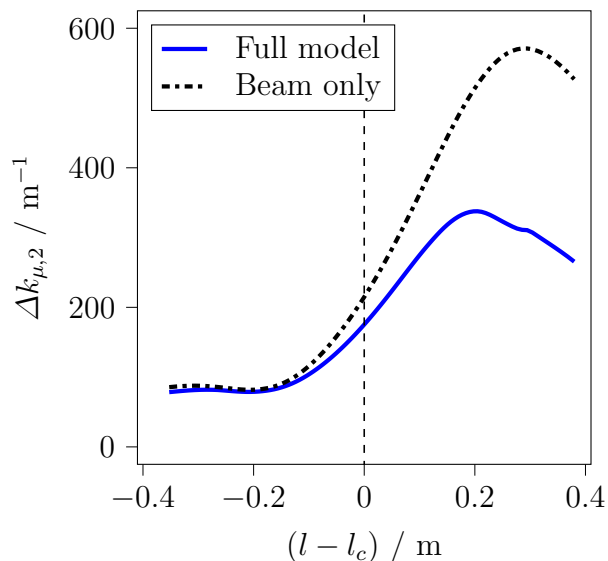
Figure 15: Wavenumber resolution for $k_{\perp,2}$ as a function of distance from the cut-off along the central ray $l - l_c$ for our MAST test scenario. The solid blue line includes the corrections arising from curvature and shear of $\hat{\mathbf{b}}$, while the dash-dot black line does not have these corrections, and only uses the beam properties.

10. Mismatch

The backscattered spectral density decays exponentially with mismatch, $p_r \propto \exp[-2\theta_{m,\mu}^2/(\Delta\theta_{m,\mu})^2]$, where $\Delta\theta_{m,\mu}$ is given by equation (181). This is consistent with our choice to take the mismatch angle to be small, such that the backscattered signal is large enough to detect. Like we did with the wavenumber resolution, we take $M_{xy,\mu} = 0$ to simplify the expression in order to gain some physical insight, getting

$$\Delta\theta_{m,\mu} = \frac{1}{K_\mu}\left[-\mathrm{Im}\left(\frac{1}{M_{xx,\mu}}\right)\right]^{-1/2}. \tag{203}$$

We write this out in full,

$$\Delta\theta_{m,\mu} = \frac{\sqrt{2}}{W_{x,\mu}K_\mu}\left[1 + \frac{W_{x,\mu}^4 K_\mu^2}{4R_{b,M,\mu}^2}\right]^{\frac{1}{2}}, \tag{204}$$

where we use the shorthand

$$\frac{1}{R_{b,M,\mu}} = \frac{1}{R_{b,x,\mu}} + \left(\hat{\mathbf{b}}\cdot\nabla\hat{\mathbf{b}}\cdot\hat{\mathbf{g}}\right)_\mu. \tag{205}$$

It has been reported [30, 33] that for high K, the backscattered signal's amplitude is especially sensitive to the toroidal steering angle. This can be explained by mismatch. At a given finite mismatch angle, the attenuation due to mismatch is larger at larger K_μ, as seen from equation (204) and from Figure 16. Indeed, for

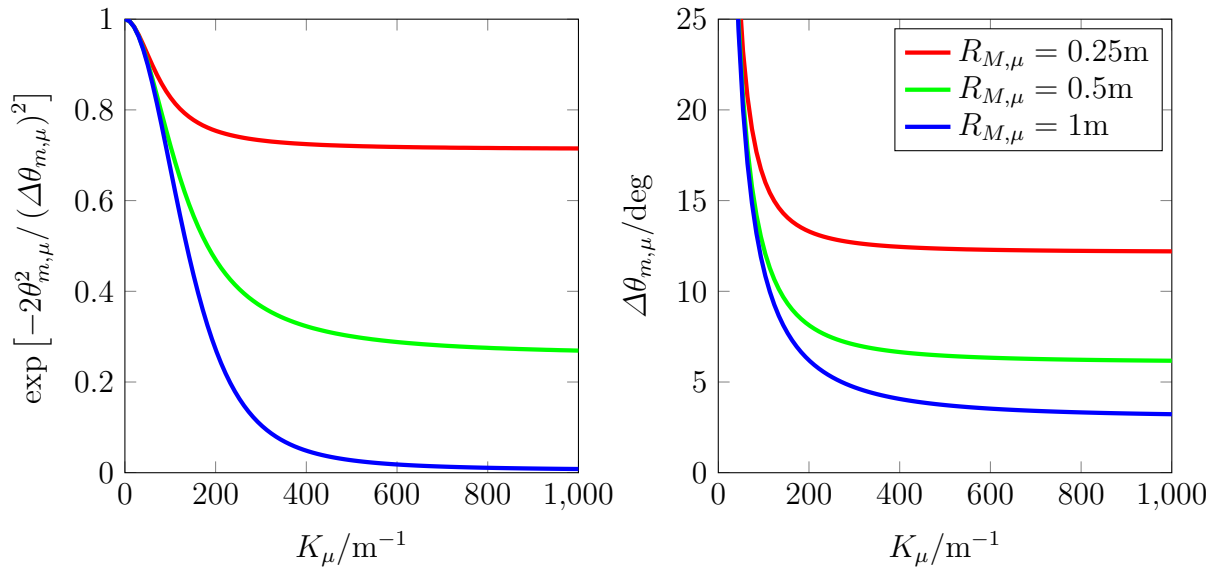$$K_\mu \gg \frac{2R_{b,M,\mu}}{W_{x,\mu}^2}, \tag{206}$$

Figure 16: How beam parameters at the scattering location influence the attenuation due to mismatch. We do not use beam tracing for these graphs; instead, we vary the beam properties by hand and see what happens. Here, we have $1/R_M = 1/R_x + \hat{\mathbf{b}} \cdot \nabla \hat{\mathbf{b}} \cdot \hat{\mathbf{g}}$, $M_{xy} = 0$, $W_x = 7.5$cm, and $\theta_m = 5°$. The line colours correspond to the same R_M for both graphs.

equation (204) reduces to

$$\exp\left[-2\frac{\theta_{m,\mu}^2}{(\Delta\theta_{m,\mu})^2}\right] \approx \exp\left(-\theta_{m,\mu}^2 \frac{4R_{b,M,\mu}^2}{W_{x,\mu}^2}\right), \qquad (207)$$

at which point further increasing K_μ has no effect on the mismatch attenuation. These considerations are especially important when designing DBS systems with no toroidal optimisation; there will be a finite mismatch over many of the channels, and this will be more problematic at larger wavevectors. Understanding mismatch attenuation will help one to mitigate this issue.

We proceed to apply the unsimplified expression for mismatch attenuation, equation (181), to a real tokamak, Figure 17. The beam and equilibrium plasma properties account for the experimentally-observed mismatch attenuation, and not backscattering from some $k_\parallel$ (which we neglect in our model). This preliminary analysis of MAST data is a good proof of concept; we now understand, and are able to calculate, how mismatch attenuates the DBS signal. A more detailed analysis of the other channels (different frequencies) and other times will be performed in a future paper, which will enable us to better evaluate our model for use in real plasmas. This advancement means that we can now operate DBS in regimes where the mismatch is small, but not so small as to be negligible (as was required previously). New insights can thus be gained from existing data, and new experiments can be performed with less strict tolerances.
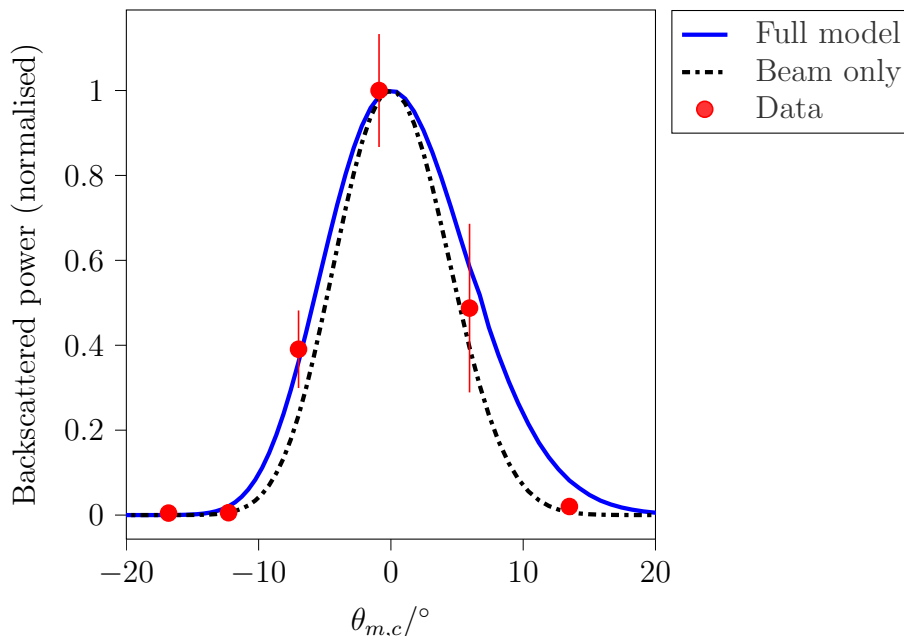
Figure 17: Red points indicate DBS data from repeated shots, where only the toroidal launch angle was varied [30]. We have taken there to be a 1.1° systematic error in the steering mirror's rotation angle, which affects the launch angles of the beam. The data points are from similar flux surfaces, but at different mismatch angles. Hence, the attenuation that we see is mainly from the mismatch, since we expect the turbulent fluctuations to be largely the same. The solid blue line indicates the model's predicted attenuation due to mismatch, $\exp\left[-2\theta_{m,c}^2 / \left(\Delta\theta_{m,c}\right)^2\right]$, given the beam properties at the cut-off when we launch the beam at various toroidal angles. The dash-dot black line shows the attenuation but with $\Delta\theta_{m,c}$ calculated from $\boldsymbol{\Psi}_w$ instead of $\boldsymbol{M}_w$, that is, calculated only from the beam properties without the corrections arising from the curvature and shear of $\hat{\mathbf{b}}$.

11. Backscattered electric field and power: large mismatch angle ordering

At the end of Section 5, we introduced the *small mismatch angle* and *large mismatch angle* orderings. Thus far, we have focused on the former. That is, we have taken $\theta_m \sim \lambda/W \ll 1$ along the beam. When the mismatch angle is not small at every point along the beam (*large mismatch angle* ordering), we consider only the simplified case in which one point along the path has no mismatch, $\tau = \tau_0$, and that the mismatch angle is large elsewhere.

To begin, we remind readers of the exponentially decaying piece in equation (127)

$$\tilde{A}_r \propto \exp\left[-\frac{\mathrm{i}}{4}\left(2K\sin(\theta + \theta_m) + k_{\perp,1}\sin\theta\right)^2 M_{xx}^{-1}\right], \tag{208}$$

where we have used equation (141). Since $k_{\perp,1} \sim K$ and $K^2 M_{xx}^{-1} \sim W^2/\lambda^2 \gg 1$, the signal is localised to the points where the mismatch is zero, $\theta_m = 0$, regardless of whether those are near the cut-off or not; due to equation (137), $\theta = 0$ at these points as well.

At the location with zero mismatch, the dominant scattered wavevector is given by the Bragg condition at this point. In a case in which the mismatch angle does not vanish at any point along the ray, we would need to use a steepest descent method to optimise for both the real (mismatch attenuation) and imaginary (stationary phase, conventionally called the Bragg condition) parts of the exponential. However, we will not cover this here.

We perform a Taylor expansion around the point of zero mismatch, for $g(\tau - \tau_0) \sim W$, which is a sensible ordering because the equilibrium properties such as the mismatch vary on length scales of L. Hence, a distance of W away from zero mismatch, we expect the mismatch to be $\sim W/L$. Thus, the argument of equation (208) is of order unity in the region $g(\tau - \tau_0) \sim W$, which means the backscattered signal is significantly attenuated away from this region. The Bragg condition is also not exactly met away from τ_0, hence

$$2K_0 + k_{\perp,1} \sim \frac{1}{W}, \tag{209}$$

which we will later prove in equation (222).

We begin by introducing a few more orderings. From earlier, we had $\theta_0 = \theta_{m,0} = 0$. However, the derivatives of both θ and θ_m change on the length scale L,

$$\frac{\mathrm{d}\theta}{\mathrm{d}\tau} \sim \frac{\mathrm{d}\theta_m}{\mathrm{d}\tau} \sim \frac{1}{\tau_L}, \tag{210}$$

where $\tau_L \sim L/g$; at a distance of L away from τ_0, the mismatch is large $\theta \sim \theta_m \sim 1$. Using these orderings, we find that

$$(\tau - \tau_0) \frac{\mathrm{d}}{\mathrm{d}\tau} \left(2K_x - k_{\perp,1} \sin\theta \right)\big|_{\tau_0} \simeq -2K_0 \frac{\mathrm{d}\theta_m}{\mathrm{d}\tau}\bigg|_{\tau_0} (\tau - \tau_0) \sim \frac{1}{W}, \tag{211}$$

and

$$(\tau - \tau_0)^2 \frac{\mathrm{d}^2}{\mathrm{d}\tau^2} \left(2K_x - k_{\perp,1} \sin\theta \right)\big|_{\tau_0}$$
$$\simeq \left[-4 \frac{\mathrm{d}K}{\mathrm{d}\tau}\bigg|_{\tau_0} \left(\frac{\mathrm{d}\theta_m}{\mathrm{d}\tau}\bigg|_{\tau_0} + \frac{\mathrm{d}\theta}{\mathrm{d}\tau}\bigg|_{\tau_0} \right) - 2K_0 \frac{\mathrm{d}^2\theta_m}{\mathrm{d}\tau^2}\bigg|_{\tau_0} \right] (\tau - \tau_0)^2 \tag{212}$$
$$\sim \frac{1}{L},$$

where we have used equation (141), and equation (209) to write $k_{\perp,1} \simeq -2K_0$. Taking into account all these considerations, and recalling that $k_{\perp,2} \sim 1/W$, we now Taylor expand the exponentially decaying piece, as well as the large phase piece, keeping terms

of order unity

$$-\frac{1}{4}(2K_x - k_{\perp,1}\sin\theta)^2 M_{xx}^{-1} - \frac{1}{2}k_{\perp,2}(2K_x - k_{\perp,1}\sin\theta)M_{xy}^{-1} - \frac{1}{4}k_{\perp,2}^2 M_{yy}^{-1}$$

$$+ 2s + k_{\perp,1}\int_0^\tau g(\tau')\cos\theta(\tau')\,\mathrm{d}\tau'$$

$$\simeq -\frac{1}{4}k_{\perp,2}^2 M_{yy,0}^{-1} + 2s_0 + k_{\perp,1}\int_0^{\tau_0} g(\tau')\cos\theta(\tau')\,\mathrm{d}\tau' \tag{213}$$

$$+ \left(k_{\perp,2}K_0\frac{\mathrm{d}\theta_m}{\mathrm{d}\tau}\Big|_{\tau_0} M_{xy,0}^{-1} + 2K_0 g_0 + k_{\perp,1}g_0\right)(\tau - \tau_0)$$

$$+ \left[g_0\frac{\mathrm{d}K}{\mathrm{d}\tau}\Big|_{\tau_0} - K_0^2\left(\frac{\mathrm{d}\theta_m}{\mathrm{d}\tau}\Big|_{\tau_0}\right)^2 M_{xx,0}^{-1}\right](\tau - \tau_0)^2.$$

To make the equations more manageable, we use the shorthand

$$G_0(k_{\perp,1}, k_{\perp,2}) = \left[g_0\frac{\mathrm{d}K}{\mathrm{d}\tau}\Big|_{\tau_0} - K_0^2\left(\frac{\mathrm{d}\theta_m}{\mathrm{d}\tau}\Big|_{\tau_0}\right)^2 M_{xx,0}^{-1}\right]^{-1}. \tag{214}$$

We now proceed to solve the Gaussian integral in τ to get

$$\tilde{A}_r = -\frac{\Omega A_{ant}g_{ant}\hat{\mathbf{e}}_{ant}\cdot\hat{\mathbf{e}}_{ant}}{2c}\int\left[\frac{\det[\mathrm{Im}(\boldsymbol{\Psi}_{w,0})]}{\det(\boldsymbol{M}_{w,0})}\right]^{\frac{1}{2}}\exp(2\mathrm{i}\phi_{G,0})$$

$$\times \frac{\delta\tilde{n}_{e,0}}{n_{e,0}}\,\hat{\mathbf{e}}_0^*\cdot(\boldsymbol{\epsilon}_{eq,0} - \mathbf{1})\cdot\hat{\mathbf{e}}_0\,\exp\left(2\mathrm{i}s_0 + \mathrm{i}k_{\perp,1}\int_0^{\tau_0} g(\tau')\cos\theta(\tau')\,\mathrm{d}\tau'\right) \tag{215}$$

$$\times \exp\left[-\frac{\mathrm{i}}{4}\left(k_{\perp,2}K_0\frac{\mathrm{d}\theta_m}{\mathrm{d}\tau}\Big|_{\tau_0} M_{xy,0}^{-1} + 2K_0 g_0 + k_{\perp,1}g_0\right)^2 G_0\right]$$

$$\times (\pi\mathrm{i}G_0)^{\frac{1}{2}}\exp\left[-\frac{\mathrm{i}}{4}k_{\perp,2}^2 M_{yy,0}^{-1}\right]\,\mathrm{d}k_{\perp,1}\,\mathrm{d}k_{\perp,2}.$$

Here $\mathrm{Re}\left(\sqrt{\pi\mathrm{i}G_0}\right) \geq 0$ as per standard contour integration methods, and the density fluctuations are evaluated at

$$\delta\tilde{n}_{e,0}(k_{\perp,1}, k_{\perp,2}, \omega) = \delta\tilde{n}_e\left(k_{\perp,1}, k_{\perp,2}, -\int_0^{\tau_0} g(\tau')\sin\theta(\tau')\,\mathrm{d}\tau', \omega\right). \tag{216}$$

In principle, the mismatch could be zero at more than one point along the ray. In that case, the total backscattered signal is the sum of the backscattered signal of each of those points. In the interests of simplicity, we will not discuss this further in this paper.

Before we continue further, we first show that in the appropriate limit, the *large mismatch angle* and *small mismatch angle* orderings give the same result. Showing that the backscattered amplitudes in these orderings match is challenging due to the large phase term $k_{\perp,1}\int_0^\tau g(\tau')\cos\theta(\tau')\mathrm{d}\tau'$. Instead, it is easier to show that the backscattered powers match. To do this, we perform subsidiary expansions of both the *small mismatch angle* and *large mismatch angle* expressions. For the former, we take the mismatch to be large and perform a Taylor expansion of $k_{\perp,1}$ about $-2K_0$. For the *large mismatch angle* ordering, we make the mismatch less than order unity $\theta_m \ll 1$ throughout the beam path. In this intermediate range,

$$1 \gg \theta_m \gg \frac{\lambda}{W}, \tag{217}$$

both models should be applicable and must coincide.

In such an endeavour, the backscattered power of the *small mismatch angle* ordering is given by equation (177); that of the *large mismatch angle* ordering can be determined by applying the same methods used in Section 7, giving

$$
\frac{p_r}{P_{ant}} = \frac{1}{4}\frac{\Omega^2}{c^2}g_{ant}^2\left|\hat{\mathbf{e}}_{ant}\cdot\hat{\mathbf{e}}_{ant}\right|^2\pi\int\frac{\det\left[\mathrm{Im}\left(\boldsymbol{\Psi}_{w,0}\right)\right]}{\left|\det\left(\boldsymbol{M}_{w,0}\right)\right|}\left|\hat{\mathbf{e}}_0^*\cdot\left(\boldsymbol{\epsilon}_{eq,0}-\mathbf{1}\right)\cdot\hat{\mathbf{e}}_0\right|^2
$$

$$
\times\frac{1}{|G_0|}\exp\left\{\frac{1}{2}\,\mathrm{Im}\left[\left(k_{\perp,2}K_0\frac{\mathrm{d}\theta_m}{\mathrm{d}\tau}\bigg|_{\tau_0}M_{xy,0}^{-1}+2K_0g_0+k_{\perp,1}g_0\right)^2G_0\right]\right\} \tag{218}
$$

$$
\times\exp\left[\frac{1}{2}\mathrm{Im}\left(M_{yy,0}^{-1}\right)k_{\perp,2}^2\right]\frac{\left\langle\delta n_{e,0}^2(t)\right\rangle_t}{n_{e,0}^2}\widetilde{C}_0(k_{\perp,1},k_{\perp,2},\omega)\,\mathrm{d}k_{\perp,1}\,\mathrm{d}k_{\perp,2}.
$$

We now perform the subsidiary expansion of the *large mismatch angle* ordering. We begin by expanding G_0 — see equation (214) — to get

$$
G_0 = \left(\frac{\mathrm{d}K}{\mathrm{d}\tau}\bigg|_{\tau_0}g_0-K_0^2\left(\frac{\mathrm{d}\theta_m}{\mathrm{d}\tau}\bigg|_{\tau_0}\right)^2M_{xx,0}^{-1}\right)^{-1}
$$

$$
\simeq\left(\frac{\mathrm{d}K}{\mathrm{d}\tau}\bigg|_{\tau_0}g_0\right)^{-1}+K_0^2\left(\frac{\mathrm{d}\theta_m}{\mathrm{d}\tau}\bigg|_{\tau_0}\right)^2M_{xx,0}^{-1}\left(\frac{\mathrm{d}K}{\mathrm{d}\tau}\bigg|_{\tau_0}g_0\right)^{-2}, \tag{219}
$$

where we have kept terms up to order unity for the exponential. When it comes to the $|G_0|^{-1}$ outside the exponential, see equation (218), we only need to keep the zeroth order term, ignoring the first order correction. It is worth noting that we looked at several MAST shots, and the difference between the full expression and the expansion in equation (219) was negligible, that is, the MAST DBS seems to be in the intermediate regime where the *small mismatch angle* and *large mismatch angle* orderings are both valid. We introduce the notation

$$
\Delta k_{\perp,1} = k_{\perp,1}-k_{\perp,1,0}=k_{\perp,1}+2K_0, \tag{220}
$$

where we have used the Bragg condition at the zero-mismatch point. We see that the signal decays exponentially with $\Delta k_{\perp,1}$ and hence we order the most quickly decaying term to be of order one

$$
-\mathrm{Im}\left[\left(\Delta k_{\perp,1}\right)^2K_0^2\left(\frac{\mathrm{d}\theta_m}{\mathrm{d}\tau}\bigg|_{\tau_0}\right)^2M_{xx,0}^{-1}\left(\frac{\mathrm{d}K}{\mathrm{d}\tau}\bigg|_{\tau_0}\right)^{-2}\right]\sim 1. \tag{221}
$$

This gives us the size of $\Delta k_{\perp,1}$

$$
\Delta k_{\perp,1}\sim\frac{1}{\theta_m W}, \tag{222}
$$

which makes physical sense, since one would expect better localisation at τ_0 with larger mismatch along the ray. In the *large mismatch angle* subsection, we had $\theta_m\sim 1$, which gives $\Delta k_{\perp,1}\sim 1/W$, justifying equation (209). We now take $\theta_m\ll 1$ and expand the

exponentially decaying piece from equation (215), using equations (219), (220), and (222), getting

$$\frac{1}{2}\text{Im}\left[\left(k_{\perp,2}K_0\frac{\mathrm{d}\theta_m}{\mathrm{d}\tau}\bigg|_{\tau_0}M_{xy,0}^{-1} + g_0\Delta k_{\perp,1}\right)^2\left(g_0\frac{\mathrm{d}K}{\mathrm{d}\tau}\bigg|_{\tau_0} - K_0^2\left(\frac{\mathrm{d}\theta_m}{\mathrm{d}\tau}\bigg|_{\tau_0}\right)^2 M_{xx,0}^{-1}\right)^{-1}\right]$$

$$+ \frac{1}{2}\text{Im}\left(M_{yy,0}^{-1}\right)k_{\perp,2}^2$$

$$\simeq \frac{1}{2}\Delta k_{\perp,1}^2 K_0^2\left(\frac{\mathrm{d}\theta_m}{\mathrm{d}\tau}\bigg|_{\tau_0}\right)^2\left(\frac{\mathrm{d}K}{\mathrm{d}\tau}\bigg|_{\tau_0}\right)^{-2}\text{Im}\left(M_{xx,0}^{-1}\right)$$

$$+ k_{\perp,2}\Delta k_{\perp,1}K_0\frac{\mathrm{d}\theta_m}{\mathrm{d}\tau}\bigg|_{\tau_0}\left(\frac{\mathrm{d}K}{\mathrm{d}\tau}\bigg|_{\tau_0}\right)^{-1}\text{Im}\left(M_{xy,0}^{-1}\right) + \frac{1}{2}k_{\perp,2}^2\text{Im}\left(M_{yy,0}^{-1}\right),$$

$$(223)$$

where we have neglected terms that are small.

We proceed to perform a subsidiary expansion of the *small mismatch angle* ordering, equation (153), in the limit $\theta_m \gg \lambda/W$. To determine the relationship between τ_μ and $k_{\perp,1}$ around τ_0, we differentiate equation (148) with respect to τ, at $\tau = \tau_0$,

$$\frac{\mathrm{d}\tau_\mu}{\mathrm{d}k_{\perp,1}}\bigg|_{\perp,1,0} = -\left(2\frac{\mathrm{d}K}{\mathrm{d}\tau}\bigg|_{\tau_0}\right)^{-1}, \tag{224}$$

which we then use in our expansion in $k_{\perp,1}$ of the exponential decaying piece in equation (177). Together with equations (220), and (222), this gives us

$$2\text{Im}\left(M_{xx,\mu}^{-1}\right)K_\mu^2\theta_{m,\mu}^2 - 2\text{Im}\left(M_{xy,\mu}^{-1}\right)K_\mu\theta_{m,\mu}k_{\perp,2} + \frac{1}{2}\text{Im}\left(M_{yy,\mu}^{-1}\right)k_{\perp,2}^2$$

$$= \frac{1}{2}\Delta k_{\perp,1}^2 K_0^2\left(\frac{\mathrm{d}\theta_m}{\mathrm{d}\tau}\bigg|_{\tau_0}\right)^2\left(\frac{\mathrm{d}K}{\mathrm{d}\tau}\bigg|_{\tau_0}\right)^{-2}\text{Im}\left(M_{xx,0}^{-1}\right)$$

$$+ k_{\perp,2}\Delta k_{\perp,1}K_0\frac{\mathrm{d}\theta_m}{\mathrm{d}\tau}\bigg|_{\tau_0}\left(\frac{\mathrm{d}K}{\mathrm{d}\tau}\bigg|_{\tau_0}\right)^{-1}\text{Im}\left(M_{xy,0}^{-1}\right) + \frac{1}{2}k_{\perp,2}^2\text{Im}\left(M_{yy,0}^{-1}\right),$$

$$(225)$$

where we have neglected terms which are small and recalled that the Bragg condition is exactly met at τ_0. We note that equations (223) and (225) match, showing that the exponential decay is indeed the same in both orderings. As such, we can use the *small mismatch angle* formulation and the associated results, such as equations (180) and (196), even for moderate *large mismatch angle* situations. Recall that the MAST DBS seems to be in this regime. As we explain below equation (219), for the few MAST shots that we have reviewed, the difference between the exact and approximate expressions of G_0 was negligble.

12. Discussion

Having presented the physical and quantitative insight our model sheds on localisation, wavenumber resolution, and mismatch attenuation, we now discuss how the various aspects of our model might come together and enable us to better understand DBS as a whole.

A point of considerable interest is that the optimisations of both $k_{\perp,2}$ wavenumber resolution and mismatch attenuation have opposite requirements. To gain intuition, we consider the simplified case for $M_{xy,\mu} = 0$, where the associated mismatch attenuation is given in equation (204) and the $k_{\perp,2}$ wavenumber resolution in equation (202). When designing a DBS system, one would want to maximise resolution (minimise $\Delta k_{\mu,2}$) and minimise mismatch attenuation (maximise $\Delta\theta_{m,\mu}$). Hence, to optimise both simultaneously, one would need an elliptical beam.

We examine how the $-\text{Im}\,(1/\Psi_{\alpha\alpha})$ piece behaves in vacuum and answer the question of whether the wavenumber resolution $\Delta k_{\mu,2}$ and the mismatch attenuation $\Delta\theta_{m,\mu}$ are larger at or far from the beam waist. The answer is not obvious. Consider the following example. The intuitive reason why the backscattered power is nonzero when there is a mismatch is because there is a spread in $\mathbf{K}$ due to the width and curvature of the beam. Specifically, we see that only the width and curvature in one direction matters, $\Psi_{xx,\mu}$. To maximise the aforementioned spread, we want very curved wavefronts (small $R_{x,\mu}$) and narrow beams (small $W_{x,\mu}$). The dependence on beam curvature means we want to be far from the waist, while the dependence on width means we want to be at the waist. Conversely, the wavenumber resolution, which depends on $\Psi_{yy,\mu}$, benefits from the low curvature near the waist, and from the larger beam widths far from the waist.

In fact, in vacuum, it can be shown that a elliptical beam satisfies

$$-\text{Im}\left(\frac{1}{\Psi_{\alpha\alpha}}\right) = \frac{2}{W_{\alpha,waist}^2} \tag{226}$$

at all points along the beam. Here, $\Psi_{\alpha\alpha}$ are the eigenvalues of $\boldsymbol{\Psi}_w$. Hence, it does not matter where we are along the beam nor where is the beam waist, the only important thing is the beam waist's width. We would want a narrower waist to optimise wavenumber resolution, and a wider waist to optimise mismatch attenuation. In order to reconcile these seemingly contradictory requirements, one could imagine using an elliptical Gaussian beam to simultaneously optimise widths in the relevant directions.

Despite the intuition that considering beams in vacuum may give us, the evolution of $\boldsymbol{\Psi}_w$ is ultimately more complicated in a plasma. This is one reason why using beam tracing is important. In Figure 18, we see that the beam in the plasma can indeed be quite different from what one would expect from vacuum propagation; the beam curvature goes to zero at two points, and neither of them are where the beam widths are at a minimum. Thus, the notion of a beam waist, where the widths are at a minimum and the wavefront curvatures are zero simultaneously, is not properly achieved to begin with. This insight is a demonstration of the strength of our model.

13. Conclusion

We have successfully derived the full analytical form of the linear backscattered signal from DBS measurements by combining the beam-tracing equations with the reciprocity theorem in general geometry. This is the first analytical model to self-consistently account for signal localisation (spatial resolution), wavenumber resolution,
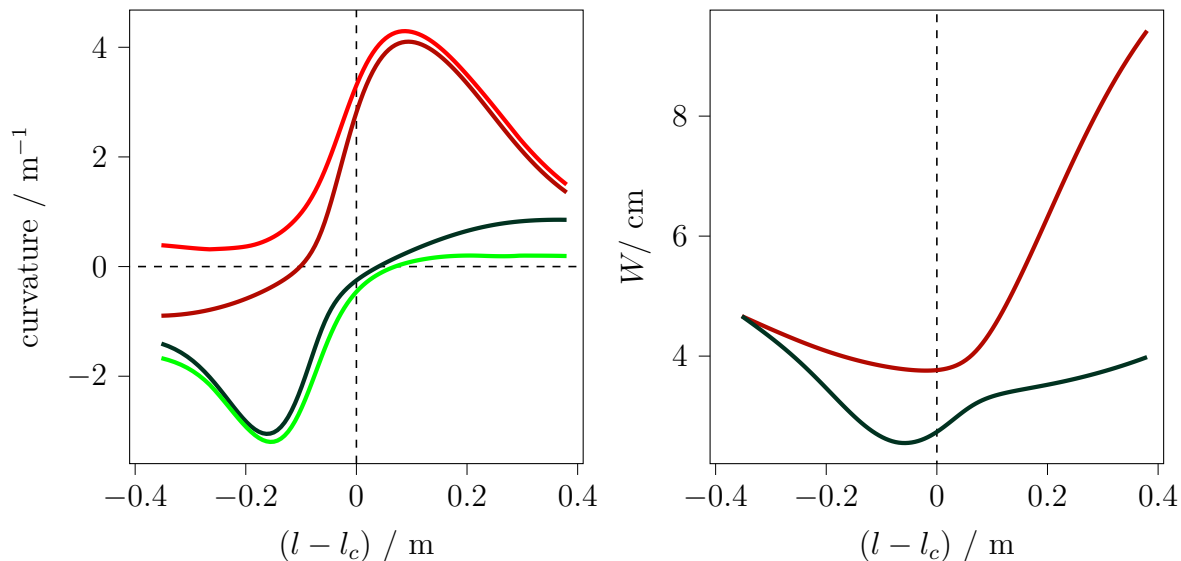
Figure 18: MAST test scenario, with launch parameters $R_{b,x} = R_{b,y} = -1.79$m, $W_x = W_y = 9.47$cm. Evolution of curvatures $1/R_b$ (left, dark green and dark red, the two colours corresponding to two different directions) and widths (right) along the beam, calculated from the non-zero eigenvalues of the real and imaginary parts of $\boldsymbol{\Psi}_w$ respectively. The effective curvatures $1/R_{b,M}$ (left, bright green and bright red) are calculated from the non-zero eigenvalues of the real part of $\boldsymbol{M}_w$. We plot the curvatures $1/R_b$ and $1/R_{b,M}$ rather than the radii of curvature R_b and $R_{b,M}$ to avoid a divergence. Note that the directions of the eigenvectors corresponding to W, $1/R_b$, and $1/R_{b,M}$ are not aligned with one another (nor with $\hat{\mathbf{x}}$ or $\hat{\mathbf{y}}$) in general. Even at the point the beam enters the plasma (when these plots start), the principal curvatures are not the equal to each other, despite us launching a circular beam, because we have applied the vacuum-plasma boundary conditions, as described in Appendix C. Recall that $l - l_c$ is the distance along the central ray from the cut-off location.

and mismatch attenuation, given in equations (197), (182), and (181), respectively. In particular, we find that it is the curvature of the field lines and the magnetic shear, rather than the curvature of the cut-off surface, that is important for the calculation of these quantities. This is a result of the magnetic curvature and shear modifying the effective beam curvature, as shown in equations (155) and (156). We also show that the localisation and one of the two components of wavenumber resolution are inextricably intertwined, via the Bragg condition.

To calculate these quantities, one needs to solve the beam tracing equations (24), (25), and (27), evolving the probe beam as it propagates through the plasma. Beam tracing requires the following additional input parameters: the equilibrium density, magnetic field, and potentially temperature. Beam-tracing simulations are swift, which makes the beam model suitable for intershot analysis of DBS data and for large parameter sweeps. Since beam tracing solves for the next-order corrections to ray

tracing, it should not be too complicated to upgrade existing ray-tracing codes to solve for the beam properties and use them in post-processing for our model.

Using our model, one can now correct for the effect of mismatch, since we have found, for the first time, the quantitative analytical dependence of attenuation on the mismatch angle. This is vital for DBS measurements of spherical tokamak plasmas, where the pitch angle is large and varies both spatially and temporally, making optimisation for all channels at all times impossible. Furthermore, we find analytical evidence that mismatch attenuation is also important in conventional tokamaks, especially for high wavenumber measurements. Being able to calculate the quantitative effect of mismatch enables one to relax the criterion that the probe wavevector has to be exactly perpendicular to the magnetic field. As long as the mismatch angle is not so large that the signal is completely attenuated, the mismatch attenuation can be quantitatively corrected with our model. This allows one to run DBS studies with fewer repeated shots by optimising the launch angles such that there is useful data on as many channels as possible, to glean new physical insights from legacy data, and to potentially design simpler DBS systems with smaller ranges of launch angles or without 2D steering.

We derived our model in two limits: the small-mismatch and large-mismatch orderings. Conventionally, DBS is operated in the small-mismatch regime, where the signal does indeed come from around the cut-off region. In the large-mismatch regime, we focus on the specific case where the mismatch angle is zero at at least one point along the beam path, and find that the signal comes from that point, which in general will not be at the cut-off. This provides an alternative method of getting a localised signal, via a different physical mechanism. We show that in cases where the mismatch angle is moderately large, the small-mismatch and large-mismatch formulations give the same results, see Section 11. In such situations, the same formulation can be used for both cases.

Finally, our model provides the basis for synthetic diagnostics, a quick and realistic physical method to calculate the expected DBS signal given particular realisations of turbulence from gyrokinetic simulations. Depending on how much physics one intends to keep, one could use equation (196), (180), or even (127).

Acknowledgments

Appendix A. Derivation of beam tracing

In beam tracing, we seek to find the electric field of the Gaussian probe beam as it propagates through the plasma. Our derivation is an alternative to that of Pereverzev's [48, 49, 50, 51]; the results are equivalent, but ours is specific to our choice of coordinates, and is thus more convenient for our work on Doppler backscattering. Unlike Pereverzev, our derivation does not require some of the intermediate steps in Section III of his work [51].

By directly using the ansatz for the probe beam's electric field, equation (10), and the expansion of its amplitude in equation (19), we get

$$\mathbf{E} = \left[\mathbf{A}^{(0)}(\tau) + \mathbf{A}^{(1)}(\tau, \mathbf{w}) + \mathbf{A}^{(2)}(\tau, \mathbf{w}) \right] \exp\left(i\psi\right). \tag{A.1}$$

We take $\mathbf{A}^{(1)}$ and $\mathbf{A}^{(2)}$, the higher order amplitudes, to be linear and bilinear in $\mathbf{w}$, that is

$$\mathbf{A}^{(1)}(\tau, \mathbf{w}) = \mathbf{w} \cdot \nabla_w \mathbf{A}^{(1)}(\tau), \tag{A.2}$$

and

$$\mathbf{A}^{(2)}(\tau, \mathbf{w}) = \frac{1}{2} \mathbf{w}\mathbf{w} : \nabla_w \nabla_w \mathbf{A}^{(2)}(\tau) + \mathbf{A}^{(2)}(\tau, \mathbf{w} = 0). \tag{A.3}$$

This simplified dependence on the intermediate length scale $\mathbf{w}$ allows us to neglect $\nabla\nabla\mathbf{A}^{(1)}$ and $\nabla\nabla\nabla\mathbf{A}^{(2)}$ compared to $\nabla\nabla\mathbf{A}^{(0)}(\tau)$ and $\nabla\nabla\nabla\mathbf{A}^{(0)}(\tau)$, respectively.

Since we are looking for a solution to equation (4), we need to evaluate the derivatives of $\mathbf{E}$,

$$\frac{\partial^2 \mathbf{E}}{\partial r_\mu \partial r_\nu} = \left[- \underbrace{\frac{\partial\psi}{\partial r_\mu}\frac{\partial\psi}{\partial r_\nu}\mathbf{A}}_{\sim \lambda^{-2}\mathbf{A}} + \underbrace{i\frac{\partial\psi}{\partial r_\mu}\frac{\partial\mathbf{A}}{\partial r_\nu} + i\frac{\partial^2\psi}{\partial r_\mu \partial r_\nu}\mathbf{A} + i\frac{\partial\mathbf{A}}{\partial r_\mu}\frac{\partial\psi}{\partial r_\nu}}_{\sim \lambda^{-1}L^{-1}\mathbf{A}} + \underbrace{\frac{\partial^2\mathbf{A}}{\partial r_\mu \partial r_\nu}}_{\sim L^{-2}\mathbf{A}} \right] \exp(i\psi). \tag{A.4}$$

The first order derivatives of ψ, where ψ is given in equation (11), are

$$\nabla\psi = \frac{ds}{d\tau}\nabla\tau + \mathbf{K}_w + \frac{d\mathbf{K}_w}{d\tau} \cdot \mathbf{w}\nabla\tau + \boldsymbol{\Psi}_w \cdot \mathbf{w} + \frac{1}{2}\mathbf{w} \cdot \frac{d\boldsymbol{\Psi}_w}{d\tau} \cdot \mathbf{w}\nabla\tau. \tag{A.5}$$

Here we have used $\mathbf{w} = [\mathbf{r} - \mathbf{q}(\tau)]_w$, and noted that since $d\mathbf{q}/d\tau = \mathbf{g}$, we get $\mathbf{K}_w \cdot d\mathbf{q}/d\tau = 0$ and $d\mathbf{q}/d\tau \cdot \boldsymbol{\Psi}_w \cdot \mathbf{w} = 0$. In order to proceed, we need to know the form of $\nabla\tau$. We do this by using the reciprocal vector

$$\nabla\tau = \left(\frac{\partial\mathbf{r}}{\partial w_x} \times \frac{\partial\mathbf{r}}{\partial w_y} \right) \left[\frac{\partial\mathbf{r}}{\partial\tau} \cdot \left(\frac{\partial\mathbf{r}}{\partial w_x} \times \frac{\partial\mathbf{r}}{\partial w_y} \right) \right]^{-1}. \tag{A.6}$$

Using $d\hat{\mathbf{x}}/d\tau \cdot \hat{\mathbf{g}} = -\hat{\mathbf{x}} \cdot d\hat{\mathbf{g}}/d\tau$ and $d\hat{\mathbf{y}}/d\tau \cdot \hat{\mathbf{g}} = -\hat{\mathbf{y}} \cdot d\hat{\mathbf{g}}/d\tau$, we find that

$$\nabla\tau = \hat{\mathbf{g}} \left[g - \mathbf{w} \cdot \frac{d\hat{\mathbf{g}}}{d\tau} \right]^{-1}. \tag{A.7}$$

Note that $g^{-1}d\hat{\mathbf{g}}/d\tau = d\hat{\mathbf{g}}/dl = \boldsymbol{\kappa}$, where $\boldsymbol{\kappa} \sim L^{-1}$ is the curvature of the central ray and l is arc length along the ray. This ray curvature should not be confused with the wavefront curvature. Using the ray curvature $\boldsymbol{\kappa}$ and equation (A.7),

$$\nabla\tau = \frac{\hat{\mathbf{g}}}{g(1 - \boldsymbol{\kappa}\cdot\mathbf{w})}. \tag{A.8}$$

We note that $\boldsymbol{\kappa}\cdot\mathbf{w} \sim W/L \ll 1$ and that we can re-express $\nabla\tau$ as

$$\nabla\tau = \frac{\hat{\mathbf{g}}}{g}[1 + \boldsymbol{\kappa}\cdot\mathbf{w} + (\boldsymbol{\kappa}\cdot\mathbf{w})^2 + \ldots]. \tag{A.9}$$

Substituting equation (A.9) into the equation for $\nabla\psi$, equation (A.5), and separating the terms by order, we get

$$\nabla\psi = \underbrace{(\nabla\psi)^{(0)}}_{\sim 1/\lambda} + \underbrace{(\nabla\psi)^{(1)}}_{\sim 1/W} + \underbrace{(\nabla\psi)^{(2)}}_{\sim 1/L} + \ldots, \tag{A.10}$$

where

$$(\nabla\psi)^{(0)} = K_g\hat{\mathbf{g}} + \mathbf{K}_w = \mathbf{K},$$

$$(\nabla\psi)^{(1)} = K_g\hat{\mathbf{g}}(\boldsymbol{\kappa}\cdot\mathbf{w}) + \frac{\hat{\mathbf{g}}}{g}\frac{d\mathbf{K}_w}{d\tau}\cdot\mathbf{w} + \boldsymbol{\Psi}_w\cdot\mathbf{w},$$

$$\tag{A.11}$$

and

$$(\nabla\psi)^{(2)} = K_g\hat{\mathbf{g}}(\boldsymbol{\kappa}\cdot\mathbf{w})^2 + \frac{\hat{\mathbf{g}}}{g}(\boldsymbol{\kappa}\cdot\mathbf{w})\frac{d\mathbf{K}_w}{d\tau}\cdot\mathbf{w} + \frac{1}{2}\frac{\hat{\mathbf{g}}}{g}\mathbf{w}\cdot\frac{d\boldsymbol{\Psi}_w}{d\tau}\cdot\mathbf{w}.$$

Here we have defined the wavenumber parallel to the central ray to be $K_g = g^{-1}ds/d\tau = ds/dl$, and the total wavevector to be $\mathbf{K} = K_g\hat{\mathbf{g}} + \mathbf{K}_w$.

We will need $\nabla\nabla\psi$ only to lowest order. Note that the gradient of ψ can only have two possible length scales, W and L. Consequently, to evaluate $\nabla\nabla\psi$ to leading order, we need to find the gradients of both $(\nabla\psi)^{(0)}$ and $(\nabla\psi)^{(1)}$, but not $(\nabla\psi)^{(2)}$. Hence, we have

$$\nabla\nabla\psi \simeq \nabla\left[\mathbf{K} + K_g\hat{\mathbf{g}}(\boldsymbol{\kappa}\cdot\mathbf{w}) + \frac{\hat{\mathbf{g}}}{g}\frac{d\mathbf{K}_w}{d\tau}\cdot\mathbf{w} + \boldsymbol{\Psi}_w\cdot\mathbf{w}\right]$$

$$\simeq \boldsymbol{\Psi}_w + \frac{\hat{\mathbf{g}}}{g}\frac{d\mathbf{K}}{d\tau} + K_g\boldsymbol{\kappa}\hat{\mathbf{g}} + \left(\frac{d\mathbf{K}_w}{d\tau}\right)_w\frac{\hat{\mathbf{g}}}{g}, \tag{A.12}$$

where all the terms are of order $(\lambda L)^{-1} \sim W^{-2}$.

We substitute equation (10) into equation (4), and remember the sizes of various terms as shown in equation (A.4). We perform a Taylor expansion of the dielectric tensor,

$$\boldsymbol{\epsilon}(\mathbf{r}) = \boldsymbol{\epsilon}(\mathbf{q} + \mathbf{w}) \simeq \boldsymbol{\epsilon}(\mathbf{q}) + \mathbf{w}\cdot\nabla\boldsymbol{\epsilon}(\mathbf{q}) + \frac{1}{2}\mathbf{ww} : \nabla\nabla\boldsymbol{\epsilon}(\mathbf{q}). \tag{A.13}$$

Appendix A.1. Zeroth order

To lowest order $\nabla\psi \simeq K_g\hat{\mathbf{g}} + \mathbf{K}_w = \mathbf{K} \sim \lambda^{-1}$ and $\mathbf{A} \simeq \mathbf{A}^{(0)}$, giving

$$\left[\frac{c^2}{\Omega^2}(\mathbf{KK} - K^2\mathbf{1}) + \boldsymbol{\epsilon}\right]\cdot\mathbf{A}^{(0)} = 0. \tag{A.14}$$

We do not need to keep higher order terms because $(c^2/\Omega^2)\mathbf{K}\times(\mathbf{K}\times\mathbf{E}) \sim (c^2K^2/\Omega^2)E \sim N^2E$ and $\boldsymbol{\epsilon}\cdot\mathbf{E} \sim N^2E$, where N is the refractive index. For convenience, we use the notation

$$\boldsymbol{D}(\mathbf{q},\mathbf{K}) = \frac{c^2}{\Omega^2}(\mathbf{KK}-K^2\mathbf{1})+\boldsymbol{\epsilon}(\mathbf{q}), \tag{A.15}$$

leading to

$$\boldsymbol{D}\cdot\mathbf{A}^{(0)} = 0. \tag{A.16}$$

Since $\boldsymbol{D}$ is Hermitian, it can be diagonalised — there exist three vectors $\hat{\mathbf{e}}(\mathbf{r},\mathbf{K})$ such that $\boldsymbol{D}\cdot\hat{\mathbf{e}} = H\hat{\mathbf{e}}$. To solve equation (A.15), $K_g(\tau)$ must be such that one of the three eigenvalues $H(\mathbf{q}(\tau),\mathbf{K}(\tau))$ vanishes, that is, $H=0$ will give $K_g(\tau)$ once $\mathbf{K}_w(\tau)$ and $\mathbf{q}(\tau)$ are known. To obtain the equations for $\mathbf{K}_w(\tau)$ and $\mathbf{q}(\tau)$, we need to go to first order in the expansion $\lambda/W \sim W/L$.

In general, only one of the eigenvalues H goes to zero. The vector $\mathbf{A}^{(0)}$ has to be parallel to the $\hat{\mathbf{e}}$ that corresponds to $H=0$, $\mathbf{A}^{(0)} = A^{(0)}\hat{\mathbf{e}}$.

Appendix A.2. First order

In this subsection, we get contributions to equation (4) that are of first order in $\lambda/W \sim W/L \ll 1$. The terms come from $\nabla\psi$ in equation (A.5), the next order correction to the amplitude $\mathbf{A}^{(1)}$, and the expansion of $\boldsymbol{\epsilon}$ in equation (A.13),

$$(\nabla\psi)^{(1)}\cdot\nabla_K\boldsymbol{D}\cdot\hat{\mathbf{e}}A^{(0)} + \boldsymbol{D}\cdot\mathbf{A}^{(1)} + \mathbf{w}\cdot\nabla\boldsymbol{\epsilon}(\mathbf{q})\cdot\hat{\mathbf{e}}A^{(0)} = 0. \tag{A.17}$$

Here we have used

$$\begin{aligned}
\frac{\partial D_{\alpha\beta}}{\partial K_\mu} &= \frac{c^2}{\Omega^2}\frac{\partial}{\partial K_\mu}(K_\alpha K_\beta - K^2\delta_{\alpha\beta}) \\
&= \frac{c^2}{\Omega^2}\left[K_\beta\delta_{\alpha\mu} + K_\alpha\delta_{\beta\mu} - 2K_\mu\delta_{\alpha\beta}\right],
\end{aligned} \tag{A.18}$$

where $\delta_{..}$ are Kronecker deltas. Substituting the expression for $(\nabla\psi)^{(1)}$ given in equation (A.11) and realising that $\nabla\boldsymbol{\epsilon} = \nabla\boldsymbol{D}$, we get

$$\begin{aligned}
&\left(K_g\hat{\mathbf{g}}(\boldsymbol{\kappa}\cdot\mathbf{w}) + \frac{\hat{\mathbf{g}}}{g}\frac{d\mathbf{K}_w}{d\tau}\cdot\mathbf{w} + \boldsymbol{\Psi}_w\cdot\mathbf{w}\right)\cdot\nabla_K\boldsymbol{D}\cdot\hat{\mathbf{e}}A^{(0)} \\
&+ \boldsymbol{D}\cdot\mathbf{A}^{(1)} + \mathbf{w}\cdot\nabla\boldsymbol{D}\cdot\hat{\mathbf{e}}A^{(0)} = 0.
\end{aligned} \tag{A.19}$$

Since $\boldsymbol{D}$ is Hermitian, $\hat{\mathbf{e}}^*\cdot\boldsymbol{D} = 0$. Thus, we multiply equation (A.19) by $\hat{\mathbf{e}}^*$ to eliminate $\boldsymbol{D}\cdot\mathbf{A}^{(1)}$,

$$\hat{\mathbf{e}}^*\cdot\left[\left(K_g\hat{\mathbf{g}}(\boldsymbol{\kappa}\cdot\mathbf{w}) + \frac{\hat{\mathbf{g}}}{g}\frac{d\mathbf{K}_w}{d\tau}\cdot\mathbf{w} + \boldsymbol{\Psi}_w\cdot\mathbf{w}\right)\cdot\nabla_K\boldsymbol{D} + \mathbf{w}\cdot\nabla\boldsymbol{\epsilon}(\mathbf{q})\right]\cdot\hat{\mathbf{e}} = 0. \tag{A.20}$$

This equation can be simplified by using derivatives of the dispersion relation $H = \hat{\mathbf{e}}^*\cdot\boldsymbol{D}\cdot\hat{\mathbf{e}}$. Since $\boldsymbol{D}\cdot\hat{\mathbf{e}} = 0 = \hat{\mathbf{e}}^*\cdot\boldsymbol{D}$, we find that $\partial_\mu H = \hat{\mathbf{e}}^*\cdot\partial_\mu\boldsymbol{D}\cdot\hat{\mathbf{e}}$, where ∂_μ is shorthand for either $\partial/\partial K_\mu$ or $\partial/\partial r_\mu$. Hence, equation (A.19) can be rewritten as

$$\left(K_g\hat{\mathbf{g}}(\boldsymbol{\kappa}\cdot\mathbf{w}) + \frac{\hat{\mathbf{g}}}{g}\frac{d\mathbf{K}_w}{d\tau}\cdot\mathbf{w} + \boldsymbol{\Psi}_w\cdot\mathbf{w}\right)\cdot\nabla_K H + \mathbf{w}\cdot\nabla H = 0. \tag{A.21}$$

We note that the curvature $\boldsymbol{\kappa}$ is always in the same plane as $\mathbf{w}$ (since it is always normal to the group velocity), and so is the matrix $\boldsymbol{\Psi}_w$ (since we have chosen it to be so). Since equation (A.20) is satisfied for all possible values of $\mathbf{w}$, we obtain

$$\left[K_g\boldsymbol{\kappa} + \frac{1}{g}\left(\frac{\mathrm{d}\mathbf{K}_w}{\mathrm{d}\tau}\right)_w\right]\hat{\mathbf{g}}\cdot\nabla_K H + \boldsymbol{\Psi}_w\cdot\nabla_K H + \nabla_w H = 0. \tag{A.22}$$

Note that H is real and $\boldsymbol{\Psi}_w$ is complex. There are four equations at play here; there are two directions in the plane perpendicular to $\hat{\mathbf{g}}$, and since $\boldsymbol{\Psi}_w$ is complex, both the real and imaginary parts in either of these directions must be satisfied. Two of these equations are used to determine $\mathrm{d}\mathbf{K}_w/\mathrm{d}\tau$, and the other two are used to determine $\hat{\mathbf{g}}$, the direction of $\mathbf{g} = \mathrm{d}\mathbf{q}/\mathrm{d}\tau$. The magnitude of $\mathbf{g}$ is not determined by these equations, since we do not have enough of them; instead we choose it shortly. Since we want $\mathbf{K}$ to be real, we have to enforce $\mathrm{Im}(\boldsymbol{\Psi}_w)\cdot\nabla_K H = 0$, which will lead to $\nabla_K H \propto \hat{\mathbf{g}}$, since $\boldsymbol{\Psi}_w$ is perpendicular to the group velocity. This is the key step — we select the group velocity such that it is in the direction of the central ray, the only direction in which there is no decay of the electric field. Since $\hat{\mathbf{g}}$ is now a unit vector in the direction of $\nabla_K H$, we get

$$\left[K_g\boldsymbol{\kappa} + \frac{1}{g}\left(\frac{\mathrm{d}\mathbf{K}_w}{\mathrm{d}\tau}\right)_w\right]|\nabla_K H| = -\nabla_w H = -\nabla H + \hat{\mathbf{g}}\hat{\mathbf{g}}\cdot\nabla H. \tag{A.23}$$

We obtain $\hat{\mathbf{g}}\cdot\nabla H$ from taking the derivative of the equation for K_g, $H = 0$, with respect to τ. Since $\mathrm{d}H/\mathrm{d}\tau = 0$, we obtain

$$\frac{\mathrm{d}\mathbf{K}}{\mathrm{d}\tau}\cdot\nabla_K H + \frac{\mathrm{d}\mathbf{q}}{\mathrm{d}\tau}\cdot\nabla H = 0, \tag{A.24}$$

which can be rewritten as

$$\frac{1}{g}\frac{\mathrm{d}\mathbf{K}}{\mathrm{d}\tau}\cdot\nabla_K H = -\hat{\mathbf{g}}\cdot\nabla H. \tag{A.25}$$

Substituting equation (A.25) into equation (A.23), we get

$$\left[K_g\boldsymbol{\kappa} + \frac{1}{g}\left(\frac{\mathrm{d}\mathbf{K}_w}{\mathrm{d}\tau}\right)_w\right]|\nabla_K H| + \frac{\hat{\mathbf{g}}}{g}\frac{\mathrm{d}\mathbf{K}}{\mathrm{d}\tau}\cdot\hat{\mathbf{g}}|\nabla_K H| = -\nabla H. \tag{A.26}$$

We then note that

$$\left(\frac{\mathrm{d}\mathbf{K}}{\mathrm{d}\tau}\right)_w = \left(\frac{\mathrm{d}\mathbf{K}_w}{\mathrm{d}\tau}\right)_w + K_g\left(\frac{\mathrm{d}\hat{\mathbf{g}}}{\mathrm{d}\tau}\right)_w = \left(\frac{\mathrm{d}\mathbf{K}_w}{\mathrm{d}\tau}\right)_w + K_g g\boldsymbol{\kappa}. \tag{A.27}$$

Consequently, we get

$$\frac{|\nabla_K H|}{g}\frac{\mathrm{d}\mathbf{K}}{\mathrm{d}\tau} = -\nabla H. \tag{A.28}$$

We then choose $g = |\nabla_K H|$. This gives us

$$\frac{\mathrm{d}\mathbf{q}}{\mathrm{d}\tau} = g\hat{\mathbf{g}} = |\nabla_K H|\hat{\mathbf{g}} = \nabla_K H. \tag{A.29}$$

Hence, we have

$$\frac{\mathrm{d}\mathbf{K}}{\mathrm{d}\tau} = -\nabla H. \tag{A.30}$$

Note that we could have chosen any other prescription for g, and it would only have modified the definition of the free parameter τ. The choice $g = |\nabla_K H|$ emphasises the Hamiltonian character of the equations.

Finally, we can use equations (A.19) and (A.23) to solve for $\mathbf{A}^{(1)}$,

$$\boldsymbol{D} \cdot \mathbf{A}^{(1)} = -\left[\left(-\frac{\hat{\mathbf{g}}\mathbf{w} \cdot \nabla H}{g} + \mathbf{w} \cdot \boldsymbol{\Psi}_w\right) \cdot \nabla_K \boldsymbol{D} \cdot \hat{\mathbf{e}} + \mathbf{w} \cdot \nabla \boldsymbol{D} \cdot \hat{\mathbf{e}}\right] A^{(0)}. \tag{A.31}$$

We can write the solution to equation (A.31) in terms of the derivatives of $\hat{\mathbf{e}}(\mathbf{r}, \mathbf{K})$ Taking any derivative of equation (23), we get

$$\partial_\mu \boldsymbol{D} \cdot \hat{\mathbf{e}} + \boldsymbol{D} \cdot \partial_\mu \hat{\mathbf{e}} = (\partial_\mu H)\hat{\mathbf{e}}, \tag{A.32}$$

where we have used $H = 0$. The projection of equation (A.32) on $\hat{\mathbf{e}}^*$ gives

$$\partial_\mu H = \hat{\mathbf{e}}^* \cdot \partial_\mu \boldsymbol{D} \cdot \hat{\mathbf{e}}. \tag{A.33}$$

The projection perpendicular to $\hat{\mathbf{e}}^*$ gives

$$(\mathbf{1} - \hat{\mathbf{e}}\hat{\mathbf{e}}^*) \cdot \partial_\mu \boldsymbol{D} \cdot \hat{\mathbf{e}} = -\boldsymbol{D} \cdot \partial_\mu \hat{\mathbf{e}}. \tag{A.34}$$

This equation only gives the component of $\partial_\mu \hat{\mathbf{e}}$ perpendicular to $\hat{\mathbf{e}}$. The component of $\partial_\mu \hat{\mathbf{e}}$ parallel to $\hat{\mathbf{e}}$ is a free choice that is partially constrained by the condition $\hat{\mathbf{e}} \cdot \hat{\mathbf{e}}^* = 1$, equation (21). Indeed, even with this condition, $\hat{\mathbf{e}}$ is defined only up to a phase factor α,

$$\hat{\mathbf{e}} \to \hat{\mathbf{e}} \exp(\mathrm{i}\alpha). \tag{A.35}$$

Hence, one can always add a vector parallel to $\hat{\mathbf{e}}$ to $\partial_\mu \hat{\mathbf{e}}$,

$$\partial_\mu \hat{\mathbf{e}} \to \partial_\mu \hat{\mathbf{e}} + \mathrm{i}\hat{\mathbf{e}}\partial_\mu\alpha. \tag{A.36}$$

This result shows that the condition $\hat{\mathbf{e}} \cdot \hat{\mathbf{e}}^* = 1$ constrains the component of $\partial_\mu \hat{\mathbf{e}}$ along $\hat{\mathbf{e}}$ to be purely imaginary. To summarise, while $\partial_\mu \hat{\mathbf{e}} \cdot (\mathbf{1} - \hat{\mathbf{e}}^*\hat{\mathbf{e}})$ is uniquely determined by the beam tracing equations and is thus physical, $\partial_\mu \hat{\mathbf{e}} \cdot \hat{\mathbf{e}}^*\hat{\mathbf{e}}$ can be chosen at will and it does not have any particular physical meaning. Using the result in equation (A.31), and noticing that equation (A.31) is perpendicular to $\hat{\mathbf{e}}^*$ when equations (A.29) and (A.30) are satisfied, we find

$$\mathbf{A}^{(1)} = \left[\left(-\mathbf{w} \cdot \nabla_w H\frac{\hat{\mathbf{g}}}{g} + \mathbf{w} \cdot \boldsymbol{\Psi}_w\right) \cdot \nabla_K \hat{\mathbf{e}} + \mathbf{w} \cdot \nabla\hat{\mathbf{e}}\right] A^{(0)}. \tag{A.37}$$

Appendix A.3. Second order

To get the contributions to equation (4) that are second order in $\lambda/W \sim W/L \ll 1$, we need to evaluate $\nabla\mathbf{A}$,

$$\nabla\mathbf{A} \simeq \frac{d}{d\tau}(A^{(0)}\hat{\mathbf{e}})\nabla\tau + \nabla_w\mathbf{A}^{(1)}, \tag{A.38}$$

where we have noted that $\nabla_w\mathbf{A}^{(1)} \sim \nabla(A^{(0)}\hat{\mathbf{e}})$. To lowest order, $\nabla\tau \simeq \hat{\mathbf{g}}/g$. To find $\nabla_w\mathbf{A}^{(1)}$, we take the derivative of equation (A.37),

$$\nabla_w\mathbf{A}^{(1)} = \left[-\nabla_w H\frac{\hat{\mathbf{g}}}{g} \cdot \nabla_K\hat{\mathbf{e}} + \boldsymbol{\Psi}_w \cdot \nabla_K\hat{\mathbf{e}} + \nabla_w\hat{\mathbf{e}}\right] A^{(0)}. \tag{A.39}$$

It is convenient to define a new tensor $\boldsymbol{\Psi}$ that contains $\boldsymbol{\Psi}_w$. The tensor $\boldsymbol{\Psi}$ is the lowest order result for $\nabla\nabla\psi$, given in equation (A.12),

$$\boldsymbol{\Psi} = \nabla\nabla\psi. \tag{A.40}$$

With this definition of $\boldsymbol{\Psi}$, we find

$$\boldsymbol{\Psi} \cdot \nabla_K H = \frac{\mathrm{d}\mathbf{K}}{\mathrm{d}\tau} = -\nabla H, \tag{A.41}$$

$$\nabla_w \mathbf{A}^{(1)} = A^{(0)}(\boldsymbol{\Psi} \cdot \nabla_K + \nabla)_w \hat{\mathbf{e}}, \tag{A.42}$$

and

$$(\nabla\psi)^{(1)} = \boldsymbol{\Psi} \cdot \mathbf{w}. \tag{A.43}$$

Using equations (A.4), (A.10), (A.13), (A.38), and (A.40), we find the second order contribution to (4),

$$
\begin{aligned}
\boldsymbol{D} \cdot \mathbf{A}^{(2)} &+ (\nabla\psi)^{(1)} \cdot \nabla_K \boldsymbol{D} \cdot \mathbf{A}^{(1)} \\
&+ (\nabla\psi)^{(2)} \cdot \nabla_K \boldsymbol{D} \cdot \hat{\mathbf{e}} A^{(0)} + \frac{1}{2}(\nabla\psi)^{(1)}(\nabla\psi)^{(1)} : \nabla_K \nabla_K \boldsymbol{D} \cdot \hat{\mathbf{e}} A^{(0)} \\
&+ \mathbf{w} \cdot \nabla\boldsymbol{\epsilon} \cdot \mathbf{A}^{(1)} + \frac{1}{2}\mathbf{w}\mathbf{w} : \nabla\nabla\boldsymbol{\epsilon} \cdot \hat{\mathbf{e}} A^{(0)} \\
&- \mathrm{i}\frac{c^2}{\Omega^2}\left[\frac{\hat{\mathbf{g}}}{g}\frac{\mathrm{d}}{\mathrm{d}\tau}\left(A^{(0)}\hat{\mathbf{e}}\right) + \nabla_w \mathbf{A}^{(1)}\right] \cdot (\nabla\psi)^{(0)} \\
&+ 2\mathrm{i}\frac{c^2}{\Omega^2}(\nabla\psi)^{(0)} \cdot \left[\frac{\hat{\mathbf{g}}}{g}\frac{\mathrm{d}}{\mathrm{d}\tau}\left(A^{(0)}\hat{\mathbf{e}}\right) + \nabla_w \mathbf{A}^{(1)}\right] \\
&- \mathrm{i}\frac{c^2}{\Omega^2}(\nabla\psi)^{(0)}\left[\frac{\hat{\mathbf{g}}}{g} \cdot \frac{\mathrm{d}}{\mathrm{d}\tau}\left(A^{(0)}\hat{\mathbf{e}}\right) + \nabla_w \cdot \mathbf{A}^{(1)}\right] \\
&- \mathrm{i}\frac{c^2}{\Omega^2}A^{(0)}\boldsymbol{\Psi} \cdot \hat{\mathbf{e}} + \mathrm{i}\frac{c^2}{\Omega^2}A^{(0)}\hat{\mathbf{e}}\boldsymbol{\Psi} : \mathbf{1} = 0.
\end{aligned} \tag{A.44}
$$

To eliminate $\boldsymbol{D} \cdot \mathbf{A}^{(2)}$ from the equation, we contract the free index with $\hat{\mathbf{e}}^*$. We remark that some of the terms depend on $\mathbf{w}$ while the others do not. Since the equation must be valid regardless of the particular value of $\mathbf{w}$, we can separate it into two separate independent equations, one of which depends on $\mathbf{w}$, and the other having no $\mathbf{w}$ dependence. The equations that we derive from the piece of equation (A.44) that depends on $\mathbf{w}$ will determine the evolution of $\boldsymbol{\Psi}_w$, whereas the piece independent of $\mathbf{w}$ gives the equation for $A^{(0)}$. Note that the components of $\boldsymbol{\Psi}$ that are not in $\boldsymbol{\Psi}_w$ are determined by equation (A.41).

Appendix A.3.1. Pieces proportional to $\mathbf{ww}$. Using equations (A.11), (A.37), (A.42), and (A.43), the terms proportional to $\mathbf{ww}$ in equation (A.44) give

$$
\frac{1}{2g}\left[\mathbf{w}\cdot\frac{\mathrm{d}\boldsymbol{\Psi}_w}{\mathrm{d}\tau}\cdot\mathbf{w}+2gK_g(\boldsymbol{\kappa}\cdot\mathbf{w})^2+2(\boldsymbol{\kappa}\cdot\mathbf{w})\frac{\mathrm{d}\mathbf{K}_w}{\mathrm{d}\tau}\cdot\mathbf{w}\right]\left(\hat{g}_\mu\hat{\mathbf{e}}^*\cdot\frac{\partial\boldsymbol{D}}{\partial K_\mu}\cdot\hat{\mathbf{e}}\right)
$$

$$
+\mathrm{w}_\mu\Psi_{\mu\nu}\hat{\mathbf{e}}^*\cdot\frac{\partial\boldsymbol{D}}{\partial K_\nu}\cdot\left(\mathrm{w}_\alpha\Psi_{\alpha\beta}\frac{\partial\hat{\mathbf{e}}}{\partial K_\beta}+\mathrm{w}_\beta\frac{\partial\hat{\mathbf{e}}}{\partial r_\beta}\right)
$$

$$
+\frac{1}{2}(\mathrm{w}_\mu\Psi_{\mu\nu})(\mathrm{w}_\alpha\Psi_{\alpha\beta})\hat{\mathbf{e}}^*\cdot\frac{\partial^2\boldsymbol{D}}{\partial K_\nu K_\beta}\cdot\hat{\mathbf{e}}\qquad\text{(A.45)}
$$

$$
+\mathrm{w}_\nu\hat{\mathbf{e}}^*\cdot\frac{\partial\boldsymbol{D}}{\partial r_\nu}\cdot\left(\mathrm{w}_\alpha\Psi_{\alpha\beta}\frac{\partial\hat{\mathbf{e}}}{\partial K_\beta}+\mathrm{w}_\beta\frac{\partial\hat{\mathbf{e}}}{\partial r_\beta}\right)
$$

$$
+\frac{1}{2}\mathrm{w}_\nu\mathrm{w}_\beta\hat{\mathbf{e}}^*\cdot\frac{\partial^2\boldsymbol{D}}{\partial r_\nu r_\beta}\cdot\hat{\mathbf{e}}=0.
$$

We now use equations (A.27), (A.40), and (A.12) to write

$$
\mathbf{w}\cdot\frac{\mathrm{d}\boldsymbol{\Psi}_w}{\mathrm{d}\tau}\cdot\mathbf{w}=\mathbf{w}\cdot\frac{\mathrm{d}\boldsymbol{\Psi}}{\mathrm{d}\tau}\cdot\mathbf{w}-2gK_g(\boldsymbol{\kappa}\cdot\mathbf{w})^2-2(\boldsymbol{\kappa}\cdot\mathbf{w})\frac{\mathrm{d}\mathbf{K}_w}{\mathrm{d}\tau}\cdot\mathbf{w}.\qquad\text{(A.46)}
$$

We then substitute equation (A.46) into equation (A.45) and use

$$
\hat{g}_\mu\hat{\mathbf{e}}^*\cdot\frac{\partial\boldsymbol{D}}{\partial K_\mu}\cdot\hat{\mathbf{e}}=\hat{\mathbf{g}}\cdot\nabla_K H=g\qquad\text{(A.47)}
$$

to get

$$
\mathbf{w}\cdot\frac{\mathrm{d}\boldsymbol{\Psi}}{\mathrm{d}\tau}\cdot\mathbf{w}
$$

$$
+2\mathrm{w}_\mu\Psi_{\mu\nu}\hat{\mathbf{e}}^*\cdot\frac{\partial\boldsymbol{D}}{\partial K_\nu}\cdot\left(\mathrm{w}_\alpha\Psi_{\alpha\beta}\frac{\partial\hat{\mathbf{e}}}{\partial K_\beta}+\mathrm{w}_\beta\frac{\partial\hat{\mathbf{e}}}{\partial r_\beta}\right)+(\mathrm{w}_\mu\Psi_{\mu\nu})(\mathrm{w}_\alpha\Psi_{\alpha\beta})\hat{\mathbf{e}}^*\cdot\frac{\partial^2\boldsymbol{D}}{\partial K_\nu K_\beta}\cdot\hat{\mathbf{e}}\quad\text{(A.48)}
$$

$$
+2\mathrm{w}_\nu\hat{\mathbf{e}}^*\cdot\frac{\partial\boldsymbol{D}}{\partial r_\nu}\cdot\left(\mathrm{w}_\alpha\Psi_{\alpha\beta}\frac{\partial\hat{\mathbf{e}}}{\partial K_\beta}+\mathrm{w}_\beta\frac{\partial\hat{\mathbf{e}}}{\partial r_\beta}\right)+\mathrm{w}_\nu\mathrm{w}_\beta\hat{\mathbf{e}}^*\cdot\frac{\partial^2\boldsymbol{D}}{\partial r_\nu\partial r_\beta}\cdot\hat{\mathbf{e}}=0.
$$

This expression can be rewritten in terms of derivatives of the dispersion relation H. Differentiating $\boldsymbol{D}\cdot\hat{\mathbf{e}}=H\hat{\mathbf{e}}$, we find

$$
\partial_\mu\partial_\nu\boldsymbol{D}\cdot\hat{\mathbf{e}}+\partial_\nu\boldsymbol{D}\cdot\partial_\mu\hat{\mathbf{e}}+\partial_\mu\boldsymbol{D}\cdot\partial_\nu\hat{\mathbf{e}}+\boldsymbol{D}\cdot\partial_\mu\partial_\nu\hat{\mathbf{e}}
$$
$$
=(\partial_\mu\partial_\nu H)\hat{\mathbf{e}}+(\partial_\nu H)\partial_\mu\hat{\mathbf{e}}+(\partial_\mu H)\partial_\nu\hat{\mathbf{e}}+H\partial_\mu\partial_\nu\hat{\mathbf{e}}.\qquad\text{(A.49)}
$$

Contracting the free index in this equation with $\hat{\mathbf{e}}^*$, we get

$$
\hat{\mathbf{e}}^*\cdot\partial_\mu\partial_\nu\boldsymbol{D}\cdot\hat{\mathbf{e}}+\hat{\mathbf{e}}^*\cdot\partial_\nu\boldsymbol{D}\cdot\partial_\mu\hat{\mathbf{e}}+\hat{\mathbf{e}}^*\cdot\partial_\mu\boldsymbol{D}\cdot\partial_\nu\hat{\mathbf{e}}
$$
$$
=\partial_\mu\partial_\nu H+(\partial_\nu H)\partial_\mu\hat{\mathbf{e}}\cdot\hat{\mathbf{e}}^*+(\partial_\mu H)\partial_\nu\hat{\mathbf{e}}\cdot\hat{\mathbf{e}}^*,\qquad\text{(A.50)}
$$

where we have used $H=0$ and $\hat{\mathbf{e}}^*\cdot\boldsymbol{D}=0$. Using these results, employing the fact that the equation must hold true for arbitrary $\mathbf{w}$, and remembering that $\boldsymbol{\Psi}$ is symmetric, we find that

$$
\left(\frac{\mathrm{d}\boldsymbol{\Psi}}{\mathrm{d}\tau}+\nabla\nabla H+\boldsymbol{\Psi}\cdot\nabla_K\nabla H+\nabla\nabla_K H\cdot\boldsymbol{\Psi}+\boldsymbol{\Psi}\cdot\nabla_K\nabla_K H\cdot\boldsymbol{\Psi}\right)_w
$$

$$
+\left[(\boldsymbol{\Psi}\cdot\nabla_K H)(\boldsymbol{\Psi}\cdot\nabla_K\hat{\mathbf{e}}\cdot\hat{\mathbf{e}}^*)+(\boldsymbol{\Psi}\cdot\nabla_K\hat{\mathbf{e}}\cdot\hat{\mathbf{e}}^*)(\boldsymbol{\Psi}\cdot\nabla_K H)\right]_w
$$

$$
+\left[\nabla H(\nabla\hat{\mathbf{e}}\cdot\hat{\mathbf{e}}^*)+(\nabla\hat{\mathbf{e}}\cdot\hat{\mathbf{e}}^*)\nabla H\right]_w\qquad\text{(A.51)}
$$

$$
+\left[\boldsymbol{\Psi}\cdot\nabla_K H(\nabla\hat{\mathbf{e}}\cdot\hat{\mathbf{e}}^*)+(\boldsymbol{\Psi}\cdot\nabla_K\hat{\mathbf{e}}\cdot\hat{\mathbf{e}}^*)\nabla H\right]_w
$$

$$
+\left[\nabla H(\boldsymbol{\Psi}\cdot\nabla_K\hat{\mathbf{e}}\cdot\hat{\mathbf{e}}^*)+(\nabla\hat{\mathbf{e}}\cdot\hat{\mathbf{e}}^*)\boldsymbol{\Psi}\cdot\nabla_K H\right]_w=0.
$$

Here we use the notation $\boldsymbol{C}_w = (\mathbf{1} - \hat{\mathbf{g}}\hat{\mathbf{g}}) \cdot \boldsymbol{C} \cdot (\mathbf{1} - \hat{\mathbf{g}}\hat{\mathbf{g}})$, where $\boldsymbol{C}$ is an arbitrary 3D matrix. We use equation (A.41) to get

$$\left(\frac{\mathrm{d}\boldsymbol{\Psi}}{\mathrm{d}\tau} + \boldsymbol{\Psi} \cdot \nabla_K \nabla_K H \cdot \boldsymbol{\Psi} + \boldsymbol{\Psi} \cdot \nabla_K \nabla H + \nabla\nabla_K H \cdot \boldsymbol{\Psi} + \nabla\nabla H\right)_w = 0, \qquad \text{(A.52)}$$

which gives the components of $\mathrm{d}\boldsymbol{\Psi}/\mathrm{d}\tau$ perpendicular to the beam. To obtain the components parallel to the beam, $\mathrm{d}\boldsymbol{\Psi}/\mathrm{d}\tau \cdot \hat{\mathbf{g}}$, we differentiate equation (A.41) with respect to τ,

$$\frac{\mathrm{d}\boldsymbol{\Psi}}{\mathrm{d}\tau} \cdot \hat{\mathbf{g}} + (\boldsymbol{\Psi} \cdot \nabla_K \nabla_K H \cdot \boldsymbol{\Psi} + \boldsymbol{\Psi} \cdot \nabla_K \nabla H + \nabla\nabla_K H \cdot \boldsymbol{\Psi} + \nabla\nabla H) \cdot \hat{\mathbf{g}} = 0, \qquad \text{(A.53)}$$

where we have used $\mathrm{d}(\partial_\mu H)/\mathrm{d}\tau = \mathbf{g} \cdot \nabla(\partial_\mu H) + \mathrm{d}\mathbf{K}/\mathrm{d}\tau \cdot \nabla_K(\partial_\mu H)$, equations (A.29), (A.30), and (A.41), as well as the symmetry of $\boldsymbol{\Psi}$. Recalling that $(\mathrm{d}\boldsymbol{\Psi}/\mathrm{d}\tau)_w = (\mathbf{1} - \hat{\mathbf{g}}\hat{\mathbf{g}}) \cdot (\mathrm{d}\boldsymbol{\Psi}/\mathrm{d}\tau) \cdot (\mathbf{1} - \hat{\mathbf{g}}\hat{\mathbf{g}})$, equations (A.52) and (A.53) give

$$\frac{\mathrm{d}\boldsymbol{\Psi}}{\mathrm{d}\tau} + \boldsymbol{\Psi} \cdot \nabla_K \nabla_K H \cdot \boldsymbol{\Psi} + \boldsymbol{\Psi} \cdot \nabla_K \nabla H + \nabla\nabla_K H \cdot \boldsymbol{\Psi} + \nabla\nabla H = 0. \quad \text{(A.54)}$$

Appendix A.3.2. Pieces independent of $\mathbf{w}$. Using equations (A.11) and (A.42), the terms independent of $\mathbf{w}$ in equation (A.44) give

$$\frac{1}{gA^{(0)}} \left[(\mathbf{K} \cdot \hat{\mathbf{e}})\hat{\mathbf{e}}^* + (\mathbf{K} \cdot \hat{\mathbf{e}}^*)\hat{\mathbf{e}} - 2\mathbf{K}\right] \cdot \hat{\mathbf{g}} \frac{\mathrm{d}A^{(0)}}{\mathrm{d}\tau}$$
$$+ \boldsymbol{\Psi} : (\hat{\mathbf{e}}^*\hat{\mathbf{e}} - \mathbf{1}) + \frac{1}{g}\left[(\hat{\mathbf{e}}^* \cdot \hat{\mathbf{g}})\frac{\mathrm{d}\hat{\mathbf{e}}}{\mathrm{d}\tau} \cdot \mathbf{K} + (\mathbf{K} \cdot \hat{\mathbf{e}}^*)\hat{\mathbf{g}} \cdot \frac{\mathrm{d}\hat{\mathbf{e}}}{\mathrm{d}\tau} - 2(\mathbf{K} \cdot \hat{\mathbf{g}})\frac{\mathrm{d}\hat{\mathbf{e}}}{\mathrm{d}\tau} \cdot \hat{\mathbf{e}}^*\right]$$
$$+ \hat{\mathbf{e}}^* \cdot (\mathbf{1} - \hat{\mathbf{g}}\hat{\mathbf{g}}) \cdot (\boldsymbol{\Psi} \cdot \nabla_K \hat{\mathbf{e}} + \nabla\hat{\mathbf{e}}) \cdot \mathbf{K} \qquad \text{(A.55)}$$
$$+ (\mathbf{K} \cdot \hat{\mathbf{e}}^*)(\mathbf{1} - \hat{\mathbf{g}}\hat{\mathbf{g}}) : (\boldsymbol{\Psi} \cdot \nabla_K \hat{\mathbf{e}} + \nabla\hat{\mathbf{e}})$$
$$- 2\mathbf{K} \cdot (\mathbf{1} - \hat{\mathbf{g}}\hat{\mathbf{g}}) \cdot (\boldsymbol{\Psi} \cdot \nabla_K \hat{\mathbf{e}} + \nabla\hat{\mathbf{e}}) \cdot \hat{\mathbf{e}}^* = 0.$$

Noting that equation (A.41) can be used to write

$$g\hat{\mathbf{g}} \cdot (\boldsymbol{\Psi} \cdot \nabla_K \hat{\mathbf{e}} + \nabla\hat{\mathbf{e}}) = \frac{\mathrm{d}\mathbf{K}}{\mathrm{d}\tau} \cdot \nabla_K \hat{\mathbf{e}} + \frac{\mathrm{d}\mathbf{q}}{\mathrm{d}\tau} \cdot \nabla\hat{\mathbf{e}} = \frac{\mathrm{d}\hat{\mathbf{e}}}{\mathrm{d}\tau}, \qquad \text{(A.56)}$$

we find that

$$\frac{1}{g}\left[(\hat{\mathbf{e}}^* \cdot \hat{\mathbf{g}})\frac{\mathrm{d}\hat{\mathbf{e}}}{\mathrm{d}\tau} \cdot \mathbf{K} + (\mathbf{K} \cdot \hat{\mathbf{e}}^*)\hat{\mathbf{g}} \cdot \frac{\mathrm{d}\hat{\mathbf{e}}}{\mathrm{d}\tau} - 2(\mathbf{K} \cdot \hat{\mathbf{g}})\frac{\mathrm{d}\hat{\mathbf{e}}}{\mathrm{d}\tau} \cdot \hat{\mathbf{e}}^*\right]$$
$$= (\hat{\mathbf{e}}^* \cdot \hat{\mathbf{g}})\hat{\mathbf{g}} \cdot (\boldsymbol{\Psi} \cdot \nabla_K \hat{\mathbf{e}} + \nabla\hat{\mathbf{e}}) \cdot \mathbf{K} + (\mathbf{K} \cdot \hat{\mathbf{e}}^*)\hat{\mathbf{g}}\hat{\mathbf{g}} : (\boldsymbol{\Psi} \cdot \nabla_K \hat{\mathbf{e}} + \nabla\hat{\mathbf{e}}) \qquad \text{(A.57)}$$
$$- 2(\mathbf{K} \cdot \hat{\mathbf{g}})\hat{\mathbf{g}} \cdot (\boldsymbol{\Psi} \cdot \nabla_K \hat{\mathbf{e}} + \nabla\hat{\mathbf{e}}) \cdot \hat{\mathbf{e}}^*.$$

Using equations (A.18), (A.29), and (A.57), equation (A.55) becomes

$$\frac{\Omega^2}{c^2}\frac{\mathrm{d}\ln A^{(0)}}{\mathrm{d}\tau} + \boldsymbol{\Psi} : (\hat{\mathbf{e}}^*\hat{\mathbf{e}} - \mathbf{1}) + \hat{\mathbf{e}}^* \cdot (\boldsymbol{\Psi} \cdot \nabla_K \hat{\mathbf{e}} + \nabla\hat{\mathbf{e}}) \cdot \mathbf{K}$$
$$+ (\mathbf{K} \cdot \hat{\mathbf{e}}^*)(\boldsymbol{\Psi} : \nabla_K \hat{\mathbf{e}} + \nabla \cdot \hat{\mathbf{e}}) - 2\mathbf{K} \cdot (\boldsymbol{\Psi} \cdot \nabla_K \hat{\mathbf{e}} + \nabla\hat{\mathbf{e}}) \cdot \hat{\mathbf{e}}^* = 0. \qquad \text{(A.58)}$$

Noting that

$$\hat{\mathbf{e}}^* \cdot \frac{\partial \boldsymbol{D}}{\partial K_\mu} \cdot \partial_\nu \hat{\mathbf{e}} = \frac{c^2}{\Omega^2}(\mathbf{K} \cdot \hat{\mathbf{e}}^*)\partial_\nu \hat{e}_\mu + \frac{c^2}{\Omega^2}(\mathbf{K} \cdot \partial_\nu \hat{\mathbf{e}})\hat{e}_\mu^* - 2\frac{c^2}{\Omega^2}(\hat{\mathbf{e}}^* \cdot \partial_\nu \hat{\mathbf{e}})K_\mu, \qquad \text{(A.59)}$$

$$\hat{\mathbf{e}}^* \cdot \frac{\partial^2 \boldsymbol{D}}{\partial K_\mu \partial K_\nu} \cdot \hat{\mathbf{e}} = \frac{c^2}{\Omega^2} \hat{e}_\mu^* \hat{e}_\nu + \frac{c^2}{\Omega^2} \hat{e}_\mu \hat{e}_\nu^* - \frac{c^2}{\Omega^2} 2\delta_{\mu\nu}, \tag{A.60}$$

and that $\boldsymbol{\Psi}$ is symmetric, we can simplify equation (A.58) further, getting

$$\frac{\mathrm{d}\ln A^{(0)}}{\mathrm{d}\tau} + \Psi_{\mu\nu}\left(\frac{1}{2}\hat{\mathbf{e}}^* \cdot \frac{\partial^2 \boldsymbol{D}}{\partial K_\mu \partial K_\nu} \cdot \hat{\mathbf{e}} + \hat{\mathbf{e}}^* \cdot \frac{\partial \boldsymbol{D}}{\partial K_\mu} \cdot \frac{\partial \hat{\mathbf{e}}}{\partial K_\nu}\right)$$
$$+ \hat{\mathbf{e}}^* \cdot \frac{\partial \boldsymbol{D}}{\partial K_\mu} \cdot \frac{\partial \hat{\mathbf{e}}}{\partial r_\mu} = 0. \tag{A.61}$$

Using equation (A.50), equation (A.61) simplifies to

$$\frac{\mathrm{d}\ln A^{(0)}}{\mathrm{d}\tau} + \frac{1}{2}\boldsymbol{\Psi} : \nabla_K \nabla_K H + \nabla_K H \cdot \boldsymbol{\Psi} \cdot \nabla_K \hat{\mathbf{e}} \cdot \hat{\mathbf{e}}^* + \hat{\mathbf{e}}^* \cdot \frac{\partial \boldsymbol{D}}{\partial K_\mu} \cdot \frac{\partial \hat{\mathbf{e}}}{\partial r_\mu} = 0. \tag{A.62}$$

We then use equation (A.41), getting

$$\frac{\mathrm{d}\ln A^{(0)}}{\mathrm{d}\tau} + \frac{1}{2}\boldsymbol{\Psi} : \nabla_K \nabla_K H + \frac{\mathrm{d}\mathbf{K}}{\mathrm{d}\tau} \cdot \nabla_K \hat{\mathbf{e}} \cdot \hat{\mathbf{e}}^* + \hat{\mathbf{e}}^* \cdot \frac{\partial \boldsymbol{D}}{\partial K_\mu} \cdot \frac{\partial \hat{\mathbf{e}}}{\partial r_\mu} = 0. \tag{A.63}$$

To solve for $A^{(0)}$ using equation (A.63), we write $A^{(0)}$ as $A^{(0)} = |A^{(0)}|\exp(\mathrm{i}\phi^{(0)})$. The real part of equation (A.63) gives the equation for $|A^{(0)}|$, and its imaginary part the equation for $\phi^{(0)}$. The real part of equation (A.63) is

$$\frac{\mathrm{d}\ln |A^{(0)}|}{\mathrm{d}\tau} + \frac{1}{2}\mathrm{Re}(\boldsymbol{\Psi}) : \nabla_K \nabla_K H + \frac{1}{2}\left(\hat{\mathbf{e}}^* \cdot \frac{\partial \boldsymbol{D}}{\partial K_\mu} \cdot \frac{\partial \hat{\mathbf{e}}}{\partial r_\mu} + \frac{\partial \hat{\mathbf{e}}^*}{\partial r_\mu} \cdot \frac{\partial \boldsymbol{D}}{\partial K_\mu} \cdot \hat{\mathbf{e}}\right) = 0, \tag{A.64}$$

where we have used $\hat{\mathbf{e}} \cdot \partial \hat{\mathbf{e}}^*/\partial K_\mu + \hat{\mathbf{e}}^* \cdot \partial \hat{\mathbf{e}}/\partial K_\mu = \partial(\hat{\mathbf{e}}^* \cdot \hat{\mathbf{e}})/\partial K_\mu = 0$, the fact that $\partial \boldsymbol{D}/\partial K_\mu$ is Hermitian, and that only $\boldsymbol{\Psi}$ and $\hat{\mathbf{e}}$ are complex. We then differentiate $H = \hat{\mathbf{e}}^* \cdot \boldsymbol{D} \cdot \hat{\mathbf{e}}$ and use $\partial^2 \boldsymbol{D}/\partial K_\mu \partial r_\nu = 0$ and equation (A.32) to obtain

$$\frac{\partial^2 H}{\partial K_\mu \partial r_\mu} = \frac{\partial \hat{\mathbf{e}}^*}{\partial r_\mu} \cdot \frac{\partial \boldsymbol{D}}{\partial K_\mu} \cdot \hat{\mathbf{e}} + \hat{\mathbf{e}}^* \cdot \frac{\partial \boldsymbol{D}}{\partial K_\mu} \cdot \frac{\partial \hat{\mathbf{e}}}{\partial r_\mu}, \tag{A.65}$$

to get

$$\frac{\mathrm{d}\ln |A^{(0)}|}{\mathrm{d}\tau} + \frac{1}{2}\mathrm{Re}(\boldsymbol{\Psi}) : \nabla_K \nabla_K H + \frac{1}{2}\nabla \cdot \nabla_K H = 0. \tag{A.66}$$

The magnitude $|A^{(0)}|$ is related to $\det[\mathrm{Im}(\boldsymbol{\Psi}_w)]$, where we have defined the determinant to be

$$\det(\boldsymbol{\Psi}_w) = \begin{vmatrix} \Psi_{xx} & \Psi_{xy} \\ \Psi_{yx} & \Psi_{yy} \end{vmatrix}. \tag{A.67}$$

To prove that $|A^{(0)}|$ is related to $\det[\mathrm{Im}(\boldsymbol{\Psi}_w)]$, we evaluate

$$\frac{\mathrm{d}}{\mathrm{d}\tau}\det[\mathrm{Im}(\boldsymbol{\Psi}_w)] = \det[\mathrm{Im}(\boldsymbol{\Psi}_w)][\mathrm{Im}(\boldsymbol{\Psi}_w)]^{-1} : \frac{\mathrm{d}\,\mathrm{Im}(\boldsymbol{\Psi}_w)}{\mathrm{d}\tau}, \tag{A.68}$$

where we define

$$\boldsymbol{\Psi}_w^{-1} = \begin{pmatrix} \begin{pmatrix} \Psi_{xx} & \Psi_{xy} \\ \Psi_{yx} & \Psi_{yy} \end{pmatrix}^{-1} & \begin{matrix} 0 \\ 0 \end{matrix} \\ \begin{matrix} 0 & 0 \end{matrix} & 0 \end{pmatrix}. \tag{A.69}$$

We use equation (A.54) to find d Im($\boldsymbol{\Psi}$)/dτ, which is

$$\frac{\mathrm{d}\,\mathrm{Im}(\boldsymbol{\Psi})}{\mathrm{d}\tau} = -\,\mathrm{Im}(\boldsymbol{\Psi}) \cdot \nabla_K \nabla_K H \cdot \mathrm{Re}(\boldsymbol{\Psi}) - \mathrm{Re}(\boldsymbol{\Psi}) \cdot \nabla_K \nabla_K H \cdot \mathrm{Im}(\boldsymbol{\Psi})$$
$$- \mathrm{Im}(\boldsymbol{\Psi}) \cdot \nabla_K \nabla H - \nabla \nabla_K H \cdot \mathrm{Im}(\boldsymbol{\Psi}). \tag{A.70}$$

Substituting equation (A.70) into equation (A.68), and using $\mathrm{Im}(\boldsymbol{\Psi}_w) \cdot [\mathrm{Im}(\boldsymbol{\Psi}_w)]^{-1} = \mathbf{1} - \hat{\mathbf{g}}\hat{\mathbf{g}}$, we get

$$\frac{\mathrm{d}}{\mathrm{d}\tau} \ln(\det[\mathrm{Im}(\boldsymbol{\Psi}_w)]) = -2(\mathbf{1} - \hat{\mathbf{g}}\hat{\mathbf{g}}) : [\mathrm{Re}(\boldsymbol{\Psi}) \cdot \nabla_K \nabla_K H + \nabla_K \nabla H]. \tag{A.71}$$

Using this result and equation (A.66), we find

$$\frac{\mathrm{d}\ln|A^{(0)}|}{\mathrm{d}\tau} = \frac{1}{4}\frac{\mathrm{d}}{\mathrm{d}\tau}\ln(\det[\mathrm{Im}(\boldsymbol{\Psi}_w)]) - \frac{1}{2}\hat{\mathbf{g}} \cdot \mathrm{Re}(\boldsymbol{\Psi}) \cdot \nabla_K \nabla_K H \cdot \hat{\mathbf{g}} - \frac{1}{2}\hat{\mathbf{g}} \cdot \nabla_K \nabla H \cdot \hat{\mathbf{g}}. \tag{A.72}$$

Using the fact that $\hat{\mathbf{g}}$ is purely real and taking the real part of equation (A.41), we find that

$$\hat{\mathbf{g}} \cdot \mathrm{Re}(\boldsymbol{\Psi}) = \frac{1}{g}\frac{\mathrm{d}\mathbf{K}}{\mathrm{d}\tau}. \tag{A.73}$$

Hence,

$$\hat{\mathbf{g}} \cdot \mathrm{Re}(\boldsymbol{\Psi}) \cdot \nabla_K \nabla_K H \cdot \hat{\mathbf{g}} + \hat{\mathbf{g}} \cdot \nabla_K \nabla H \cdot \hat{\mathbf{g}}$$
$$= \frac{\hat{\mathbf{g}}}{g} \cdot \nabla_K \nabla_K H \cdot \frac{\mathrm{d}\mathbf{K}}{\mathrm{d}\tau} + \frac{\hat{\mathbf{g}}}{g} \cdot \nabla \nabla_K H \cdot \frac{\mathrm{d}\mathbf{q}}{\mathrm{d}\tau}, \tag{A.74}$$

where we have used the definition of group velocity in equation (A.29). Substituting this result into equation (A.72), and noting that

$$\frac{\mathrm{d}\mathbf{g}}{\mathrm{d}\tau} = \frac{\mathrm{d}}{\mathrm{d}\tau}(\nabla_K H) = \frac{\mathrm{d}\mathbf{K}}{\mathrm{d}\tau} \cdot \nabla_K \nabla_K H + \frac{\mathrm{d}\mathbf{q}}{\mathrm{d}\tau} \cdot \nabla \nabla_K H, \tag{A.75}$$

we find

$$\frac{\mathrm{d}\ln|A^{(0)}|}{\mathrm{d}\tau} = \frac{1}{4}\frac{\mathrm{d}}{\mathrm{d}\tau}\ln(\det[\mathrm{Im}(\boldsymbol{\Psi}_w)]) - \frac{1}{2}\frac{\hat{\mathbf{g}}}{g} \cdot \frac{\mathrm{d}\mathbf{g}}{\mathrm{d}\tau}. \tag{A.76}$$

Using $g^{-1}\hat{\mathbf{g}} \cdot \mathrm{d}\mathbf{g}/\mathrm{d}\tau = \mathrm{d}\ln g/\mathrm{d}\tau$ and simplifying, we get

$$|A^{(0)}| = C\frac{[\det(\mathrm{Im}(\boldsymbol{\Psi}_w))]^{\frac{1}{4}}}{g^{\frac{1}{2}}}, \tag{A.77}$$

where C is a constant of integration.

The imaginary part of equation (A.63) gives us

$$\frac{\mathrm{d}\phi^{(0)}}{\mathrm{d}\tau} = -\mathrm{Im}(\boldsymbol{\Psi}) : \nabla_K \nabla_K H$$
$$+ \mathrm{i}\frac{\mathrm{d}K}{\mathrm{d}\tau} \cdot \nabla_K \hat{\mathbf{e}} \cdot \hat{\mathbf{e}}^* - \frac{1}{2\mathrm{i}}\left(\hat{\mathbf{e}}^* \cdot \frac{\partial \boldsymbol{D}}{\partial K_\mu} \cdot \frac{\partial \hat{\mathbf{e}}}{\partial r_\mu} - \frac{\partial \hat{\mathbf{e}}^*}{\partial r_\mu} \cdot \frac{\partial \boldsymbol{D}}{\partial K_\mu} \cdot \hat{\mathbf{e}}\right), \tag{A.78}$$

where we have once again used $\hat{\mathbf{e}} \cdot \partial \hat{\mathbf{e}}^*/\partial K_\mu + \hat{\mathbf{e}}^* \cdot \partial \hat{\mathbf{e}}/\partial K_\mu = \partial(\hat{\mathbf{e}}^* \cdot \hat{\mathbf{e}})/\partial K_\mu = 0$. Using equations (A.29) and (A.33), we can rewrite this equation as

$$\frac{\mathrm{d}\phi^{(0)}}{\mathrm{d}\tau} = -\mathrm{Im}(\boldsymbol{\Psi}) : \nabla_K \nabla_K H$$
$$+ \mathrm{i}\frac{\mathrm{d}\hat{\mathbf{e}}}{\mathrm{d}\tau} \cdot \hat{\mathbf{e}}^* - \frac{1}{2\mathrm{i}}\left(\hat{\mathbf{e}}^* \cdot \frac{\partial \boldsymbol{D}}{\partial K_\mu} \cdot (\mathbf{1} - \hat{\mathbf{e}}\hat{\mathbf{e}}^*) \cdot \frac{\partial \hat{\mathbf{e}}}{\partial r_\mu} - \frac{\partial \hat{\mathbf{e}}^*}{\partial r_\mu} \cdot (\mathbf{1} - \hat{\mathbf{e}}\hat{\mathbf{e}}^*) \cdot \frac{\partial \boldsymbol{D}}{\partial K_\mu} \cdot \hat{\mathbf{e}}\right). \tag{A.79}$$

For clarity, we have re-expressed the second and third terms of equation (A.78) as two new terms, one parallel to $\hat{\mathbf{e}}$, and the other perpendicular to it. Using equation (A.34), this simplifies to

$$
\begin{aligned}
\frac{\mathrm{d}\phi^{(0)}}{\mathrm{d}\tau} = & -\mathrm{Im}(\boldsymbol{\Psi}) : \nabla_K \nabla_K H \\
& + \mathrm{i}\frac{\mathrm{d}\hat{\mathbf{e}}}{\mathrm{d}\tau} \cdot \hat{\mathbf{e}}^* - \frac{1}{2\mathrm{i}} \left(\frac{\partial \hat{\mathbf{e}}^*}{\partial K_\mu} \cdot \boldsymbol{D} \cdot \frac{\partial \hat{\mathbf{e}}}{\partial r_\mu} - \frac{\partial \hat{\mathbf{e}}^*}{\partial r_\mu} \cdot \boldsymbol{D} \cdot \frac{\partial \hat{\mathbf{e}}}{\partial K_\mu} \right).
\end{aligned}
\tag{A.80}
$$

We separate $\phi^{(0)}$ into two parts, the Gouy phase ϕ_G and the phase ϕ_P associated with how the polarisation changes when the probe beam passes through a plasma. The former is a beam effect, whereas the latter is a result of ray tracing. We define the phases ϕ_G and ϕ_P by their evolution equations,

$$
\frac{\mathrm{d}\phi_G}{\mathrm{d}\tau} = -\mathrm{Im}(\boldsymbol{\Psi}) : \nabla_K \nabla_K H,
\tag{A.81}
$$

and

$$
\frac{\mathrm{d}\phi_P}{\mathrm{d}\tau} = \mathrm{i}\frac{\mathrm{d}\hat{\mathbf{e}}}{\mathrm{d}\tau} \cdot \hat{\mathbf{e}}^* - \frac{1}{2\mathrm{i}} \left(\frac{\partial \hat{\mathbf{e}}^*}{\partial K_\mu} \cdot \boldsymbol{D} \cdot \frac{\partial \hat{\mathbf{e}}}{\partial r_\mu} - \frac{\partial \hat{\mathbf{e}}^*}{\partial r_\mu} \cdot \boldsymbol{D} \cdot \frac{\partial \hat{\mathbf{e}}}{\partial K_\mu} \right).
\tag{A.82}
$$

The $\mathrm{d}\hat{\mathbf{e}}/\mathrm{d}\tau \cdot \hat{\mathbf{e}}^*$ piece corrects for our choice of the vectors $\partial_\mu \hat{\mathbf{e}} \cdot \hat{\mathbf{e}}^*$, as discussed at the end of Appendix A.2. If we had chosen the vectors $\partial_\mu \hat{\mathbf{e}} \cdot \hat{\mathbf{e}}^* = 0$, then we would get $\mathrm{d}\hat{\mathbf{e}}/\mathrm{d}\tau \cdot \hat{\mathbf{e}}^* = 0$. The other piece of $\mathrm{d}\phi_P/\mathrm{d}\tau$ is physical, and accounts for how the polarisation changes as $\mathbf{B}$ and n_e vary along the beam path.

Appendix B. Eigenvalues of $\boldsymbol{D}$

We find the eigenvalues of $\boldsymbol{D}$, given in equation (36) by solving the eigenvalue equation

$$
\det\left(\boldsymbol{D} - H\mathbf{1}\right) = \begin{vmatrix} D_{11} - H & -\mathrm{i}D_{12} & D_{1b} \\ \mathrm{i}D_{12} & D_{22} - H & 0 \\ D_{1b} & 0 & D_{bb} - H \end{vmatrix} = 0,
\tag{B.1}
$$

getting

$$
H^3 + h_2 H^2 + h_1 H + h_0 = 0,
\tag{B.2}
$$

where the coefficients h_2, h_1, and h_0 are

$$
h_2 = -D_{11} - D_{22} - D_{bb},
\tag{B.3}
$$

$$
h_1 = D_{11}D_{bb} + D_{11}D_{22} + D_{22}D_{bb} - D_{12}^2 - D_{1b}^2,
\tag{B.4}
$$

and

$$
h_0 = D_{22}D_{1b}^2 + D_{bb}D_{12}^2 - D_{11}D_{22}D_{bb}.
\tag{B.5}
$$

We use Cardano's formula to solve for H, getting three possible solutions

$$
H_1 = \frac{h_t}{3\sqrt[3]{2}} - \sqrt[3]{2}\frac{3h_1 - h_2^2}{3h_t} - \frac{h_2}{3},
\tag{B.6}
$$

$$H_2 = -\frac{1 - i\sqrt{3}}{6\sqrt[3]{2}}h_t + \left(1 + i\sqrt{3}\right)\frac{3h_1 - h_2^2}{3\sqrt[3]{4}h_t} - \frac{h_2}{3}, \tag{B.7}$$

and

$$H_3 = -\frac{1 + i\sqrt{3}}{6\sqrt[3]{2}}h_t + \left(1 - i\sqrt{3}\right)\frac{3h_1 - h_2^2}{3\sqrt[3]{4}h_t} - \frac{h_2}{3}, \tag{B.8}$$

where we have used the shorthand

$$h_t = \left[-2h_2^3 + 9h_2h_1 - 27h_0 + 3\sqrt{3}\left(4h_2^3h_0 - h_2^2h_1^2 - 18h_2h_1h_0 + 4h_1^3 + 27h_0^2\right)^{\frac{1}{2}}\right]^{\frac{1}{3}}. \tag{B.9}$$

We select the solution that is zero along the entire path of the ray, using it to calculate g in post-processing.

Appendix C. Discontinuity of $\boldsymbol{\Psi}$ at the vacuum-plasma boundary

We are going to look at a special case of the vacuum-plasma boundary, where the density n_e is continuous, but its gradient ∇n_e is discontinuous. Hence, the ray part of beam tracing is well-behaved, but there will be a discontinuity in the beam part. We need to find the matching conditions at the boundary for $\boldsymbol{\Psi}$. This is a special case of what was presented in earlier work [53].

We take the density to be zero on the plasma-vacuum interface. We also assume a general 2D curvature of the interface surface, which is relevant to our concerns because density is specified on flux surfaces, curved in 2D.

We re-express the exponential piece in $\mathbf{E}_b$ at the vacuum-plasma boundary as

$$\begin{aligned}
E_b \propto \exp\Big[&is^{vp} + iK_R^{vp}\Delta R + iK_Z^{vp}\Delta Z + iK_\zeta^{vp}\Delta\zeta \\
&+ \frac{i}{2}(\Psi_{RR}(\Delta R)^2 + 2\Psi_{RZ}\Delta R\Delta Z + \Psi_{ZZ}(\Delta Z)^2 \\
&+ \Psi_{\zeta\zeta}(\Delta\zeta)^2 + 2\Psi_{R\zeta}\Delta R\Delta\zeta + 2\Psi_{\zeta Z}\Delta\zeta\Delta Z)\Big],
\end{aligned} \tag{C.1}$$

where the superscript ^{vp} indicates that the variables are continuous across this boundary. We need to impose continuity of $\mathbf{E}_b$ across this boundary. Since we are dealing with the special case where the density is zero at the boundary, there is no charge or current, so all components of $\mathbf{E}_b$ are continuous. To proceed, we have to figure out how to parameterise the vacuum-plasma boundary. Since the density is specified on a flux surface, the discontinuity in $\boldsymbol{\Psi}$ occurs on a flux surface, which we take to also be the vacuum-plasma boundary. Two points on the same flux surface must have the same flux label. Hence, they are related by

$$\begin{aligned}
\psi_p(R, Z) &= \psi_p(R + \Delta R, Z + \Delta Z) \\
&\simeq \psi_p(R, Z) + \frac{\partial\psi_p}{\partial R}\Delta R + \frac{\partial\psi_p}{\partial Z}\Delta Z \\
&+ \frac{1}{2}\left(\frac{\partial^2\psi_p}{\partial R^2}(\Delta R)^2 + 2\frac{\partial^2\psi_p}{\partial R\partial Z}\Delta R\Delta Z + \frac{\partial^2\psi_p}{\partial Z^2}(\Delta Z)^2\right),
\end{aligned} \tag{C.2}$$

where we have expanded to second order. We write $\Delta R = \Delta R^{(0)} + \Delta R^{(1)} + \ldots$ and $\Delta Z = \Delta Z^{(0)} + \Delta Z^{(1)} + \ldots$. We parameterise poloidal displacement with ξ, such that

$$\begin{pmatrix} \Delta R^{(0)} \\ \Delta Z^{(0)} \end{pmatrix} = \begin{pmatrix} -\partial\psi_p/\partial Z \\ \partial\psi_p/\partial R \end{pmatrix} \xi. \tag{C.3}$$

This choice ensures that equation (C.2) is satisfied to first order. To second order, we find

$$\begin{aligned} & \frac{\partial\psi_p}{\partial R}\Delta R^{(1)} + \frac{\partial\psi_p}{\partial Z}\Delta Z^{(1)} \\ & + \frac{1}{2}\left(\frac{\partial^2\psi_p}{\partial R^2}\left(\Delta R^{(0)}\right)^2 + 2\frac{\partial^2\psi_p}{\partial R\partial Z}\Delta R^{(0)}\Delta Z^{(0)} + \frac{\partial^2\psi_p}{\partial Z^2}\left(\Delta Z^{(0)}\right)^2 \right) = 0. \end{aligned} \tag{C.4}$$

The next order corrections are thus

$$\begin{pmatrix} \Delta R^{(1)} \\ \Delta Z^{(1)} \end{pmatrix} = \begin{pmatrix} -\partial\psi_p/\partial Z \\ \partial\psi_p/\partial R \end{pmatrix} \xi^{(1)} + \eta \begin{pmatrix} \partial\psi_p/\partial R \\ \partial\psi_p/\partial Z \end{pmatrix}, \tag{C.5}$$

where η is given by

$$\begin{aligned} \eta = & -\frac{1}{2}\left[\frac{\partial^2\psi_p}{\partial R^2}\left(\frac{\partial\psi_p}{\partial Z}\right)^2 + 2\frac{\partial^2\psi_p}{\partial R\partial Z}\frac{\partial\psi_p}{\partial R}\frac{\partial\psi_p}{\partial Z} + \frac{\partial^2\psi_p}{\partial Z^2}\left(\frac{\partial\psi_p}{\partial R}\right)^2 \right] \\ & \times \left[\left(\frac{\partial\psi_p}{\partial R}\right)^2 + \left(\frac{\partial\psi_p}{\partial Z}\right)^2 \right]^{-1} \xi^2. \end{aligned} \tag{C.6}$$

We redefine ξ such that it incorporates the $\xi^{(1)}$ term, getting

$$\begin{pmatrix} \Delta R^{(1)} \\ \Delta Z^{(1)} \end{pmatrix} = \eta \begin{pmatrix} \partial\psi_p/\partial R \\ \partial\psi_p/\partial Z \end{pmatrix}. \tag{C.7}$$

Imposing continuity across the plasma-vacuum boundary, we find the formula

$$\begin{aligned} & s^{vp} + K_R^{vp}\Delta R + K_Z^{vp}\Delta Z + K_\zeta^{vp}\Delta\zeta + \frac{1}{2}\left(\Psi_{RR}^v\left(\Delta R\right)^2 + \Psi_{ZZ}^v\left(\Delta Z\right)^2 + \Psi_{\zeta\zeta}^v\left(\Delta\zeta\right)^2 \right) \\ & + \Psi_{RZ}^v\Delta R\Delta Z + \Psi_{R\zeta}^v\Delta R\Delta\zeta + \Psi_{\zeta Z}^v\Delta\zeta\Delta Z \\ = & s^{vp} + K_R^{vp}\Delta R + K_Z^{vp}\Delta Z + K_\zeta^{vp}\Delta\zeta + \frac{1}{2}\left(\Psi_{RR}^p\left(\Delta R\right)^2 + \Psi_{ZZ}^p\left(\Delta Z\right)^2 + \Psi_{\zeta\zeta}^p\left(\Delta\zeta\right)^2 \right) \\ & + \Psi_{RZ}^p\Delta R\Delta Z + \Psi_{R\zeta}^p\Delta R\Delta\zeta + \Psi_{\zeta Z}^p\Delta\zeta\Delta Z. \end{aligned} \tag{C.8}$$

We now consider displacement in the toroidal direction only, $\xi = 0$,

$$K_\zeta^{vp} + \frac{1}{2}\Psi_{\zeta\zeta}^v\left(\Delta\zeta\right)^2 = K_\zeta^{vp} + \frac{1}{2}\Psi_{\zeta\zeta}^p\left(\Delta\zeta\right)^2, \tag{C.9}$$

hence

$$\Psi_{\zeta\zeta}^v = \Psi_{\zeta\zeta}^p. \tag{C.10}$$

It may seem surprising that the curvature of the flux surface in the toroidal direction does not appear in this equation. However, this curvature is already accounted for in

our definition of $\Psi_{\zeta\zeta}$ that gives rise to the $K_R R$ term in equation (68). Moving forward, we consider purely poloidal displacement, that is, $\Delta\zeta = 0$,

$$
\begin{aligned}
K_R^{vp}\Delta R + K_Z^{vp}\Delta Z &+ \frac{1}{2}\left(\Psi_{RR}^v\left(\Delta R\right)^2 + 2\Psi_{RZ}^v\Delta R\Delta Z + \Psi_{ZZ}^v\left(\Delta Z\right)^2\right) \\
&= K_R^{vp}\Delta R + K_Z^{vp}\Delta Z + \frac{1}{2}\left(\Psi_{RR}^p\left(\Delta R\right)^2 + 2\Psi_{RZ}^p\Delta R\Delta Z + \Psi_{ZZ}^p\left(\Delta Z\right)^2\right).
\end{aligned}
\tag{C.11}
$$

Hence, to leading order, we use equations (C.3) and (C.7) to get

$$
\begin{aligned}
\Psi_{RR}^v\left(\frac{\partial\psi_p}{\partial Z}\right)^2 &- 2\Psi_{RZ}^v\frac{\partial\psi_p}{\partial R}\frac{\partial\psi_p}{\partial Z} + \Psi_{ZZ}^v\left(\frac{\partial\psi_p}{\partial R}\right)^2 \\
&= \Psi_{RR}^p\left(\frac{\partial\psi_p}{\partial Z}\right)^2 - 2\Psi_{RZ}^p\frac{\partial\psi_p}{\partial R}\frac{\partial\psi_p}{\partial Z} + \Psi_{ZZ}^p\left(\frac{\partial\psi_p}{\partial R}\right)^2.
\end{aligned}
\tag{C.12}
$$

Note that $\Delta R^{(2)}$ and $\Delta Z^{(2)}$ do not contribute because of the continuity of $\mathbf{K}$ across the boundary [53]. Finally, we consider a displacement that is simultaneously in the toroidal and poloidal directions. Following similar steps as earlier, and using the results we already have, we find that

$$
\Psi_{R\zeta}^v\Delta R\Delta\zeta + \Psi_{\zeta Z}^v\Delta\zeta\Delta Z = \Psi_{R\zeta}^p\Delta R\Delta\zeta + \Psi_{\zeta Z}^p\Delta\zeta\Delta Z.
\tag{C.13}
$$

Hence,

$$
-\Psi_{R\zeta}^v\frac{\partial\psi_p}{\partial Z} + \Psi_{\zeta Z}^v\frac{\partial\psi_p}{\partial R} = -\Psi_{R\zeta}^p\frac{\partial\psi_p}{\partial Z} + \Psi_{\zeta Z}^p\frac{\partial\psi_p}{\partial R}.
\tag{C.14}
$$

Equations (C.10), (C.12), and (C.14) give us 3 conditions for the transition, but we have 6 variables we want to find (either $\boldsymbol{\Psi}^p$ or $\boldsymbol{\Psi}^v$). The other 3 conditions can be found from equation (A.41), giving us

$$
\boldsymbol{\Psi}^p \cdot \nabla_K H + \nabla H = 0.
\tag{C.15}
$$

We solve these six linear equations numerically in Scotty.

If the equilibrium density were also discontinuous, then we would have to solve three more equations. Two are linear equations, which state that the components of $\mathbf{K}$ parallel to the flux surface have to be continuous. The third component of the wavevector can be determined from the dispersion relation, $H = 0$, which is nonlinear. A discontinuous $\mathbf{K}$ also means that the six equations for $\boldsymbol{\Psi}$ are changed slightly, because $\mathbf{K}^v \neq \mathbf{K}^p$. This is not currently implemented in Scotty.

Appendix D. Derivation of u_1 and u_2

We seek to find two coordinates whose gradients are perpendicular to $\hat{\mathbf{b}}$ as well as to each other. Unfortunately, due to magnetic shear, it is in general not possible to find such a set of coordinates throughout the whole volume of a plasma, but it is possible to do it along a line. Hence, we first seek to find u_1 and u_2 such that ∇u_1 and ∇u_2 are perpendicular to $\hat{\mathbf{b}}$ and to each other along $\mathbf{w} = 0$, that is, along the central ray. We then find the higher order corrections to u_1 and u_2 at finite $\mathbf{w}$ by imposing that ∇u_1 and ∇u_2 be perpendicular to $\hat{\mathbf{b}}$ everywhere.

We know that u_i must satisfy

$$\hat{\mathbf{b}}(\mathbf{q}(\tau) + \mathbf{w}) \cdot \nabla u_i \simeq \left[\hat{\mathbf{b}}(\mathbf{q}(\tau)) + \mathbf{w} \cdot \nabla \hat{\mathbf{b}}(\mathbf{q}(\tau))\right] \cdot \nabla u_i = 0. \tag{D.1}$$

Using the chain rule, we get

$$\underbrace{\left(\hat{\mathbf{b}} + \mathbf{w} \cdot \nabla \hat{\mathbf{b}}\right) \cdot \nabla \tau \frac{\partial u_i}{\partial \tau}}_{\sim \frac{1}{L} u_i} + \underbrace{\left(\hat{\mathbf{b}} + \mathbf{w} \cdot \nabla \hat{\mathbf{b}}\right) \cdot \nabla w_x \frac{\partial u_i}{\partial w_x}}_{\sim \frac{1}{W} u_i} + \underbrace{\left(\hat{\mathbf{b}} + \mathbf{w} \cdot \nabla \hat{\mathbf{b}}\right) \cdot \nabla w_y \frac{\partial u_i}{\partial w_y}}_{\sim \frac{1}{W} \frac{W}{L} \sim \frac{1}{L} u_i} = 0. \tag{D.2}$$

The size of the term proportional to $\partial u_i / \partial w_y$ is determined by the fact that ∇w_y points mostly along $\hat{\mathbf{y}}$ in Figure 6, and this direction is perpendicular to $\hat{\mathbf{b}}$. Using reciprocal vectors, we follow the same procedure used to derive equation (A.8) and get

$$\nabla w_x = \hat{\mathbf{x}} + \frac{w_y \hat{\mathbf{g}}}{g(1 - \boldsymbol{\kappa} \cdot \mathbf{w})} \left(\frac{\mathrm{d}\hat{\mathbf{x}}}{\mathrm{d}\tau} \cdot \hat{\mathbf{y}}\right), \tag{D.3}$$

and

$$\nabla w_y = \hat{\mathbf{y}} - \frac{w_x \hat{\mathbf{g}}}{g(1 - \boldsymbol{\kappa} \cdot \mathbf{w})} \left(\frac{\mathrm{d}\hat{\mathbf{x}}}{\mathrm{d}\tau} \cdot \hat{\mathbf{y}}\right). \tag{D.4}$$

Having obtained these results, we then expand u_i in W/L to obtain

$$u_i = u_i^{(0)} + u_i^{(1)} + u_i^{(2)} + \dots, \tag{D.5}$$

where $u_i^{(n)} \sim (W/L)^n \, u_i^{(0)}$. Since the term with $\partial u_i / \partial w_x$ is much larger than the other two terms, $\partial u_i^{(0)} / \partial w_x = 0$. Hence, $u_i^{(0)} = u_i^{(0)}(\tau, w_y)$. Since we want $\nabla u_1(\mathbf{w} = 0) = \hat{\mathbf{u}}_1$ and $\nabla u_2(\mathbf{w} = 0) = \hat{\mathbf{u}}_2$, where these directions are shown in Figure 6, we choose

$$u_1^{(0)} = u_1^{(0)}(\tau) = \int_0^\tau g(\tau') \cos \theta(\tau') \mathrm{d}\tau, \tag{D.6}$$

and

$$u_2^{(0)} = u_2^{(0)}(w_y) = w_y. \tag{D.7}$$

This turns out to be convenient because one direction is only a function of τ, while the other is only a function of w_y.

We now find the higher order corrections. The first order (W/L) equation for u_1 is

$$-\sin \theta \cos \theta - \frac{\partial u_1^{(1)}}{\partial w_x} \cos \theta = 0, \tag{D.8}$$

which gives us

$$u_1^{(1)} = -w_x \sin \theta. \tag{D.9}$$

The first order (W/L) equation for u_2 is

$$-\frac{\partial u_2^{(1)}}{\partial w_x} \cos \theta + \left(w_x \frac{\sin \theta}{g} \frac{\mathrm{d}\hat{\mathbf{x}}}{\mathrm{d}\tau} \cdot \hat{\mathbf{y}} + \mathbf{w} \cdot \nabla \hat{\mathbf{b}} \cdot \hat{\mathbf{y}}\right) \frac{\partial u_2^{(0)}}{\partial w_y} = 0, \tag{D.10}$$

which gives us

$$u_2^{(1)} = \frac{w_x^2}{2 \cos \theta} \left(\frac{\sin \theta}{g} \frac{\mathrm{d}\hat{\mathbf{x}}}{\mathrm{d}\tau} \cdot \hat{\mathbf{y}} + \hat{\mathbf{x}} \cdot \nabla \hat{\mathbf{b}} \cdot \hat{\mathbf{y}}\right) + \frac{w_x w_y}{\cos \theta} \hat{\mathbf{y}} \cdot \nabla \hat{\mathbf{b}} \cdot \hat{\mathbf{y}}. \tag{D.11}$$

Here we have used equations (A.8), (D.3), and (D.4). Since $k_{\perp,1}u_1^{(1)} \sim W/\lambda \gg 1$, we need to find the next order correction $u_1^{(2)}$, whereas $k_{\perp,2}u_2^{(1)} \sim (1/\lambda)(W^2/L) \sim 1$ indicates that expanding u_2 to this order is already sufficient. To get the second order contribution $u_1^{(2)}$, we use

$$
\begin{aligned}
&-\frac{\sin\theta}{g}\frac{\partial u_1^{(1)}}{\partial\tau} + \left(-\frac{\sin\theta}{g}\boldsymbol{\kappa}\cdot\mathbf{w} + \frac{\mathbf{w}\cdot\nabla\hat{\mathbf{b}}\cdot\hat{\mathbf{g}}}{g}\right)\frac{\partial u_1^{(0)}}{\partial\tau} \\
&-\cos\theta\frac{\partial u_1^{(2)}}{\partial w_x} + \left(-\frac{\sin\theta}{g}\frac{\mathrm{d}\hat{\mathbf{x}}}{\mathrm{d}\tau}\cdot\hat{\mathbf{y}}w_y + \mathbf{w}\cdot\nabla\hat{\mathbf{b}}\cdot\hat{\mathbf{x}}\right)\frac{\partial u_1^{(1)}}{\partial w_x} = 0,
\end{aligned}
\tag{D.12}
$$

and find that

$$
\begin{aligned}
u_1^{(2)} = &\frac{w_x^2}{2}\left(\frac{\sin\theta}{g}\frac{\mathrm{d}\theta}{\mathrm{d}\tau} - \boldsymbol{\kappa}\cdot\hat{\mathbf{x}}\sin\theta + \hat{\mathbf{x}}\cdot\nabla\hat{\mathbf{b}}\cdot\hat{\mathbf{g}} - \hat{\mathbf{x}}\cdot\nabla\hat{\mathbf{b}}\cdot\hat{\mathbf{x}}\tan\theta\right) \\
&+ w_x w_y\left(-\boldsymbol{\kappa}\cdot\hat{\mathbf{y}}\sin\theta + \hat{\mathbf{y}}\cdot\nabla\hat{\mathbf{b}}\cdot\hat{\mathbf{g}} + \frac{\sin\theta\tan\theta}{g}\frac{\mathrm{d}\hat{\mathbf{x}}}{\mathrm{d}\tau}\cdot\hat{\mathbf{y}} - \hat{\mathbf{y}}\cdot\nabla\hat{\mathbf{b}}\cdot\hat{\mathbf{x}}\tan\theta\right).
\end{aligned}
\tag{D.13}
$$

Appendix E. Relationship between θ and θ_m

To shed light on how θ and θ_m relate to each other (when they are small), we seek to make explicit the piece

$$
\frac{\partial H}{\partial(\mathbf{K}\cdot\hat{\mathbf{b}})^2}\left(\frac{\partial H}{\partial K^2}\right)^{-1},
\tag{E.1}
$$

in equation (138). This algebra-heavy process is detailed in Appendix E.1, while the results and their significance are discussed in Appendix E.2.

Appendix E.1. Derivation of θ/θ_m

The derivation is somewhat onerous because we cannot neglect θ_m from the onset; we need to keep $K_\parallel$ for part of the derivation to be able to calculate $\partial H/\partial K_\parallel^2$. Fortunately, since we are finding the ratio of two derivatives of H, we are free to choose a $\bar{H}$ that satisfies equation (42) because

$$
\frac{\partial H}{\partial K_\parallel^2}\left(\frac{\partial H}{\partial K^2}\right)^{-1} = \frac{\partial\bar{H}}{\partial K_\parallel^2}\left(\frac{\partial\bar{H}}{\partial K^2}\right)^{-1}.
\tag{E.2}
$$

For this calculation, we choose a convenient $\bar{H}$ to minimise the unpleasantness of the resulting algebra: $\bar{H} = \det(\boldsymbol{D})$,

$$
\begin{aligned}
\det(\boldsymbol{D}) = &\left(\epsilon_{11} - N_\parallel^2\right)\left(\epsilon_{11} - N^2\right)\left(\epsilon_{bb} - N^2 + N_\parallel^2\right) \\
&- N_\parallel^2\left(N^2 - N_\parallel^2\right)\left(\epsilon_{11} - N^2\right) - \epsilon_{12}^2\left(\epsilon_{bb} - N^2 + N_\parallel^2\right).
\end{aligned}
\tag{E.3}
$$

Here we have used equation (36), as well as the notation $N = Kc/\Omega$ and $N_\parallel = K_\parallel c/\Omega$. The derivatives that we need can then be calculated for $N_\parallel^2 = N^2\theta_m^2 \ll N^2$. We find

$$
\frac{\partial\det(\boldsymbol{D})}{\partial K^2} = \frac{c^2}{\Omega^2}\left[\epsilon_{11}\left(N^2 - \epsilon_{bb}\right) + \epsilon_{11}\left(N^2 - \epsilon_{11}\right) + \epsilon_{12}^2\right],
\tag{E.4}
$$

and

$$\frac{\partial \det(\boldsymbol{D})}{\partial K_\parallel^2} = \frac{c^2}{\Omega^2}\Big[\epsilon_{11}\left(\epsilon_{11} - N^2\right) - \left(\epsilon_{11} - N^2\right)\left(\epsilon_{bb} - N^2\right)$$
$$- N^2\left(\epsilon_{11} - N^2\right) - \epsilon_{12}^2\Big], \tag{E.5}$$

Now that we have evaluated the derivatives of $\bar{H}$, we find the piece that we care about

$$\frac{\partial H}{\partial K_\parallel^2}\left(\frac{\partial H}{\partial K^2}\right)^{-1} = \frac{\epsilon_{11}^2 - \epsilon_{12}^2 - \epsilon_{11}\epsilon_{bb} + N^2\left(\epsilon_{bb} - \epsilon_{11}\right)}{-\epsilon_{11}^2 + \epsilon_{12}^2 - \epsilon_{11}\epsilon_{bb} + 2N^2\epsilon_{11}}. \tag{E.6}$$

For the O mode, $N^2 = \epsilon_{bb}$, we have

$$\frac{\partial H}{\partial K_\parallel^2}\left(\frac{\partial H}{\partial K^2}\right)^{-1} = -\frac{\left(\epsilon_{11} - \epsilon_{bb}\right)^2 - \epsilon_{12}^2}{\epsilon_{11}\left(\epsilon_{11} - \epsilon_{bb}\right) - \epsilon_{12}^2}$$
$$= -\frac{\Omega_{pe}^2}{\Omega^2}. \tag{E.7}$$

Similarly, for the X mode, $\epsilon_{11}(\epsilon_{11} - N^2) = \epsilon_{12}^2$, we have

$$\frac{\partial H}{\partial K_\parallel^2}\left(\frac{\partial H}{\partial K^2}\right)^{-1} = -\frac{\epsilon_{12}^2\epsilon_{bb}}{\epsilon_{11}\left[\epsilon_{11}\left(\epsilon_{11} - \epsilon_{bb}\right) - \epsilon_{12}^2\right]}$$
$$= \frac{\Omega_{pe}^2\left(\Omega^2 - \Omega_{pe}^2\right)}{\Omega^2\left(\Omega^2 - \Omega_{ce}^2 - \Omega_{pe}^2\right)}. \tag{E.8}$$

Appendix E.2. Properties of θ/θ_m

Now that we have the ratio between θ_m and θ, we discuss what it means for the O and X modes. We have

$$\frac{\theta}{\theta_m} = -1 + \frac{\Omega_{pe}^2}{\Omega^2}, \tag{E.9}$$

for the O-mode and

$$\frac{\theta}{\theta_m} = -1 - \frac{\Omega_{pe}^2\left(\Omega^2 - \Omega_{pe}^2\right)}{\Omega^2\left(\Omega^2 - \Omega_{ce}^2 - \Omega_{pe}^2\right)}, \tag{E.10}$$

for the X-mode, Figure E1. For the O-mode, since we launch a beam into the plasma from vacuum, $\Omega > \Omega_{pe}$ always, and thus $\theta/\theta_m \le 0$ and $|\theta/\theta_m| \le 1$. However, for the X-mode, the cut-off frequency is $\Omega_R = (\Omega_{ce}^2/4 + \Omega_{pe}^2)^{1/2} + \Omega_{ce}/2$, which is above the upper hybrid frequency $\Omega_{UH}^2 = \Omega_{ce}^2 + \Omega_{pe}^2$. Consequently, we still have $\theta/\theta_m \le 0$, but now $|\theta/\theta_m| > 1$.

Since θ/θ_m is always negative, θ and θ_m have different signs no matter the mode. For the O-mode, the magnitude of this ratio is always less than one, so $|\theta| < |\theta_m|$, and for the X-mode, the magnitude of the same ratio is always more than one, so $|\theta| > |\theta_m|$. This is illustrated in Figure E2 for both positive and negative θ.
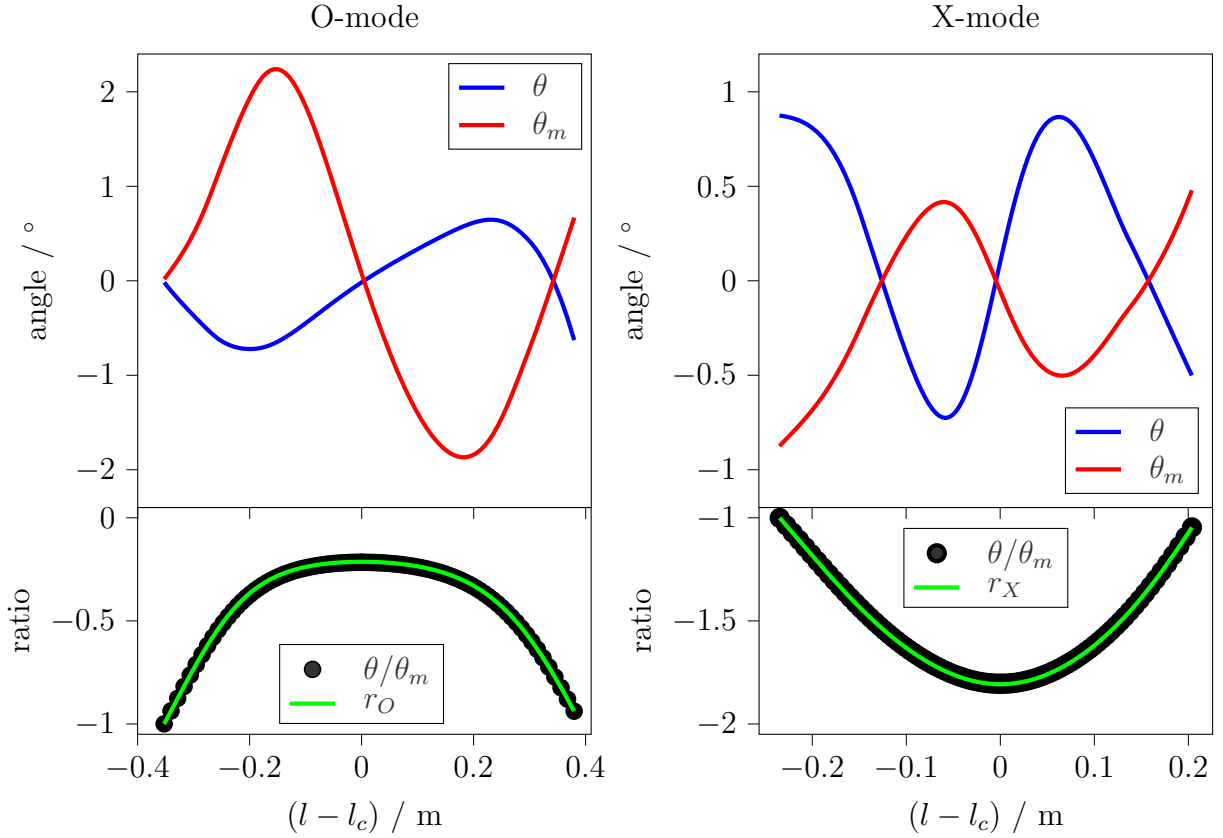
Figure E1: The variation of θ and θ_m along the ray (top), and how they relate to each other (bottom). Here $l - l_c$ is the distance along the ray from the cut-off. The standard MAST test scenario for our paper was used for the O-mode. For the X-mode, the toroidal launch angle was changed to $-7°$ such that $\theta_m = 0$ at the cut-off. In the lower subplots, we perform a sanity check; as expected, we have agreement between the ratio of θ to θ_m as calculated directly from these angles (black points) and from the right-hand sides of equations (E.9) and (E.10) (green lines).

Appendix F. Region near the cut-off

We use τ_c to denote the location where $dK/d\tau = 0$. The subscript $_c$ means that the function is evaluated at $\tau = \tau_c$, the nominal cut-off location.

We call $k_{c,1}$ the particular $k_{\perp,1}$ which scatters at τ_c,

$$k_{c,1} = -2K_c = -2K(\tau_c). \tag{F.1}$$

We Taylor expand the large phase piece $2is + ik_{\perp,1} \int_0^\tau g(\tau') \, d\tau'$ of equation (127) around $k_{c,1}$ and τ_c to determine what happens at the scattering location τ_c,

$$2s + k_{\perp,1} \int_0^\tau g(\tau') \, d\tau = 2s_c + k_{c,1} \int_0^{\tau_c} g(\tau') \, d\tau + (k_{\perp,1} - k_{c,1}) \int_0^{\tau_c} g(\tau') \, d\tau'$$

$$+ g_c(k_{\perp,1} - k_{c,1})(\tau - \tau_c) + \frac{1}{3}g_c \frac{d^2 K_g}{d\tau^2}\bigg|_{\tau_c} (\tau - \tau_c)^3. \tag{F.2}$$

(a) K_X and K_O when $\theta < 0$.　　　　(b) K_X and K_O when $\theta > 0$.
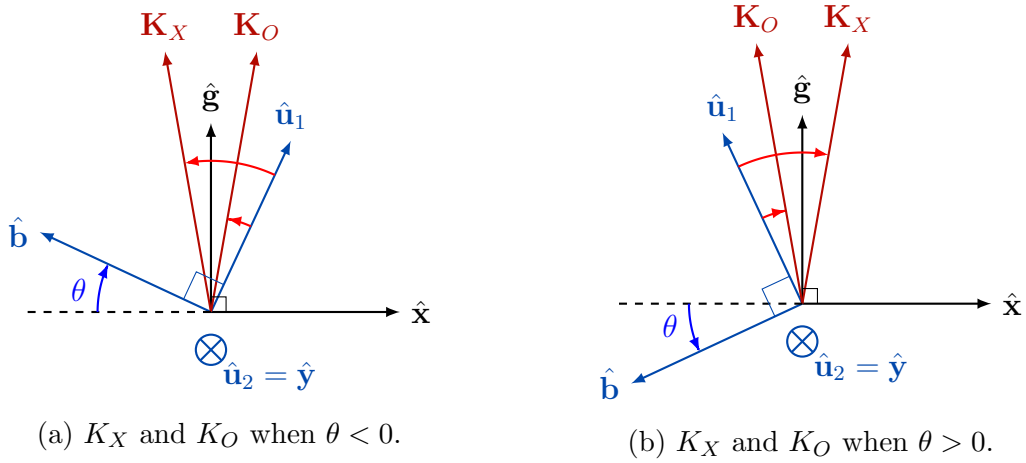
Figure E2: The wavevectors of the X-mode and O-mode are denoted by K_X and K_O respectively. This notation is only used in this section. We have shown that for the X-mode, $|\theta| > |\theta_m|$, and the O-mode, $|\theta| < |\theta_m|$. The unlabelled bright red arrows show θ_m. Note that θ and θ_m always have different signs, for reasons explained in this section. The angles used in this figure were chosen for illustration purposes: the real values of θ and θ_m for which our expansion is valid are too small for legible schematics.

We order

$$g_c \left. \frac{\mathrm{d}^2 K_g}{\mathrm{d}\tau^2} \right|_{\tau_c} (\tau - \tau_c)^3 \sim \frac{L}{\lambda} \left(\frac{\tau - \tau_c}{\tau_L} \right)^3 \sim 1, \tag{F.3}$$

and

$$g_c (k_{\perp,1} - k_{c,1})(\tau - \tau_c) \sim (k_{\perp,1} - k_{c,1}) L \frac{\tau - \tau_c}{\tau_L} \sim 1, \tag{F.4}$$

where $g\tau_L \sim L$. With these orderings, we can safely neglect the terms of the Taylor expansion of the phase that we have not included in equation (F.2). Equations (F.3) and (F.4) give $(\tau - \tau_c)/\tau_L \sim (\lambda/L)^{1/3} \ll 1$ and $(k_{\perp,1} - k_{c,1})/k_{c,1} \sim (\lambda/L)^{2/3} \ll 1$. As a result, functions that do not oscillate quickly with τ are evaluated only at τ_c. Then, using the integration variable

$$\xi = \left(g_c \left. \frac{\mathrm{d}^2 K_g}{\mathrm{d}\tau^2} \right|_{\tau_c} \right)^{\frac{1}{3}} (\tau - \tau_c), \tag{F.5}$$

equation (127) becomes

$$
\begin{aligned}
\tilde{A}_r = -\frac{\Omega A_{ant} g_{ant} \pi}{c} \int & \left[\frac{\det \left[\mathrm{Im} \left(\boldsymbol{\Psi}_{w,c} \right) \right]}{\det \left(\boldsymbol{M}_{w,c} \right)} \right]^{\frac{1}{2}} \exp(2\mathrm{i}\phi_{G,c}) \\
& \times \frac{\delta \tilde{n}_{e,c}}{n_{e,c}} \, \hat{\mathbf{e}}_c^* \cdot (\boldsymbol{\epsilon}_{eq,c} - \mathbf{1}) \cdot \hat{\mathbf{e}}_c \, \exp \left[2\mathrm{i}s_t + \mathrm{i}k_{\perp,1} \int_0^{\tau_t} g(\tau') \left(1 - \frac{\theta^2(\tau')}{2} \right) \, \mathrm{d}\tau' \right] \\
& \times \left(g_t \left. \frac{\mathrm{d}^2 K_g}{\mathrm{d}\tau^2} \right|_{\tau_t} \right)^{-\frac{1}{3}} \mathrm{Ai} \left[(k_{\perp,1} - k_{t,1}) g_t^{\frac{2}{3}} \left(\left. \frac{\mathrm{d}^2 K_g}{\mathrm{d}\tau^2} \right|_{\tau_t} \right)^{-\frac{1}{3}} \right] \\
& \times \exp \left[-\frac{\mathrm{i}}{4} (2\mathbf{K}_{w,c} + \mathbf{k}_{\perp,w,c}) \cdot \boldsymbol{M}_{w,c}^{-1} \cdot (2\mathbf{K}_{w,c} + \mathbf{k}_{\perp,w,c}) \right] \, \mathrm{d}k_{\perp,1} \, \mathrm{d}k_{\perp,2}.
\end{aligned}
\tag{F.6}
$$

where $\mathrm{Ai}(z) = (2\pi)^{-1} \int_{-\infty}^{\infty} \exp(z\xi + \xi^3/3)\mathrm{d}\xi$ is the Airy function. We have thus shown that there is indeed no divergence at the cut-off.

References

[1] Hillesheim J C, Peebles W A, Rhodes T L, Schmitz L, Carter T A, Gourdain P A and Wang G 2009 *Review of Scientific Instruments* **80** ISSN 00346748

[2] Hirsch M, Holzhauer E, Baldzuhn J, Kurzan B and Scott B 2001 *Plasma Physics and Controlled Fusion* **43** 1641–1660 ISSN 07413335

[3] Hillesheim J C, Parra F I, Barnes M, Crocker N A, Meyer H, Peebles W A, Scannell R and Thornton A 2015 *Nuclear Fusion* **55** 032003 ISSN 0029-5515 (*Preprint* `1407.2121v2`)

[4] Conway G D, Scott B, Schirmer J, Reich M, Kendl A and Team t A U 2005 *Plasma Physics and Controlled Fusion* **47** 1165–1185 ISSN 0741-3335

[5] Conway G D, Poli E, Happel T *et al.* 2010 *Plasma and Fusion Research* **5** S2005–S2005

[6] Schmitz L 2017 *Nuclear Fusion* **57** 025003

[7] Tynan G R, Fujisawa A and McKee G 2009 *Plasma Physics and Controlled Fusion* **51** 113001

[8] Hennequin P, Honoré C, Truc A, Quéméneur A, Lemoine N, Chareau J M and Sabot R 2004 *Review of Scientific Instruments* **75** 3881–3883

[9] Happel T, Estrada T, Blanco E, Tribaldos V, Cappa A and Bustos A 2009 *Review of Scientific Instruments* **80** 073502

[10] Zhou C, Liu A D, Zhang X H, Hu J Q, Wang M Y, Li H, Lan T, Xie J L, Sun X, Ding W X *et al.* 2013 *Review of Scientific Instruments* **84** 103511

[11] Happel T, Görler T, Hennequin P, Lechte C, Bernert M, Conway G D, Freethy S J, Honoré C, Pinzón J, Stroth U *et al.* 2017 *Plasma Physics and Controlled Fusion* **59** 054009

[12] Shi Z, Zhong W, Jiang M, Yang Z, Zhang B, Shi P, Chen W, Wen J, Chen C, Fu B *et al.* 2016 *Review of Scientific Instruments* **87** 113501

[13] Rhodes T L, Barada K, Peebles W A and Crocker N A 2016 *Review of Scientific Instruments* **87** 11E726

[14] Hu J, Zhou C, Liu A, Wang M, Doyle E, Peebles W, Wang G, Zhang X, Zhang J, Feng X *et al.* 2017 *Review of Scientific Instruments* **88** 073504

[15] Tokuzawa T, Tsuchiya H, Tsujimura T, Emoto M, Nakanishi H, Inagaki S, Ida K, Yamada H, Ejiri A, Watanabe K Y *et al.* 2018 *Review of Scientific Instruments* **89** 10H118

[16] Molina Cabrera P, Coda S, Porte L, Smolders A and Team T 2019 *Review of Scientific Instruments* **90** 123501

[17] Wen J, Shi Z, Zhong W, Yang Z, Yang Z, Wang B, Jiang M, Shi P, Hillesheim J, Freethy S *et al.* 2021 *Review of Scientific Instruments* **92** 063513

[18] Tokuzawa T, Tanaka K, Tsujimura T, Kubo S, Emoto M, Inagaki S, Ida K, Yoshinuma M, Watanabe K, Tsuchiya H *et al.* 2021 *Review of Scientific Instruments* **92** 043536

[19] Carralero D, Happel T, Estrada T, Tokuzawa T, Martínez J, de la Luna E, Cappa A and García J 2021 *Fusion Engineering and Design* **173** 112803

[20] Yashin A, Bulanin V, Petrov A and Ponomarenko A 2021 *Applied Sciences* **11** 8975

[21] Volpe F A 2017 *Journal of Instrumentation* **12** C01094

[22] Costley A E 2010 *IEEE Transactions on Plasma Science* **38** 2934–2943

[23] Piliya A D and Popov A Y 2002 *Plasma Physics and Controlled Fusion* **44** 467

[24] Gusakov E Z and Surkov A V 2004 *Plasma Physics and Controlled Fusion* **46** 1143

[25] Bulanin V V and Yafanov M V 2006 *Plasma Physics Reports* **32** 47–55

[26] Gusakov E Z and Kosolapova N V 2011 *Plasma Physics and Controlled Fusion* **53** 045012 URL https://doi.org/10.1088/0741-3335/53/4/045012

[27] Krutkin O, Altukhov A B, Gurchenko A D, Gusakov E Z, Irzak M A, Esipov L A, Sidorov A, Chôné L, Kiviniemi T P, Leerink S *et al.* 2019 *Nuclear Fusion*

[28] Catto P J 1978 *Plasma Physics* **20** 719

[29] Frieman E and Chen L 1982 *The Physics of Fluids* **25** 502–508

[30] Hillesheim J C, Crocker N A, Peebles W A, Meyer H, Meakins A, Field A R, Dunai D, Carr M, Hawkes N, Team M *et al.* 2015 *Nuclear Fusion* **55** 073024

[31] Coelho R, Alves D, Hawkes N, Brix M and Contributors J E 2009 *Review of Scientific Instruments* **80** 063504

[32] Ko J 2016 *Review of Scientific Instruments* **87** 11E541

[33] Damba J, Hong R, Pratt Q and Rhodes T 2021 *Bulletin of the American Physical Society*

[34] Stix T H 1992 *Waves in plasmas* (Springer Science & Business Media)

[35] Hirsch M, Holzhauer E, Baldzuhn J, Kurzan B and Scott B 2001 *Plasma Physics and Controlled Fusion* **43** 1641

[36] Silva F d, Heuraux S, Lemoine N, Honoré C, Hennequin P, Manso M and Sabot R 2004 *Review of Scientific Instruments* **75** 3816–3818

[37] Hillesheim J, Holland C, Schmitz L, Kubota S, Rhodes T and Carter T 2012 *Review of Scientific Instruments* **83** 10E331

[38] Williams T, Köhn A, O'Brien M and Vann R 2014 *Plasma Physics and Controlled Fusion* **56** 075010

[39] Peysson Y, Decker J and Morini L 2012 *Plasma Physics and Controlled Fusion* **54** 045003

[40] Marushchenko N B, Erckmann V, Hartfuss H J, Hirsch M, Laqua H P, Maassberg H and Turkin Y 2007 *Plasma and Fusion Research* **2** S1129

[41] Farina D 2007 *Fusion Science and Technology* **52** 154–160

[42] Prater R, Farina D, Gribov Y, Harvey R W, Ram A, Lin-Liu Y R, Poli E, Smirnov A P, Volpe F, Westerhof E *et al.* 2008 *Nuclear Fusion* **48** 035006

[43] Honoré C, Hennequin P, Truc A and Quéméneur A 2006 *Nuclear fusion* **46** S809

[44] Casperson L W 1973 *Applied optics* **12** 2434–2441

[45] Červenỳ V, Popov M M and Pšenčík I 1982 *Geophysical Journal International* **70** 109–128

[46] Kravtsov Y A and Berczynski P 2007 *Studia Geophysica et Geodaetica* **51** 1–36

[47] Peeters A G 1996 *Physics of Plasmas* **3** 4386–4395

[48] Pereverzev G 1992 *Nuclear fusion* **32** 1091

[49] Pereverzev G V 1993

[50] Pereverzev G V 1996 Paraxial wkb solution of a scalar wave equation *Reviews of Plasma Physics: Volume 19* ed Kadomtsev B B (Springer) pp 1–48

[51] Pereverzev G V 1998 *Physics of Plasmas* **5** 3529–3541

[52] Poli E, Pereverzev G V and Peeters A G 1999 *Physics of Plasmas* **6** 5–11

[53] Poli E, Peeters A G and Pereverzev G V 2001 *Physics of Plasmas* **8** 4325–4330

[54] Poli E, Peeters A G and Pereverzev G V 2001 *Computer Physics Communications* **136** 90–104

[55] Ramponi G, Farina D, Henderson M A, Poli E, Sauter O, Saibene G, Zohm H and Zucca C 2008 *Nuclear Fusion* **48** 054012

[56] Bertelli N, Balakin A, Westerhof E and Buyanova M 2010 *Nuclear Fusion* **50** 115008

[57] Rodrigues P and Bizarro J P 2002 *IEEE transactions on plasma science* **30** 68–69

[58] Thomas D A 2016 *Phased array imaging of two dimensional Doppler microwave backscattering from spherical tokamak edge plasmas* Ph.D. thesis University of York

[59] Stegmeir A, Conway G D, Poli E and Strumberger E 2011 *Fusion Engineering and Design* **86** 2928–2942

[60] Hillesheim J C, Delabie E, Meyer H, Maggi C F, Meneses L, Poli E, Contributors J, Consortium E *et al.* 2016 *Physical Review Letters* **116** 065002

[61] Maj O, Pereverzev G V and Poli E 2009 *Physics of Plasmas* **16** 062105

[62] Fidone I and Granata G 1971 *Nuclear Fusion* **11** 133

[63] Boyd D A 1985 *Proceedings of the Fifth Joint Workshop on Electron Cyclotron Emission and Electron Cyclotron Resonant Heating* 77

[64] Donné A, De Baar M and Cavazzana R 1997 *Review of scientific instruments* **68** 473–476

[65] Minami K, Ejiri A, Tanaka K and Watanabe T 1998 *Japanese journal of applied physics* **37** 6601

[66] Nagasaki K, Ejiri A, Mizuuchi T, Obiki T, Okada H, Sano F, Zushi H, Besshou S and Kondo K 1999 *Physics of Plasmas* **6** 556–564

[67] Tokuzawa T, Kawahata K, Tanaka K, Nagayama Y, Group L E, Kaneba T and Ejiri A 2003 *Review of scientific instruments* **74** 1506–1509

[68] Tokuzawa T, Kawahata K, Nagayama Y, Inagaki S, De Vries P, Mase A, Kogi Y, Yokota Y, Hojo H, Tanaka K *et al.* 2010 *Fusion Science and Technology* **58** 364–374

[69] Booker H G 1936 *Proceedings of the Royal Society of London. Series A-Mathematical and Physical Sciences* **155** 235–257

[70] Booker H G 1938 *Philosophical Transactions of the Royal Society of London. Series A, Mathematical and Physical Sciences* **237** 411–451

[71] Lao L, John H S, Stambaugh R, Kellman A and Pfeiffer W 1985 *Nuclear fusion* **25** 1611

[72] Appel L, Huysmans G, Lao L, McCarthy P, Muir D, Solano E, Storrs J, Taylor D, Zwingmann W *et al.* 2006 A unified approach to equilibrium reconstruction *Proceedings-33rd EPS conference on Controlled Fusion and Plasma Physics, pp. P–2.160*

[73] Virtanen P, Gommers R, Oliphant T E, Haberland M, Reddy T, Cournapeau D, Burovski E, Peterson P, Weckesser W, Bright J, van der Walt S J, Brett M, Wilson J, Millman K J, Mayorov N, Nelson A R J, Jones E, Kern R, Larson E, Carey C J, Polat İ, Feng Y, Moore E W, VanderPlas J, Laxalde D, Perktold J, Cimrman R, Henriksen I, Quintero E A, Harris C R, Archibald A M, Ribeiro A H, Pedregosa F, van Mulbregt P and SciPy 10 Contributors 2020 *Nature Methods* **17** 261–272

[74] Dormand J R and Prince P J 1980 *Journal of computational and applied mathematics* **6** 19–26

[75] Scannell R, Walsh M, Dunstan M, Figueiredo J, Naylor G, O'Gorman T, Shibaev S, Gibson K and Wilson H 2010 *Review of Scientific Instruments* **81** 10D520

[76] Slusher R E and Surko C M 1980 *The Physics of Fluids* **23** 472–490

[77] Hutchinson I H 2002 *Principles of Plasma Diagnostics* (IOP Publishing)

[78] Froula D, Glenzer S H, Luhmann Jr N C and Sheffield J 2011 *Plasma scattering of electromagnetic radiation: theory and measurement techniques* (Academic press)

[79] Brooker G and Brooker G 2003 *Modern classical optics* vol 8 (Oxford University Press)

[80] Goldsmith P F 1998 *Quasioptical systems* (Chapman & Hall New York)

[81] Villeneuve A and Harrington R 1958 *IRE Transactions on Microwave Theory and Techniques* **6** 308–310

[82] Gusakov E Z and Tyntarev M A 1997 *Fusion Engineering and Design* 501–505

[83] Holzhauer E, Hirsch M, Grossmann T, Branas B and Serra F 1998 *Plasma physics and controlled fusion* **40** 1869

[84] Conway G, Schirmer J, Klenge S, Suttrop W, Holzhauer E *et al.* 2004 *Plasma Physics and Controlled Fusion* **46** 951

[85] Pinzón J, Estrada T, Happel T, Hennequin P, Blanco E, Stroth U, Teams T I *et al.* 2019 *Plasma Physics and Controlled Fusion* **61** 105009

[86] Lechte C 2009 *IEEE Transactions on Plasma Science* **37** 1099–1103

[87] Lechte C, Conway G, Görler T, Tröster-Schmid C *et al.* 2017 *Plasma Physics and Controlled Fusion* **59** 075006

[88] Ruiz Ruiz J, Parra F I, Hall-Chen V H, Christen N, Barnes B, Candy J, Garcia J, Giroud C, Guttenfelder W, Hillesheim J C, Holland C, Howard N T, Ren Y, White A E and JET contributors In press *Plasma Physics and Controlled Fusion*

[89] Schekochihin A, Cowley S, Dorland W, Hammett G, Howes G G, Plunk G, Quataert E and Tatsuno T 2008 *Plasma Physics and Controlled Fusion* **50** 124024

[90] Schekochihin A, Cowley S, Dorland W, Hammett G, Howes G G, Quataert E and Tatsuno T 2009 *The Astrophysical Journal Supplement Series* **182** 310

[91] Barnes M, Parra F and Schekochihin A 2011 *Physical Review Letters* **107** 115003